Search for a diffuse neutrino emission in the Southern Sky with the ANTARES telescope

Presentata da: **Luigi Antonio Fusco**

Coordinatore Dottorato: Supervisore:
Prof. Gastone Castellani   **Prof.ssa Annarita Margiotta**

Can you hear?
Can you touch?
Can you see?
Can you really see?

Introduction

Neutrino astronomy is probably the youngest branch of astroparticle physics. Though astrophysical neutrinos have been observed from the Sun and from a Supernova collapse since almost 30 years, only recently the IceCube detector provided the observation of high energy neutrinos of cosmic origin. This has opened a new window of observation on the Universe.

For almost the entire history of mankind, in practice from the beginning of human history to the twentieth century, optical observations have been used to study the Universe. However, this is only an extremely limited window of observation in the spectrum of light. The radio, microwave, infrared, ultraviolet, X and γ bands of the photon spectrum have indeed provided in the last hundred of years a huge amount of information on the mechanisms operating in cosmic objects. Considering the energy output of astrophysical objects such as, for example, Supernova explosions, photons can be only a marginal output of the astrophysical event. In addition, photons can be absorbed or scattered when travelling from their source to Earth and information can be lost in this way. In many high energy astrophysical events, a large amount of energy is given to charged and neutral particles. In particular, neutrinos produced close to astrophysical objects can give fundamental information on the mechanisms in action. The observation of a few neutrino events from the Supernova SN1987A has given us a detailed insight on the explosion of massive stars. Analogously, observing neutrinos from other, more energetic, astrophysical objects could answer many questions on the way these objects work.

A great unanswered question in astroparticle physics can be solved with the observation of neutrinos of extra-terrestrial origin. The origin, the sources and the acceleration mechanisms of charged cosmic rays are still unknown. Since neutrinos could be produced in the dense environment surrounding the acceleration site, they can directly point to the cosmic ray source and accelerator. In addition, charged cosmic rays interacting in the Milky Way would produce a detectable flux of neutrinos and propagation models of cosmic rays could be tested.

In 1960, Markov proposed a possible way to detect high energy neutrinos using huge volumes of transparent natural material such as ice or sea water. High energy astrophysical neutrinos would undergo charged current weak interactions with one of the nucleons of the medium. This would produce charged particle that emit Cherenkov photons ice or water, which can be detected by a lattice of photomultipliers. Considering charged current interaction of muon neutrinos, above few TeV, the resulting muons can travel kilometres in the medium and are almost collinear with the parent neutrinos. This allows to point back to the neutrino sources if the muon direction can be precisely reconstructed. Given the

low cross section of νN interactions and the predicted astrophysical neutrino fluxes, the typical size of the detector should be of the order of km^3.

The ANTARES neutrino telescope is a three-dimensional array of photomultipliers distributed over 12 lines, installed in the Mediterranean Sea. The detector has been operated in partial configurations since March 2006 and was completed in May 2008. It is taking data continuously since then. The main goal of the experiment is to search for high energy neutrinos from astrophysical sources. A neutrino telescope in the Northern hemisphere includes the Galactic Centre in its field of view and is complementary to the IceCube Antarctic telescope. This complementarity can provide a different insight in the cosmic signal observed only by the IceCube Collaboration.

In this thesis a search for extended neutrino sources in the Southern sky with the ANTARES neutrino telescope is presented. The possibility that the cosmic signal observed by IceCube could due to point-like neutrino sources in the central part of our Galaxy has been already excluded using ANTARES data. Large-sized neutrino-emitting regions might not be resolved by the IceCube telescope since its angular resolution is limited by ice properties. In particular, the Galactic Plane is a guaranteed source of neutrinos. These neutrinos are produced by the interaction of cosmic rays that are confined in the Milky Way with the interstellar medium.

The structure of this thesis is as follows. A general overview of the knowledge of cosmic rays and neutrino astrophysics in given in Chapter 1. In Chapter 2 the neutrino detection principle is explained and an overview on neutrino telescopes is given, together with a review of the present status of experimental results. Chapter 3 reports on possible diffuse neutrino fluxes from the Galactic Plane. Then, the ANTARES telescope is presented in Chapter 4, along with the Monte Carlo simulation and analysis tools used for the analysis. In Chapter 5, the analysis of the atmospheric neutrino background is presented. Chapter 6 is devoted to the search for an enhanced emission of cosmic neutrinos from the Galactic Plane, analysing the complete ANTARES data sample. Finally, Chapter 7 presents an outlook towards the next generation neutrino telescope KM3NeT, whose construction has started in the last months.

Contents

Chapter 1

High energy neutrino astrophysics

1.1 Cosmic rays

The existence of a cosmic radiation, now known as Cosmic Rays (CRs), was discovered in 1912 by Victor Hess [1]. Using golden electrometers in free balloon flights, he measured the intensity of natural radiation and found out that it increases with altitude. This proved that some kind of ionising radiation enters the atmosphere from above. The nature of cosmic rays was longly debated and in 1930 Bruno Rossi [2] proposed that the presence of an "East-West" asymmetry in the directional intensity could be explained if CRs were charged particles. This was experimentally verified in the following years [3, 4, 5].

Until the advent of particle accelerators, cosmic rays represented the only source of high energy particles and some of them, such as the positron [6], the muon [7] and the pion [8], were discovered studying CRs. Many investigations have been made on the nature of cosmic rays since their discovery, but their origin and the mechanisms connected to their acceleration are not yet completely clear.

1.1.1 Cosmic ray composition and spectrum

The energy spectrum of primary CRs ranges from $\sim 10^9$ to $\sim 10^{20}$ eV. About 90% of the particles arriving at the top of the atmosphere are protons; helium nuclei (α particles) constitute $\sim 9\%$ of the cosmic ray radiation while the rest is given by heavier nuclei, electrons and γ-rays. A small quantity of antimatter is also present. The elemental composition of CR radiation is quite similar to what is observed in the Solar System, with some evident differences as shown in figure 1.1: Li-Be-B and Sc-Ti-V-Cr-Mn are relatively more abundant in CRs than in the Solar System by several orders of magnitude. Collisions (*spallation* processes) in the interstellar medium (ISM) of primary C and O, for the first group, and of Fe nuclei for the second one produce an enhancement in their relative abundance [9].

Below 10^{14} eV direct composition measurements are possible with satellite and balloon experiments. At higher energies only indirect measurements are
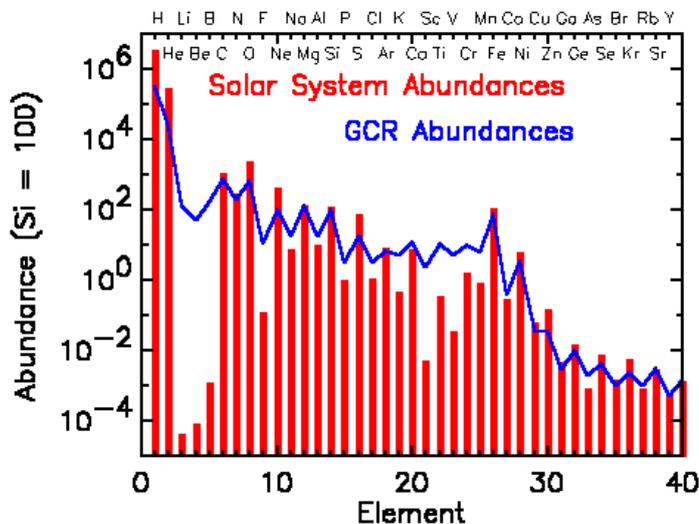
Figure 1.1: Relative (Si = 100) abundances of elements in cosmic rays (blue line) and in the Solar System (red bars) [9]. Two groups of elements (Li-Be-B and Sc-Ti-V-Cr-Mn) show significant difference in the cosmic rays abundances with respect to what is observed in the Solar System.

available as the CR flux is too low to collect enough statistics. The interaction of a primary CR with air nuclei produces extensive showers of particles. Very large ground array detectors, observing the products of CR interactions in the atmosphere, can collect many events but can only indirectly infer the mass of the nucleus originating the detected shower of particles. These indirect measurements seem to confirm that, beyond the knee, CR composition becomes heavier [10]. These results are however strongly model dependent and a precise determination of the composition is not possible.

At a first approximation, the primary energy spectrum (figure 1.2) follows an unbroken power law

$$\frac{dN}{dE} \propto E^{-\gamma}. \tag{1.1}$$

At least two changes of slope are evident in the spectrum: the *knee* around 10^{15} eV and the *ankle* above $10^{18.5}$ eV. The spectral index γ has approximately the value of 2.7 up to the knee. It then rises to a value of about 3.1. A flattening of the spectrum is present at the ankle, where $\gamma \sim 2.7$. Finally, at the highest energies, a cut-off seem to be present. The steepening of the energy spectrum in the knee region is still an open question, and many models have been proposed to explain such a variation [12]. A Z-dependence of the maximal energy at the main galactic acceleration sites (probably supernovae remnants, SNRs) can be translated into a different cut-off energy for each nuclear species and would be visible in a transition from a *proton-rich* to an *iron-rich* composition at the knee.

A different class of galactic objects is expected to accelerate CRs after the knee. Details on CR acceleration mechanisms are discussed in §1.1.2. Figure 1.3 shows a collection of results on the CR spectrum measurement above 10^{12} eV: the spectrum is here multiplied by $E^{2.5}$ to emphasise its features. After the knee,
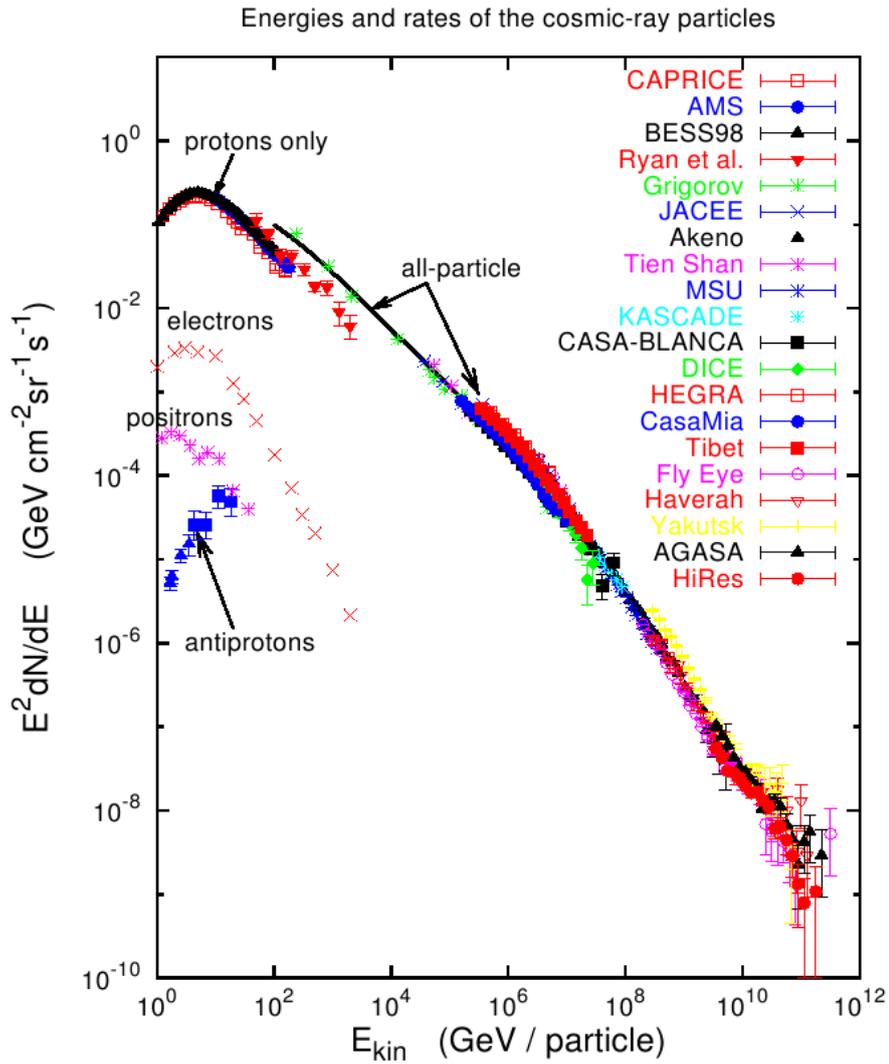
Figure 1.2: Cosmic ray energy spectrum from 1 to 10^{12} GeV as measured by many different experiments, both on balloons, satellites and on the ground as in the legend [11]. The spectrum is multiplied by E^2 to better show its features – mainly the knee, the ankle and a ultra-high energy cut-off.
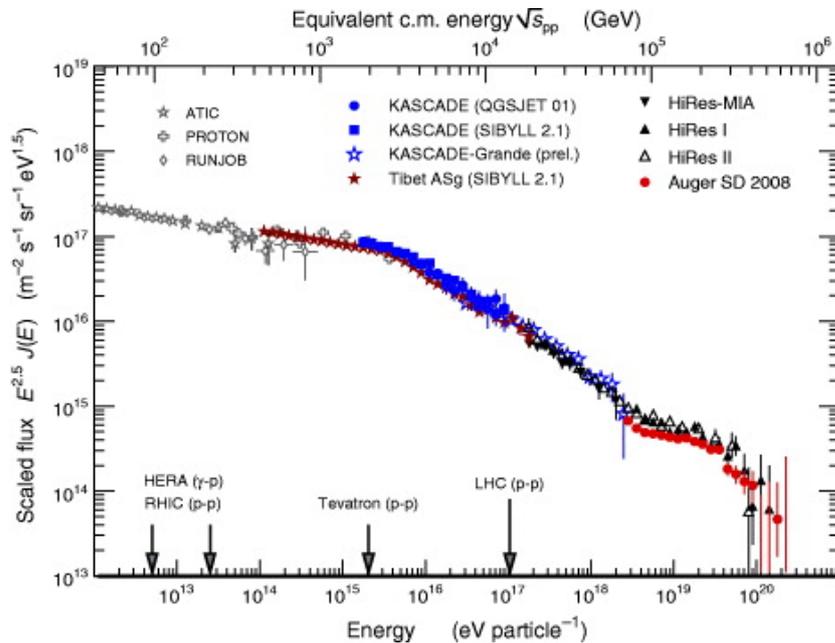
Figure 1.3: Collection of measurement of the CR energy spectrum above 10^{12} eV [13]. The spectrum is multiplied by $E^{2.5}$ in order to show structures in its shape such as the knee, the ankle and the high energy cut-off.

the so-called ankle is visible around $10^{18.5}$ eV, where the spectrum flattens. This feature is usually attributed to a transition from galactic to extra-galactic sources of cosmic rays [14]. A flatter spectrum is indeed expected for extra-galactic CRs.

An upper limit to the energy of cosmic rays is given by the so-called *Greisen-Zatsepin-Kuz'min* (GZK) effect [15, 16]: the interaction of CRs with Cosmic Microwave Background (CMB) photons via the Δ^+ resonance would limit the energy of cosmic rays at about 6×10^{19} eV. Different experiments have measured a cut-off in the CR spectrum at the highest energies [17, 18, 19], but some tension is still present in the interpretation of this feature.

The arrival direction of cosmic rays at the top of the atmosphere is isotropically distributed. The presence of galactic ($\simeq 4\,\mu$G) and extra-galactic ($\simeq$ nG) magnetic fields bends the trajectory of charged particle. The Larmor radius

$$R_L = \frac{mv_\perp}{|q|B} \qquad (1.2)$$

of a proton in the galactic magnetic field becomes compatible with the thickness of the Milky Way ($\simeq 200\,$pc) only above 10^{18} eV. Particles of lower energy or higher charge are confined in the Galaxy and randomly deflected many times in the irregularities of the magnetic field. Only very high energy cosmic rays can point back to their sources.

1.1.2 Cosmic ray accelerators

Cosmic ray acceleration through iterative scattering processes was firstly suggested by Enrico Fermi [20, 21]. Shock waves can be produced in extreme

environments such as in the proximity of black holes or after the collapse of a massive star. Stochastic iterative acceleration can be explained if one imagines to follow a charged particle entering the acceleration region with energy E. Assuming a particle trapped in magnetic field inhomogeneities, each time the particle encounters the shock wave its energy is increased by $\Delta E = \epsilon E$. The gain ϵ is due to the relative movement of the shock wave with respect to inhomogeneities of the magnetic field. The energy gain in a moving gas cloud is proportional to β^2, where β is the cloud velocity in units of c. This is often referred to as *Fermi second order acceleration*. A more efficient acceleration is achievable when a plane shock front is encountered by the particle. In this case the energy gain is proportional to β (*first order acceleration*). The energy spectrum of particles accelerated via Fermi mechanisms is described by an unbroken power law with spectral index $\gamma \sim 2$. Propagation and interaction of CRs in the Galaxy steepens the energy spectrum making it more similar to what is observed at Earth [22].

The relation between the energy that a cosmic ray can reach and the properties of its accelerator in terms of size and magnetic field can be graphically described in the so-called "Hillas plot" (figure 1.4). At a fixed size of the acceleration site, the higher the intensity of the magnetic field, the longer the CR is confined within its surrounding and can be further accelerated via Fermi mechanisms. At a given magnetic field intensity, the larger the site, the more encounters with the accelerating shocks are possible. Finally, a more compact object would require a higher magnetic field intensity to accelerate a CR to the same energy as a larger source. Moreover, the presence of a relativistic shock, with a Lorentz boost factor Γ, can produce a further enhancement of the CR energy.

Galactic sources

Fermi acceleration mechanism is believed to occur in SNRs. After a supernova (SN) explosion, the emitted material encounters the ISM and a shock front is built. Charged particles are accelerated in shock-waves of the expanding shells via the first order Fermi mechanism. With some quick calculations [22] it is possible to explain the CR energy density in our Galaxy considering the energy release of a Supernova, the Fermi mechanism efficiency and rate of SNe events. SNRs can accelerate nuclei up to $E^{max} \sim 300 \times Z$ TeV. This is the energy at which a change of slope appears in the cosmic ray energy spectrum. The transition over the knee can thus be explained as a Z dependence of the maximal energy at which cosmic rays can be accelerated at SNRs (figure 1.6).

Beyond the energy threshold for SNRs, different mechanisms, providing further particle acceleration, must be taken into account. This is possible, e.g., when a Neutron Star (NS) with a strong magnetic field is present in the SNR environment since it works as an additional particle accelerator. These object are also called Pulsar Wind Nebulae (PWNe). Indeed the magnetic field of the NS is often misaligned with respect to its rotation axis. Spinning magnetic fields can produce strong electric fields through Faraday's law. Given the strong intensity of the magnetic fields around the NS, few of these objects can provide enough energy to fill the Galaxy with CRs up to 10^{18} eV.

Further candidate galactic CR accelerators are micro-quasars, where a compact object accretes material from a normal star. The infalling matter releases gravitational potential energy. Due to this enormous motion of ionized matter, very strong electromagnetic fields are produced in the vicinity of the compact
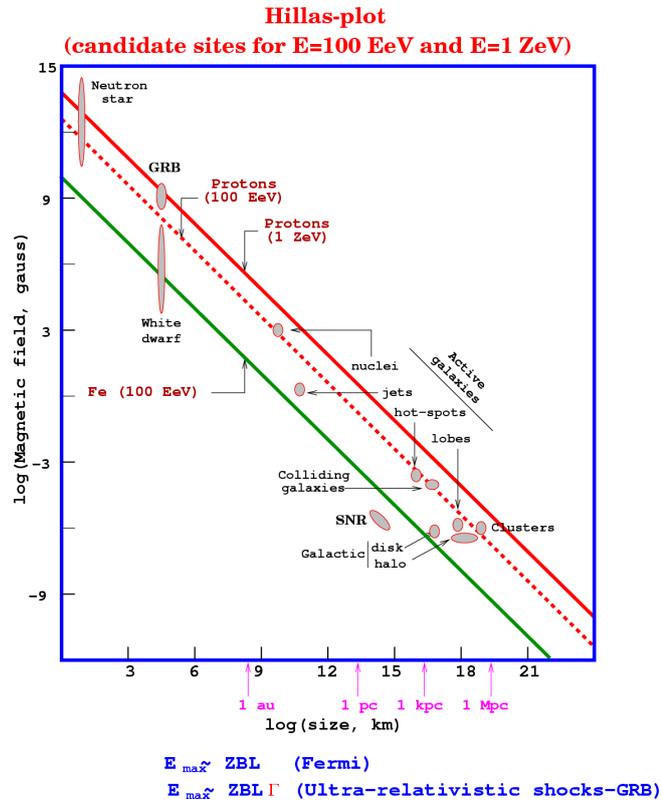
Figure 1.4: The Hillas plot, schematically showing the properties of acceleration sites, size and magnetic field strength, for a given maximal energy of a cosmic ray. Sources above the red solid (dashed) line can accelerate protons up to 1 ZeV (100 EeV). The green line refers to the acceleration of Iron nuclei up to 100 EeV

(a) SN1006   (b) Expanding shell
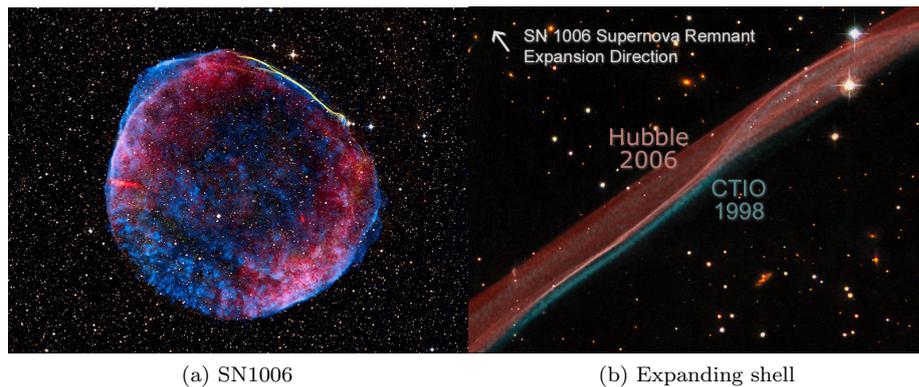
Figure 1.5: Left: SNR of SN1006, in the Lupus constellation. It is the remnant of the supernova described by various observers all over the world during A.D. 1006, probably being the brightest stellar event ever recorded in human history. Right: expanding shell of SN1006, comparing two different images from 1998 and 2006. Images from www.apod.nasa.gov and hubblesite.org
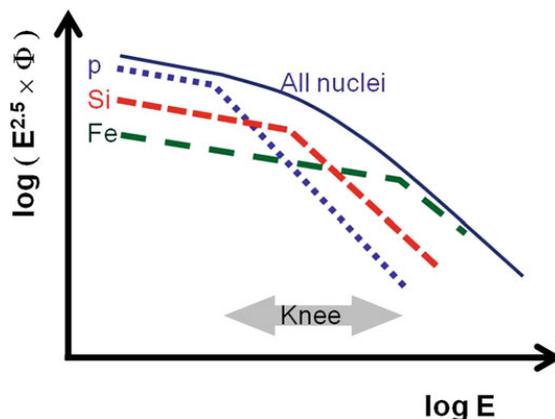
Figure 1.6: The interpretation of the CRs knee as due to the correlation between the maximum energy achievable at the acceleration site and the nuclear charge Z. The flux of each nuclear species sharply decreases after a given cut-off depending on Z. The behaviour of hydrogen, silicon (Z = 14) and iron (Z = 26) nuclei are shown [22].

object and charged particles can be accelerated to high energies. Most galactic objects which could accelerate CRs are located in the Galactic Plane, where the highest density of SNRs, PWNe and micro-quasars is present.

Extra-galactic sources

Active Galactic Nuclei (AGN) are the most powerful continuous sources of radiation in the Universe. A supermassive black hole (SMBH) is often present at the centre of galaxies. When fed with accreting matter, jets of particle and radiation can be emitted and the emission region around the SMBH becomes visible as an AGN. The AGN becomes even more luminous than its host galaxy if its emission is collimated in the line of sigth of the observer. A large variety of objects can be classified as AGNs. The *unified model* for AGNs [23, 24] explains the large variety of observed features considering that the same kind of objects can seen from different angles (figure 1.7). Because of the presence of emission jets and shocks in the galactic and extra-galactic medium, AGN can accelerate CRs to the most extreme energies. So far, no correlation between the arrival direction of ultra-high energy cosmic rays (UHECRs) and AGNs has been found [25].

Gamma Ray Bursts (GRBs) are cosmic events of short duration (ms to few minutes). They are characterised by an extremely bright γ-ray emission followed by an afterglow in X, UV and optical radiation. On the basis on the duration of the burst they are classified as "short" or "long". Short GRBs (below few seconds of duration) are believed to be originated by the merging of two neutron stars or of a neutron star and a black hole. Since compact objects are involved, this results in γ-ray emissions of short duration. Long GRBs can be produced by the supernova collapse of extremely massive stars. In both cases the steady γ emission and the subsequent afterglow can be described by the *fireball* model. The central engine, activated by a huge release of gravitational
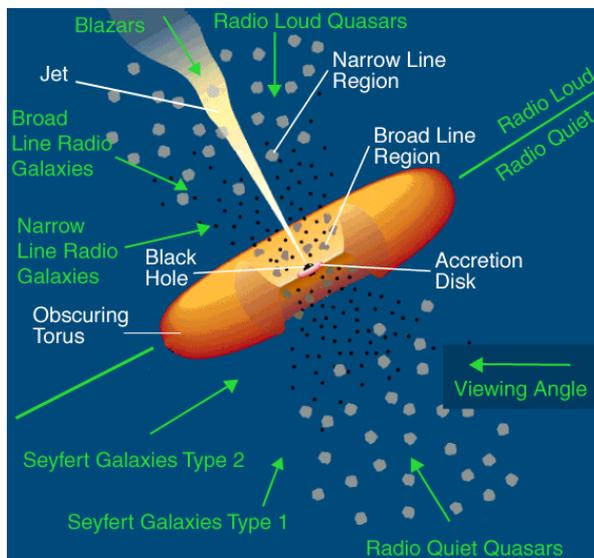
Figure 1.7: Schematic representation of the so-called unified model for AGN. Observing the same class of objects (radio loud or radio quiet AGNs) under different angles can lead to the observation of a vast variety of object. Image from www.auger.org

energy, can produce a jet of highly relativistic material, with Lorentz boost larger than $100 - 200$. This jet moves through a dense environment producing shocks, emitting γ-rays by synchrotron processess and inverse Compton effect. The afterglow emission, at lower frequencies, is caused by the time-delayed interaction of the jet with the surrounding medium. Since large and extremely fast shocks are present, CR can be accelerated during GRB events. The high Lorentz boost of the shock can enhance the maximal energy of accelerated particles up to the highest end of the CR spectrum.

1.1.3 γ-ray sources

Astrophysical objects can produce γ-rays by means of two mechanisms: *leptonic* or *hadronic* processes. Leptonic mechanisms, such as synchrotron radiation emission, bremsstrahlung and Inverse Compton (IC) scattering [26], are active when high energy electrons are accelerated near their source. In particular, synchrotron emission is present when electrons are deflected by strong magnetic fields; bremsstrahlung happens when relativistic electrons interact with the electric field of nuclei in the medium; IC is related to the inelastic scattering of fast electrons on local photons. Most of the electromagnetic radiation from cosmic sources can be explained with leptonic models.

Hadronic mechanisms are due to the interaction of CRs with the surrounding medium, where a large number of π^0 mesons is produced. They immediately decay (mean lifetime 8.4×10^{-17} s) into 2γ:

$$p + N \rightarrow X + n\,\pi^0.$$
$$\pi^0 \rightarrow \gamma\gamma \qquad (1.3)$$
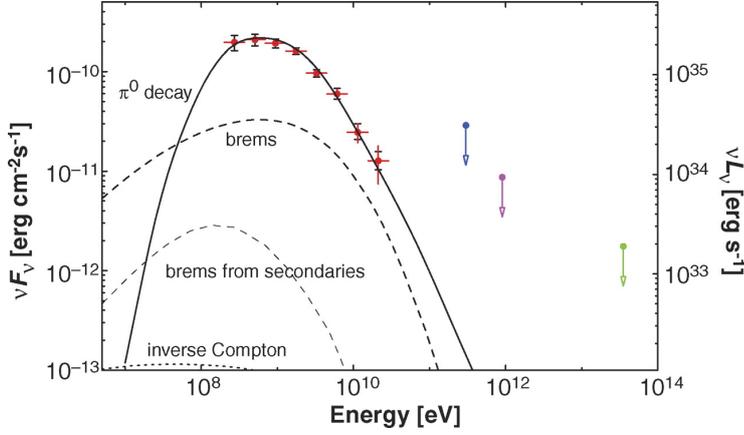
Figure 1.8: γ-ray spectral energy distribution of the SNR W44 as observed by the Fermi/LAT experiment, together with the upper limits from the Whipple (blue), HEGRA (magenta), and MILAGRO (green) experiments [27]. The experimental point are compared to the expectations from leptonic emission processes (dashed lines) – mainly from bremsstrahlung – and hadronic emission (solid line) from π^0 decay.

The observed γ-ray spectrum from hadronic production resembles that of primary CR at the acceleration site ($\Gamma \sim 2.0-2.5$), since the prompt interaction does not allow the absorption of protons before interacting and producing pions. Every possible CR accelerator would produce a large amount of γ-rays in hadronic processes. The resulting γ-rays should be higher in energy than those produced by leptonic processes. This has been observed by the Fermi/LAT satellite experiment [27] in a few SNRs. Figure 1.8 shows the spectral energy distribution (SED) of the SNR W44, where the observed flux from Fermi/LAT hints towards hadronic processes playing a role in γ-ray emission from this particular SNR.

Figure 1.9 shows a γ-ray sky map, from Fermi/LAT observations [28]. This map is centred at the Galactic Centre: an enhanced γ emission is clearly visible in the Galactic Plane. Once individual point sources are extracted, a diffuse component can be isolated. Most of this emission can be attributed to the decay of pions produced by CR interactions in the medium as shown in figure 1.10. A quite strong tension between observed data and models for the γ spectrum at high energies is present. An enhanced flux at high energies could be produced when considering the possible influence of "fresh" cosmic rays accelerated by young sources [29].

1.2   Neutrino astrophysics

Because of the presence of magnetic fields, charged particles do not point back to their sources. Cosmic rays below some 10^{18} eV – the highest energies expected for a CR accelerated in our Galaxy – are always deflected by galactic magnetic fields. The arrival direction of cosmic rays could be correlated with their sources only at the highest energies. On the other hand, neutral particles originating from prompt interactions of CRs with the surrounding medium carry information
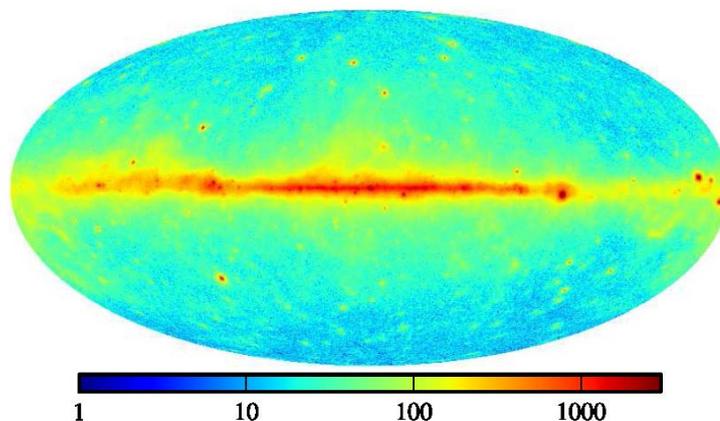
Figure 1.9: Sky map observed by the Fermi/LAT γ-ray observatory [28]. The map is centred at the Galactic Centre and the colour code represents the counting rate of the LAT instrument. Apart from strong individual sources, most of the counting rate is due to a diffuse emission in the Galactic Plane.
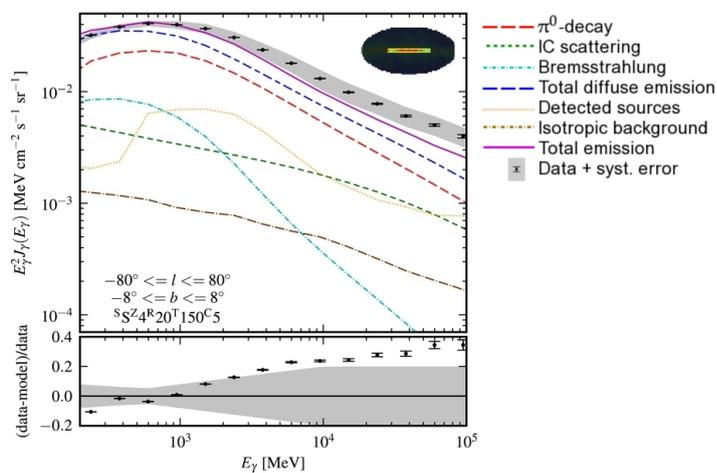
Figure 1.10: γ-ray energy spectrum for the Galactic Plane ($|\ell| < 80°$ and $|b| < 8°$) from Fermi/LAT [28]. Colour code as in the legend. A large contribution to the γ emission comes from the decay of π^0 produced by CR interactions. Also shown the comparison between data and expectations: the difference might be due to an additional component of CRs from young sources [29].

from their origin without any deflection from magnetic fields. Neutral radiation produced at CR accelerators can be composed of neutrons, γ-rays (§1.1.3) and neutrinos (§1.2.1):

- neutrons are short-lived and strongly interacting particles: they cannot reach the Earth and be detected;

- γ-rays have electromagnetic interactions with the ISM and can be absorbed along their path from the source to the Earth;

- neutrinos are only weakly interacting and can travel cosmic distances without being absorbed.

The observation of neutrinos from an individual cosmic object would be a "smoking gun" of CR acceleration taking place at that particular astrophysical site.

1.2.1   High energy neutrino sources

Along with π^0 (eq. 1.3), the interaction of a CR with the medium around its accelerator produces an equal number of charged pions so that:

$$\sum \pi^0 = \frac{1}{2} \sum \left(\pi^+ + \pi^- \right) .$$
(1.4)

Charged pions are short-lived (mean lifetime 2.6×10^{-8} s) and the products of their decay are leptons. A neutrino of the same flavour is always produced together with the charged lepton, obeying the conservation of lepton number. The leading decay processes producing neutrinos from pions are:

$$\pi^+ \to \nu_\mu + \mu^+$$
$$\mu^+ \to e^+ + \nu_e + \bar{\nu}_\mu$$
(1.5)
$$\pi^- \to \bar{\nu}_\mu + \mu^-$$
$$\mu^- \to e^- + \bar{\nu}_e + \nu_\mu$$
(1.6)

From these processes, the neutrino outcome of a source accelerating protons or nuclei can be predicted, either analitycally or numerically.

Modelling neutrino fluxes

The basic assumption to predict neutrino fluxes starting from the measurement of high energy γ-ray fluxes is that a certain fraction of the observed γ flux is of hadronic origin. Models such as that of ref. [30] allow the direct calculation of the expected neutrino spectrum starting from the observed γ flux $F_\gamma(E)$. Assuming that the source is transparent (i.e. γs are not absorbed in the source itself) and that the entire γ flux is produced by hadronic processes, the neutral pion flux at the cosmic object is:

$$F_{\pi^0}(E) = -\frac{E}{2} \frac{dF_\gamma}{dE}.$$
(1.7)

Each pion species would then follow this flux as they are equally produced by CR interactions because of isospin conservation. The ν_μ flux coming from π^+
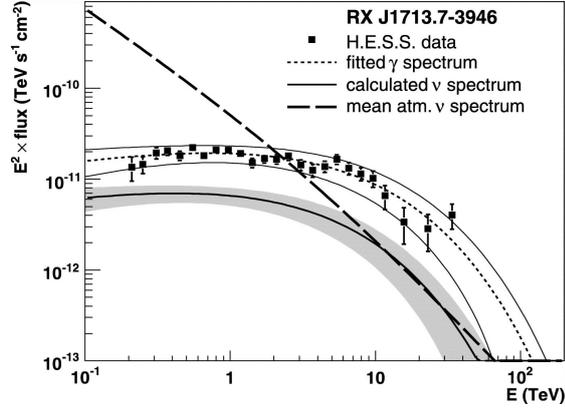
Figure 1.11: Predictions for the neutrino flux from the SNR RX J1713.7-3946 compared to the γ flux measured by HESS and the expected atmospheric neutrino background [31].

decay is:

$$F_{\nu_\mu} = \frac{F_\gamma\left[E/(1-r)\right]}{2(1-r)} \tag{1.8}$$

where r is the square of the ratio between the muon and the pion mass. The further production of neutrinos from the corresponding μ^+ flux can be expressed as:

$$F_\nu(E_\nu) = \int_0^1 \frac{dy}{y} F_\mu(E_\mu)\left[g_0(y) - \langle P(E_\mu)\rangle g_1(y)\right] \tag{1.9}$$

where $E_\mu = E_\nu/y$. The terms g_0 and g_1 are polynomials, specific for each neutrino flavour. The muon flux $F_\mu(E_\mu)$ is

$$F_\mu(E) = \frac{F_\gamma(E) - F_\gamma(E/r)}{2(1-r)} \tag{1.10}$$

while the polarization $\langle P(E_\mu)\rangle$, averaged over the pion distribution, is given by:

$$\langle P(E_\mu)\rangle \times F(E_\mu) = -\frac{F_\gamma(E) + F_\gamma(E/r)}{2(1-r)} + \frac{r}{(1-r)^2}\int_E^{E/r} F_\gamma(E')\frac{dE'}{E} \tag{1.11}$$

The further contribution to the γ spectrum from η meson decay is proportional to that of neutral pion through a coefficient that can be considered, at a first approximation, constant. Analogously the neutrino flux from charged kaons can be taken as proportional to that of $\pi^\pm$. An example of estimated neutrino flux from a SNR (RXJ 1713.7-3946) is reported in figure 1.11.

Diffuse neutrino fluxes

The neutrino flux from a single individual source might be too low to be detected. Nonetheless, the existence of many faint sources would show up in a diffuse neutrino flux. The observation of a diffuse flux of UHECRs can be used to set theoretical upper bounds on the total flux of neutrinos from extra-galactic sources. The upper bound proposed by Waxman and Bahcall (WB) [32, 33]

uses the cosmic ray observations at $E_{CR} \sim 10^{19}$ eV to constrain the neutrino flux. In the computation of the upper bound, several assumptions are made: neutrinos are produced when protons interact with ambient radiation or matter; the sources are transparent to high energy neutrons ($E_n \sim 10^{19}$ eV); the 10^{19} eV CRs produced by neutron decay are not deflected by magnetic fields; finally (and most important) the spectral shape of CRs at the acceleration site up to the GZK cut-off is $dN/dE \propto E^{-2}$, as typically expected from the Fermi mechanism. The resulting limit is:

$$E_\nu^2 \frac{d\Phi}{dE_\nu} < 4.5 \cdot 10^{-8} \text{ GeV cm}^{-2} \text{ s}^{-1} \text{ sr}^{-1} \qquad (1.12)$$

This value must be divided by 2 to take into account neutrino oscillation from the source to the Earth. The neutrino flux at the source should to be distributed between the three neutrino flavours as $\nu_e : \nu_\mu : \nu_\tau = 1 : 2 : 0$. Vacuum oscillation would produce at Earth equal subdivision in the three flavours.

A softer spectrum is expected if extra-galactic accelerators are inside galaxies that are opaque to CRs. This is the case of starburst galaxies [34], where the matter density is high enough for protons to interact, losing energy before producing pions that decay into neutrinos. The corresponding cosmic neutrino energy spectrum is steeper and lower in normalisation than the WB prediction. As starburst galaxies are usually detected in correspondence of galaxy mergers, and considering that galaxy mergers and AGN activity are correlated in radio [35], IR [36] and X observation [37], a large contribution to cosmic neutrino fluxes can be expected by these kind of objects.

Neutrinos from the Galactic Plane

A guaranteed flux of cosmic neutrinos is expected from the CR interactions in the Galactic Plane, where the π^0 contribution to measured γ fluxes is evident (§1.1.3) and the corresponding neutrino flux from $\pi^\pm$ can be computed. Using the observed γ spectrum, the primary proton spectrum can be inferred and using computational simulation of CR propagation in the Galaxy the neutrino flux can be extracted.

Different models for the CR propagation are proposed (e.g. [38, 39, 40]) as well as direct computations from Fermi data [28], each leading to a different neutrino flux expectation but in agreement within a factor ~ 2. *NoDrift* models [38, 39] do not take into account magnetic fields while *Drift* models [40], doing so, produce an enhancement of the neutrino flux in the Galactic Centre region. Figure 1.12 shows the expected neutrinos flux from the Galactic Plane region as a function of the galactic longitude. More information on the expected diffuse neutrino flux from the Milky Way is given in chapter 3.

Cosmogenic neutrinos

UHECRs interacting with CMB photons via the Δ^+ resonance, responsible of the GZK cut-off (§1.1.1), would produce neutrinos through the decay of pions generated in the reaction:

$$\gamma_{CMB} + p \rightarrow \Delta^+ \rightarrow n + \pi^+ \qquad (1.13)$$
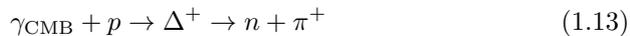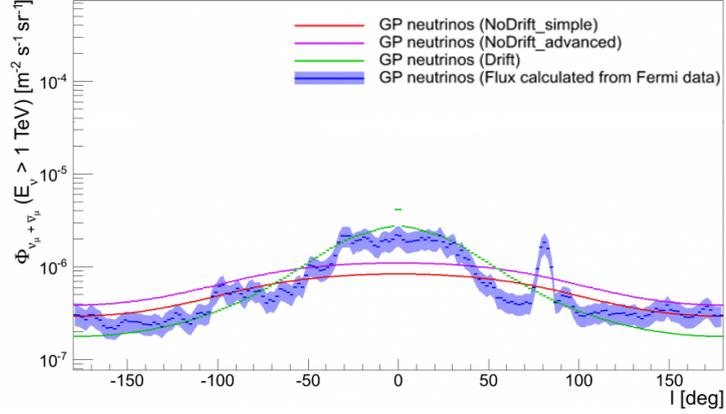
Figure 1.12: Expected neutrino flux from the Galactic Plane from different models and data from the Fermi/LAT γ-ray observations (see text for references) as a function of the galactic longitude [41].

An isotropic diffuse flux of these neutrinos would show up at extremely high energies, since both UHECR sources and CMB photons are isotropically distributed. Being the GZK threshold for protons around $5{\times}10^{19}$ eV and considering that, from simple kinematics, the resulting neutrino would carry about 1/20 of the proton energy, a flux peak at $E_\nu \sim$ EeV is expected. From the same reaction also electron neutrinos are produced from the neutron decay.

1.2.2   High energy neutrino detection

Neutrino interaction

A high energy neutrino interacts with a nucleon N via either charged current (CC) weak interaction

$$\nu_l + N \to l + X \tag{1.14}$$

or neutral current (NC) weak interaction

$$\nu_l + N \to \nu_l + X \tag{1.15}$$

At the first order, the differential cross section for CC interaction [42] is given by:

$$\frac{d^2\sigma_{\nu N}}{dxdy} = \frac{2G_F^2 m_N E_\nu}{\pi} \frac{M_W^4}{(Q^2 + M_W^2)^2} \left[xq(x, Q^2) + x(1-y)^2 \bar{q}(x, Q^2) \right] \tag{1.16}$$

where Q^2 is the square of the momentum transferred between the neutrino ν_l and the lepton l, m_N is the nucleon mass, M_W is the mass of the W boson, G_F is the Fermi coupling constant and $q(x,\, Q^2)$ and $\bar{q}(x,\, Q^2)$ are the parton function distributions for quarks and antiquarks. The so-called *scale variables* or Feynman-Bjorken variables are given by:

$$x = Q^2 / \left[2m_N(E_\nu - E_l) \right] \tag{1.17}$$

$$y = (E_\nu - E_l)/E_\nu \tag{1.18}$$
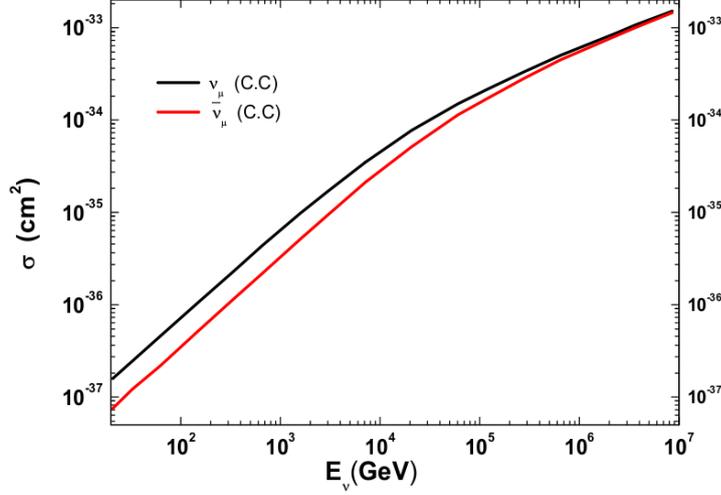
Figure 1.13: Charged current cross section for neutrinos (black) and anti-neutrinos (red) [42].

Figure 1.13 shows the ν_μ and $\bar{\nu}_\mu$ cross section as a function of the neutrino energy. The cross section grows linearly with the neutrino energy up to some tens of TeV, then slightly flattens because the square of the transferred momentum Q^2 becomes larger of M_W^2. Large theoretical uncertainties are present since few measurements are available for parton distribution functions at small x and high energies.

Cherenkov radiation

Charged particles are produced in neutrino interactions. Considering high energy interactions, the products are mainly relativistic particles. A charged particle that is above the speed of light in the medium can produce photons via Cherenkov emission [26]. Indeed the charged particle polarises the molecules along its trajectory, producing an overall dipole moment. Light is emitted when the electrons of the insulator restore themselves to equilibrium after the disruption has passed, producing coherent radiation. This radiation is emitted in a cone with a characteristic angle θ_C given by:

$$\cos\theta_C = \frac{c/n}{\beta c} = \frac{1}{\beta n} \tag{1.19}$$

where n is the refracting index of the medium and β is the particle speed in units of c. For relativistic particles ($\beta \simeq 1$) in sea water ($n \simeq 1.364$) the Cherenkov angle is about 43°. The number of Cherenkov photons N_γ emitted per unit wavelength interval $d\lambda$ and unit distance travelled dx, by a charged particle of charge e is given by:

$$\frac{d^2 N_\gamma}{dx d\lambda} = \frac{2\pi}{137\lambda^2}\left(1 - \frac{1}{n^2\beta^2}\right) \tag{1.20}$$

where λ is the wavelength of the radiation. Cherenkov radiation is significant at shorter wavelengths (visible, near UV). Typically, in the wavelength range

15
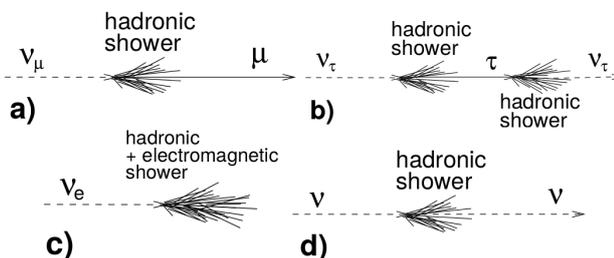
Figure 1.14: Event signature topologies for different neutrino flavours and interactions: a) CC interaction of a ν_μ produces a muon and a hadronic shower; b) CC interaction of a ν_τ producing a τ which then decays, tracing the the double bang event signature; c) CC interaction of ν_e produces both an EM and a hadronic shower; d) a NC interaction produces a hadronic shower [43].

between 300–600 nm, the number of Cherenkov photons emitted per meter is about 3.5×10^4.

Muon detection

A high energy muon is produced after the CC interaction of a muon neutrino. The direction of the μ is highly correlated with the neutrino arrival direction and the angle $\theta_{\nu\mu}$ between the incoming neutrino and the induced muon is [43]:

$$\theta_{\nu\mu} \simeq \frac{0.6°}{\sqrt{E_\nu(\text{TeV})}}. \tag{1.21}$$

Assuming that the muon is well above the Cherenkov emission threshold, the detection of this photons allows the reconstruction of its direction and consequently that of the neutrino. High energy muons can be well reconstructed since they travel straight through the detector, producing a clear track signature.

Muons lose energy because of ionisation, pair production, bremsstrahlung and photo-nuclear interactions. The energy loss per unit path length can be parametrised as:

$$dE_\mu/dx = \alpha(E_\mu) + \beta(E_\mu) \cdot E_\mu \tag{1.22}$$

where $\alpha(E_\mu)$ describes the ionisation loss, slightly depending on the muon energy, while $\beta(E_\mu)$ describes radiative losses – pair production, brehmsstrahlung and photo-nuclear interactions. Depending on the traversed material a different critical energy E_C exists where the radiative losses become larger than ionisation losses. $E_C \sim 500\,\text{GeV}$ in water.

Figure 1.15 shows the *effective range* (R_{eff}) of muons in water. This quantity is the distance after which a muon of initial energy E_μ is still above the energy threshold E_μ^{thr} for detection in the apparatus. A 10 TeV muon travelling 4 km in water can reach the detector with an energy above 1 TeV. The event will be observed even if the neutrino interaction vertex where the muon has been produced is far from the instrumented volume, increasing the effective size of the detector.

16
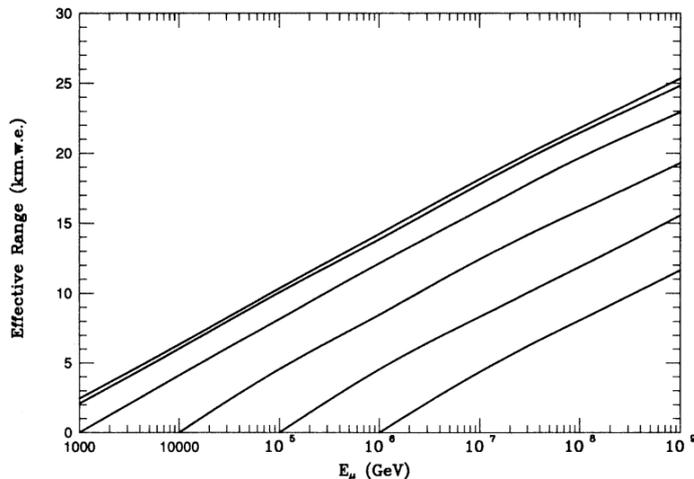
Figure 1.15: Effective range of muons as a function of the muon energy, for different energy thresholds (from 1 to 10^6 GeV) [44].

Shower detection

When a NC interaction for all neutrino flavours or a CC interaction of electron (anti)neutrino takes place, hadronic and electromagnetic showers are produced. In CC ν_e an electromagnetic (EM) shower is produced since a high energy electron is induced by the neutrino interaction. This electron can radiate bremsstrahlung γs, again producing e^+e^- pairs and generating a further cascade of EM particles. As long as the charged particles in the EM showers are above the Cherenkov threshold, light is emitted. Hadronic showers are represented by the term X of equations 1.14 and 1.15 and are present in both CC and NC interactions. The largest contribution to hadronic showers is given by pions, but also other mesons and baryons can be produced. An electromagnetic component is present in the hadronic shower because π^0 mesons are produced and they immediately decay into 2γ. All the particles in the hadronic shower can produce additional particles via radiation mechanism and can further interact with the medium. Until the charged particles in the cascade are above the speed of light in the medium, detectable Cherenkov light is produced. Whilst for CC muon neutrino interactions a track-like event is produced, shower events can usually be characterised by an expanding spherical shell of light, centred around the shower maximum. Also in this case the shower direction can be reconstructed and correlated to the neutrino arrival direction.

Tau detection

A CC ν_τ interaction produces a τ lepton. Tauons are short-lived leptons $(2.9\times10^{-13}\,\text{s})$ and decay producing a shower of particles. At high energies, their Lorentz factor can be large enough to produce a visible track before the lepton decays. In this case a shower-like event is present both at the interaction vertex and at the decay point. A track-like event would also be visible since the tau lepton produces Cherenkov light. Below 1 PeV the interaction vertex hadronic

17

shower and the decay shower are too close to be distinguished in a sparsely instrumented volume. At higher energies and for large detectors the two showers can be separated and a "double bang event" – each "bang" corresponding to a shower – is detected. If one of the two showers, either the interaction or the decay one, is outside the detection volume, only a track and a cascade are visible producing a "lollipop event".

Chapter 2

Neutrino astronomy

2.1 Neutrino telescopes

A neutrino detector can be operated as a telescope if the neutrino arrival direction is reconstructed with good angular precision ($<1°$). The angular resolution on the neutrino direction is limited by the intrinsic spread between the direction of the incoming neutrino and the interaction products that are reconstructed (eq. 1.21). The possible detection of high energy neutrinos is limited by the fact that the expected fluxes and the neutrino interaction cross-sections are very low. Very large detectors are needed, ranging up to a cubic km of instrumented volume. The use of large volumes of natural water was proposed by M.A. Markov in 1960 [45]. A large number of light detectors would make large portions of oceans, lakes or ice shells sensitive to the emission of Cherenkov photons transforming them into neutrino detectors. The medium:

- is the target for neutrino interactions;

- shields from CR air shower background;

- allows the production and the transmission of Cherenkov light produced by relativistic charged particles emerging from the neutrino interaction.

Large volume detector are required for the detection of cosmic neutrino fluxes. The ideal size for a neutrino telescope is of the order of a km^3, or more. Such a large size would allow a few of these neutrinos to interact within the sensitive volume of the detector in a year of operation. Nonetheless, the Cherenkov photons given by the neutrino interaction products sould be properly detected. A large number of highly sensitive light detectors must be put in the target medium so that the density of light detecting devices – typically photomultiplier tubes (PMT) – is large enough to have enough signals to reconstruct events. As the typical PMTs used in this sort of experiments are 10-inch in diameter, a rough estimation of the requested number of PMTs is ~ 5000 PMTs per cubic kilometre [43].

2.1.1 Light propagation in water and ice

Water and ice absorb (*absorption* processes) and deviate photons (*scattering* processes). The performance of the telescope in obtaining a high quality recon-
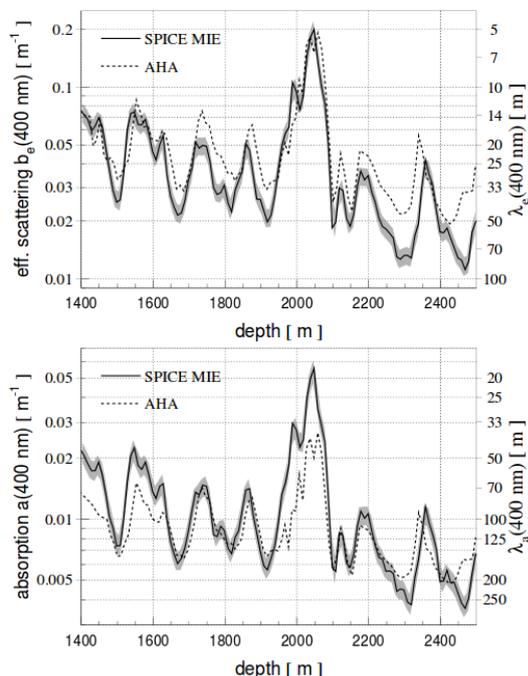
Figure 2.1: Effective scattering (top) and absorption (bottom) coefficients as a function of the depth in the South Pole ice, as measured with LED flashers [47]. The results of the measurement are dependent on the assumed models for scattering and absorption.

struction of the neutrino direction are significantly affected by the propagation properties of the medium. Absorption reduces the amplitude of the Cherenkov wavefront, i.e. the total amount of light hitting on PMTs. Scattering changes the direction of propagation of the Cherenkov photons, modifying the distribution of their arrival time on the PMTs. This causes a degradation in the reconstruction of the direction of the incoming neutrino. *Direct* photons are those arriving on a PMT without being scattered.

At a given wavelength λ, light propagation in the medium is characterised by the optical properties of the medium through the absorption a(λ), scattering b(λ) and attenuation c(λ) coefficients. The corresponding absorption, scattering and attenuation length can also be used to define the optical properties of the medium. These quantities are correlated:

$$c(\lambda) = a(\lambda) + b(\lambda) \tag{2.1}$$

$$L_i = i(\lambda)^{-1} \quad i = a, b, c \tag{2.2}$$

Each of these lengths represents the path after which a beam of initial intensity I$_0$ is reduced by a factor $1/e$ because of absorption or scattering.

A complete description of light scattering would require, in addition to the geometric scattering length L$_b(\lambda)$, the knowledge of the scattering angular distribution. An analytical solution of the Maxwell equations for the scattering

of electromagnetic radiation by spherical particles was developed by Gustav Mie [46]. This solution is appropriate for modelling light scattering in transparent media. The predominant scattering centres are sub-millimeter sized air bubbles and micron sized dust particles. In ice the concentration of scattering centres is much higher than in water. Light can be scattered several times before it reaches an optical sensor. The average cosine of the light field of photons undergoing multiple (n) scattering obeys a simple relationship:

$$\langle \cos\theta \rangle_n = \langle \cos\theta \rangle^n \tag{2.3}$$

On average, between two scattering events, a photon advances a distance $L_b(\lambda)$ at an angle $\langle \cos\theta \rangle$. Hence after n scatters, a photon has moved in the incident direction

$$L_b^{\text{eff}}(\lambda) = L_b(\lambda) \sum_{i=0}^{n} \langle \cos\theta \rangle^i \simeq \frac{L_b(\lambda)}{1 - \langle \cos\theta \rangle} \tag{2.4}$$

Experimental measurements are generally expressed in terms of the effective light scattering length $L_b^{\text{eff}}(\lambda)$, instead of the (strongly correlated) values of average scattering angle $\cos\theta$ and geometric scattering length $L_b(\lambda)$.

In general, ice is more transparent than water, i.e. its light absorption length is much longer. On the other hand the scattering is much stronger in ice as dust and air bubbles are trapped into the ice. In addition, while water is a homogeneous medium, the Antarctic ice shell was formed after the accumulation of snow over an extremely long period of time, with differences in the concentration of dust over time. For this reason the optical properties of ice can have large variation over the almost 3 km of depth, as proved by measurement of light propagation properties with LED flashers in the deep ice (figure 2.1). A rather thick "dust layer" is also present at the South Pole at a depth of about 2000 m, strongly reducing the light detection efficiency in that region.

2.1.2   Under-water detectors

First tentatives – The under-water option has been investigated both in marine and deep lake environment. The pioneering DUMAND project [48] started in 1976 and lasted until it was cancelled by U.S. Department of Energy in 1995. Preliminary studies were carried in order to deploy a detection unit in the Pacific Ocean, off Hawaii Islands, at a depth of about 4800 m. Even if DUMAND did not reach its final construction phase because of technical and financial problems, all the subsequent projects took advantage of the experience coming from its R&D phase.

Lake Baikal – The deep waters (~ 1800 m) of Lake Baikal, Russia, hosts a neutrino telescope [49]. Test detection units have been put under-water in the early nineties (NT-200 project) and preliminary measurements in the search for high energy neutrinos have been completed [50]. A Gton volume detector is foreseen to be built in Lake Baikal in the next years [51]. A thick ice shell is present on the lake during the winter time and allows easy deployment of instruments in the water. Low optical background is expected in fresh water with respect to sea water (see §4.2.3), but the water of Lake Baikal is less transparent than sea water or ice, limiting the reconstruction performance.
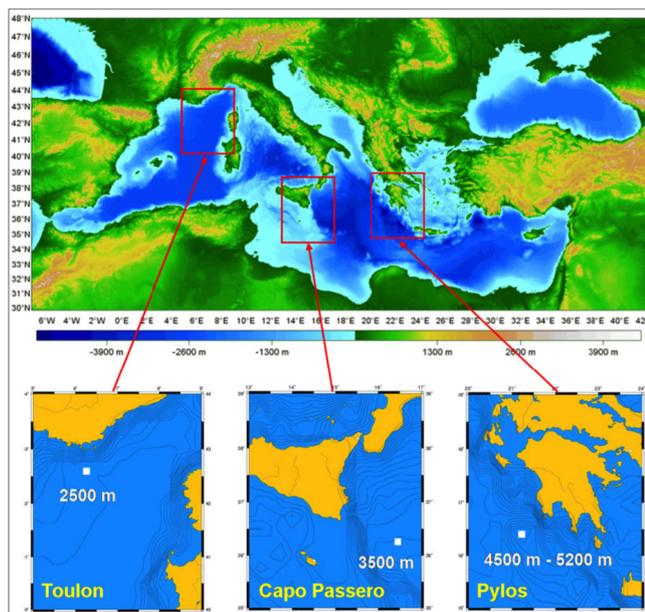
Figure 2.2: The three Mediterranean sites for neutrino detectors: ANTARES in the Toulon site, NEMO at the Capo Passero site and NESTOR in Pylos. KM3NeT, the next generation neutrino telescope, will follow a multi-site approach, instrumenting different volumes in each of the three sites.

The Mediterranean Sea – A favourable environment for building a neutrino telescope is represented by the Mediterranean Sea. Large abyssal planes are present, with depths ranging from 2500 to 4500 m. Low deep sea current are usually measured and many on-shore infrastructures are distributed along the Mediterranean coasts. At least three different sites have been investigated, off shore France, Italy and Greece (figure 2.2). All these sites are quite close to the shore and to large Physics institutes. Deploying the detector and its related infrastructure in the sea requires marine operation with a Remotely Operated Vehicle (ROV).

- The ANTARES detector [52], subject of this work, will be described in details in the next section. Anchored to the sea-bed at a depth of about 2500 m 40 km off-shore Toulon, France, it is currently the largest underwater neutrino telescope and the largest neutrino detector in the Northern hemisphere. Operating continuously since 2006, it was completed in 2008 and will be taking data at least up to 2016.

- The Greek site, off-shore Pylos, Peloponnese, comprise one of the deepest planes in the Mediterranean Sea, ranging down to 4500 m of depth. The NESTOR Collaboration [53] has deployed some test units and measured the muon flux at a depth of more than 3000 m.

- The NEMO Collaboration [54] has studied the deep sea environment in front of the Sicilian coasts, about 100 km off-shore Capo Passero. An intensive R&D activity has been conducted to define possible solutions

(a) KM3NeT DOM   (b) KM3NeT DU

Figure 2.3: Left: the KM3NeT DOM, made of 31 3-inch PMTs inside a 17-inch glass sphere. Each DOM hosts all the off-shore electronics and is installed along a detection unit (DU), a vertical string anchored to the sea-bed. Right: a complete DU at the end of its construction [58]

to be used in a neutrino telescope design. Test towers, vertical structure holding PMTs, have been deployed and the atmospheric muon flux has been measured [55]. Water properties have been studied showing low optical background [56] and stable conditions over long periods have been observed [57]. Moreover a large deep sea infrastructure has been built in the site, towards the next generation neutrino telescope, KM3NeT.

- KM3NeT [58] is a multi-site deep sea infrastructure that will host neutrino telescopes and Earth and sea science experiments. It will comprise the ARCA and ORCA projects (Astronomy and Oscillation Research with Cosmics in the Abyss) respectively dedicated to the investigation of high energy neutrino astrophysics [60] – searching for the sources of cosmic neutrinos – and low energy neutrino oscillation physics [61] – for the measurement of the neutrino mass hierarchy. The modularity of the projects will be possible following the concept of a detector *building block*. A building block is made of 115 detection units (DU) [62], vertical strings holding 18 multi-pmt Digital Optical Modules (DOM) [63]. Each DOM is made of 31 3-inch PMTs as displayed in figure 2.3. In the case of ARCA, DOMs will be put at a distance of 36 m on each DU, with an average distance of 90 m between DUs. DUs for ORCA, since an extremely low threshold (few GeV) and high granularity are required, will be put at a average distance of 20 m from each other and the inter-DOM distance will be of 9 meters. The water properties of the Mediterranean Sea along with the ns time resolution given by small PMTs will allow extremely good reconstruction performance, opening the way to point source neutrino astronomy in all neutrino flavours. The KM3NeT project is in its Phase-I
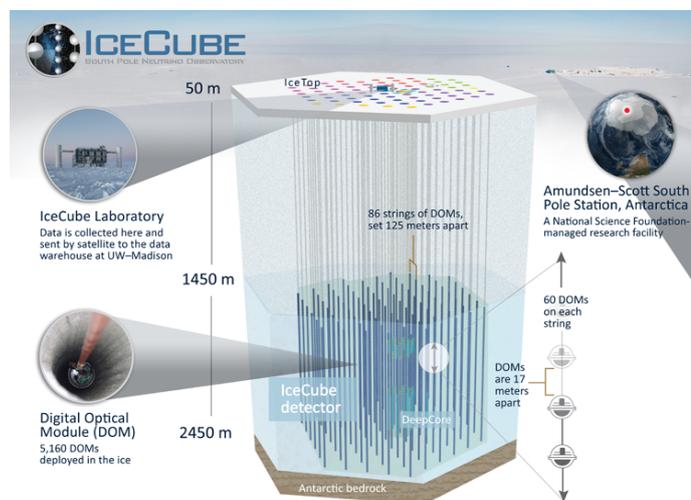
Figure 2.4: Schematic view of the IceCube detector at the geographical South Pole [65]. Strings are put in the ice shell at a depth of about 2 km, for an instrumented volume of 1 km^3. The low energy extension of IceCube, Deep Core, made of more compact and closely spaced strings, is also visible. An extensive air shower detector, IceTop, is present on top of the ice cover to analyse the atmospheric background. Image from https://icecube.wisc.edu/.

construction stage. More details are available in ref. [60, 61].

2.1.3   Under-ice detectors

A large neutrino detector is taking data in the Antarctic ice shell. This is the case of the AMANDA [64] detector and of its successor IceCube [65], currently the largest neutrino detector in the world. The detector is located at the geographic South Pole, at the permanent Amudsen-Scott Pole Station. The IceCube apparatus comprises 86 strings, each holding 60 10-inch PMTs in a glass sphere, constituting a Digital Optical Module (DOM). The distance between DOMs on a string is 17 m and strings are distributed on a hexagonal footprint at an average distance of 125 m from each other. The total instrumented volume is about one cubic kilometre. Strings have been deployed drilling the ice shell with hot water, putting the string in the hole and then letting the ice to freeze again in order to fix the position of DOMs. Ice Cherenkov tanks are placed on top of the detector, providing a cosmic ray detector that can help in rejecting the background coming from downward-going atmospheric events.

The absorption length of light is up to three times larger than in water: light can travel a much longer distance without being absorbed, enlarging the effective volume of the detector. However, due to the presence of dust and air bubbles that are trapped in ice, light scattering is much more probable than in water and most of the detected photons are indirect [47]. This limits the reconstruction performance of the detector in terms of angular resolution, especially in the case of shower events. The first observation of cosmic neutrinos has been obtained by the IceCube Collaboration. Details on this cosmic signal will be given in §2.2.
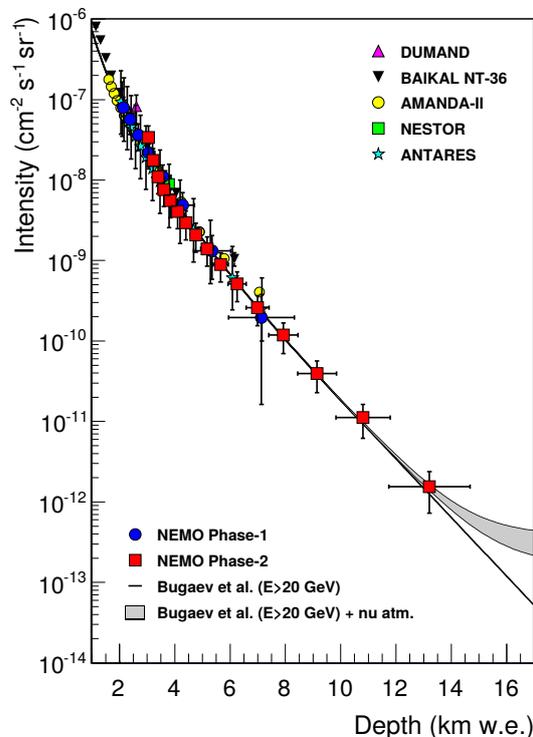
Figure 2.5: Vertical intensity of atmospheric muon as a function of the depth, in km of water equivalent, as measured by different under-water experiments [55].

2.1.4 Background events

The most abundant signal in a neutrino telescope is given by atmospheric muon bundles produced by the decay of short-lived particles in CR extensive air showers. High energy muons are highly penetrating particles and can reach the detector even if it is located under a couple of km of shielding material. When these penetrating muons are above the Cherenkov threshold, their light can be detected by the optical sensors. In order to remove this huge background a geometrical selection is applied. Atmospheric muons can only be downward-going tracks and upward-going muon tracks are due to neutrino-induced muons only, since neutrinos are the only particles that can traverse the Earth. Indeed, already at ~ 14 km water equivalent all atmospheric muons are absorbed and muon tracks are only induced by neutrinos (figure 2.5). For this reason, the search for neutrinos is mainly done looking downward. Nonetheless, the Cherekov radiation produced by atmospheric muon bundles induces signals on the PMTs that the reconstruction algorithm can reconstruct as fake upward-going particles. Strategies to reject this background of wrongly reconstructed atmospheric muons from neutrino induced muons are defined and tested in every neutrino telescope.

An irreducible background for the observation of cosmic neutrinos is given by

atmospheric neutrinos produced by the decays of short-lived particles (mainly pions and kaons) produced by the interaction of primary CRs in the atmosphere. The energy spectrum of these atmospheric neutrinos is, asymptotically, one power law steeper than that of cosmic rays. Cosmic neutrinos that are produced at the CR acceleration sites are expected to follow the same power law spectrum as primary particles at the source. Since the energy spectrum of primary CRs at the top of the atmosphere is steeper than what expected at the acceleration sites because of the propagation of primaries in the galaxy, cosmic neutrinos can be differentiated from atmospheric neutrinos by an energy estimation. Beyond 100 TeV (20 TeV), cosmic muon (electron) neutrinos are expected to be more abundant than the atmospheric component. The atmospheric background for tau neutrinos can be considered negligible, apart from small effects at low energies coming from the oscillation of atmospheric ν_μ and a possible prompt component at extremely high energies. Details on the modelisation of atmospheric neutrino fluxes will be presented in §5.1.

2.2 The IceCube signal

2.2.1 Signal characterisation

The IceCube detector has obtained so far the sole observation of high energy cosmic neutrinos. The first evidence of such a signal was found in the search for very high energy neutrino events of cosmogenic (GZK) origin [66]. Two PeV cascade-like neutrino events were found when the expectation from atmospheric backgrounds was almost negligible. These two events (nick-named "Ernie" and "Bert", sketched in figure 2.6) were at the low energy end of the analysis sensitivity range and could not be related to any of the models for cosmogenic neutrino fluxes. The null signal hypothesis (i.e. pure atmospheric origin) could be discarded at 2.8σ significance level.

The further analysis of IceCube data searched for high energy starting events (HESE) [67, 68, 69]. In this search a veto strategy is applied to reject downgoing atmospheric muons and neutrinos. Indeed atmospheric neutrinos from extensive air showers are expected to be accompanied by muon bundles produced in the same CR interaction. In the presence of a recognisable signal coming from downward-going atmospheric muons, namely in the external layers of the detector, an event is discarded since it is extremely likely to be atmospheric. On the other hand, high energy events starting inside the instrumented volume in general are not related to air showers and represent a clear signal of cosmic events. In the case of upward-going events this is not true anymore, but since a high-energy selection is applied and since at the PeV energy range the Earth is almost opaque to neutrinos, this part of the sky does not contribute too much to the sensitivity and to the background.

The first HESE data sample (including the first two years of data acquisition with the complete IceCube detector [67]) counts 28 events over an expected background of $10.6^{+5.0}_{-3.6}$ from atmospheric neutrinos and muons. The significance of the discovery corresponds to a 4.8σ excess over the background only hypothesis. The addition of a third [68] and fourth year [69] of data increases the significance of the discovery to 5.7 and 6.5σ respectively, the latter reporting a final sample of 54 cosmic neutrinos candidates with an expected background of $9.0^{+8.0}_{-2.2}$ and
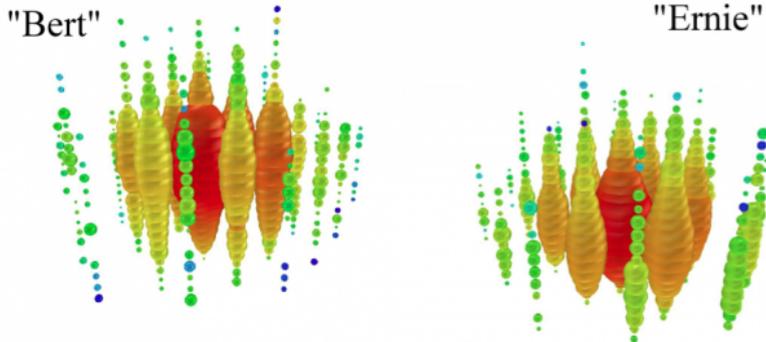
Figure 2.6: Event display from the IceCube neutrino telescope for the first two observed PeV neutrinos, nick-named "Bert" and "Ernie" [66]. Each sphere represents and hit DOM: the colour code shows the timing of hits, while the size of the sphere represents its measured charge. The shower signature is evident as a large amount of light is emitted and propagates spherically from the interaction vertex.

12.6±5.1 events from atmospheric neutrinos and muons respectively.

The energy spectrum obtained with the 2 years HESE sample can be represented with an unbroken power law:

$$\Phi_\nu = \Phi_0 E^{-\Gamma} \text{ GeV cm}^{-2} \text{ s}^{-1} \text{ sr}^{-1} \qquad (2.5)$$

where the spectral index $\Gamma = 2.0$ and the normalization, per neutrino flavour, $\Phi_0 = (1.2 \pm 0.4) \times 10^{-8}$. Adding the 3rd year of data with the complete detector more low energy events are observed while a lack of multi-PeV neutrinos suggests a steeper spectral index or a cut-off at the highest energies. The best fit per flavour is reported to be as:

$$E^2\Phi(E) = 1.5 \times 10^{-18}(E/100 \text{ TeV})^{-0.3}\text{GeV cm}^{-2} \text{ s}^{-1} \text{ sr}^{-1}. \qquad (2.6)$$

In particular, the absence of Glashow-resonance events, produced by resonant $\bar{\nu}_e$CC interaction at about 6.4 PeV, favours these hypotheses. Also the 4th year of HESE data strengthens this scenario.

A significant excess of events appears also in the upward-going tracks channel, where only muon neutrinos undergoing CC interaction are observed. This data set is independent of the HESE sample since it is made of passing through muons, which would be rejected by the adopted veto strategy. In addition, this analysis looks only at upward-going tracks, thus at the Northern sky. In this case a slight tension is observed with respect to HESE data, since the best fitting spectral index is 2.2±0.2 – for $\Gamma = 2.0$ the best fit normalisation at 100 TeV is $\Phi_0 = 9.9^{+3.9}_{-3.4} \times 10^{-19}$ per flavour. This hypothesis can be rejected at a significance level of 3σ with the HESE analysis.

The data sample is consistent with equipartition in the three neutrino flavours [72], as expected from neutrino oscillation over cosmic distances and standard neutrino production scenarios. In particular, at PeV energies, showers and
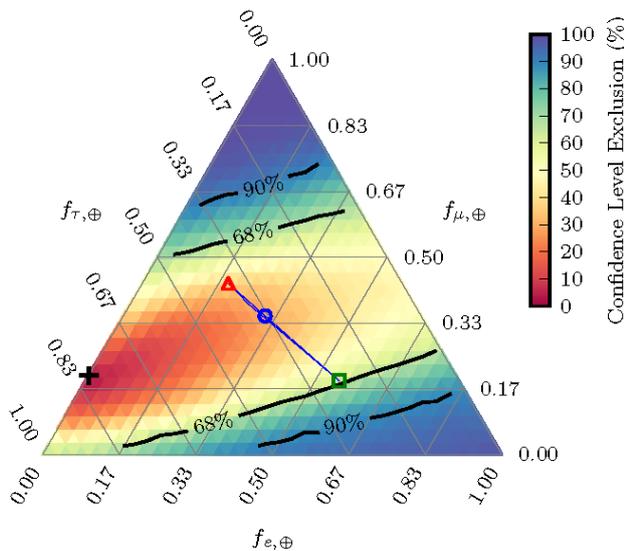
Figure 2.7: Exclusion regions for astrophysical flavour rations $(f_e, f_\mu, f_\tau)_\oplus$ at Earth. The numerical labels for each flavour refer to the tilted lines inside the triangle. Neutrino oscillations averaged over cosmic distances map the flavour ratio at sources points within the narrow blue triangle at the centre of the figure. $(1:1:1)_\oplus$ composition at Earth resulting from a $(1:2:0)_S$ source composition is marked with a blue circle; the compositions at Earth coming from a source composition of $(0:1:0)_S$ and $(1:0:0)_S$ are marked with a red triangle and a green square. Though the best fit composition at Earth (black cross) is $(0:0.2:0.8)_\oplus$, the limits are consistent with all possible source compositions [72].

tau double-bang events can be hardly distinguished in the IceCube detector: tau events represent a background free channel for cosmic searches and the measurement of the fraction of ν_τ interactions, and thus the knowledge of the exact content of showers in the sample, would disentangle $p - p$ from $p - \gamma$ production scenarios as explained in ref. [73].

The sky map of the 54 cosmic neutrino candidates is reported in figure 2.8. No significant clustering of events could be identified in the data sample, suggesting a diffuse isotropic flux of neutrinos. This could be due a bias in the search strategy that favours cascade events, for which the angular resolution of the IceCube detector is of the order of 10–20 degrees. Indeed, also a standard point source search in the muon channel did not report any significant hints of individual sources of cosmic neutrinos [74]. Some accumulation of events seems however to be present in a few regions of the sky and a "hotspot" could be identified in the 2 and 3 years sample, specifically at galactic coordinates ($\ell = 18°$, $b = -9°$), computing the average direction of the reconstructed events weighted according to their estimated energy and angular error.

2.2.2 Possible interpretations

A diffuse flux of high energy neutrinos can be attributed either to the propagation of high energy primary CRs in the Universe or to an ensemble of
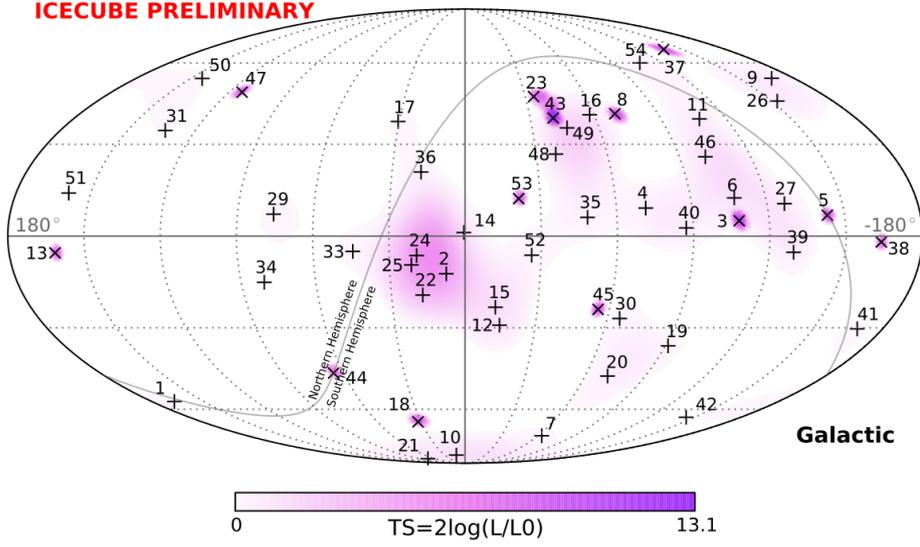
Figure 2.8: Sky map in galactic coordinates for the 4 years IceCube HESE sample [69]. Colour code reports the pre-trial probability of an excess over the expected background. No significant clustering of events is evident.

neutrino sources which cannot be individually resolved by the detector or that are too faint to produce a detectable signal.

Typically, models of extra-galactic sources (as AGN or γ-ray bursts) foresee that neutrinos are generated via photo-hadronic interactions of high energy protons with low-energy photons of the background. These models are characterized by relatively high-energy thresholds (due to the charged pion production) and disfavour a soft neutrino spectrum [75, 76]. Neutrinos produced by proton-proton (or nucleus) interactions have a spectrum that also follows that of the parent hadron spectrum but lower energy threshold [77]. This mechanism leads to the production of neutrinos through the decay chain of induced charged mesons (mainly pions) with spectral index $\Gamma \simeq 2$ for neutrinos produced by point-like sources. Stringent limits on the point source origin of the IceCube cosmic signal have been set with ANTARES data in the Southern sky [78].

It has been pointed out [70] that a Northern/Southern sky anisotropy might be present in the selected data sample of [68]. This can be also seen when looking at the energy distribution of events presented in figure 2.9: for deposited energies around 50 TeV some discrepancy is visible in data coming from the Southern hemisphere with respect to the expectations from atmospheric and cosmic events under the assumption of isotropy. Looking at events above 60 TeV, 20 events are detected, 5 coming from the Northern hemisphere and 15 from the Southern hemisphere. Part of this difference is due to neutrino absorption through the Earth, which is significantly relevant in this energy regime. The expected background is of 1.4 and 1.3 events respectively, which correspondingly produces an effective signal rate of 3.6 and 13.7 events. Since the Northern sky does not include a significant portion of the Galaxy, that part of signal can be considered completely extra-galactic. Considering the IceCube neutrino effective areas shown in ref. [67], the extra-galactic component in the Southern sky can be
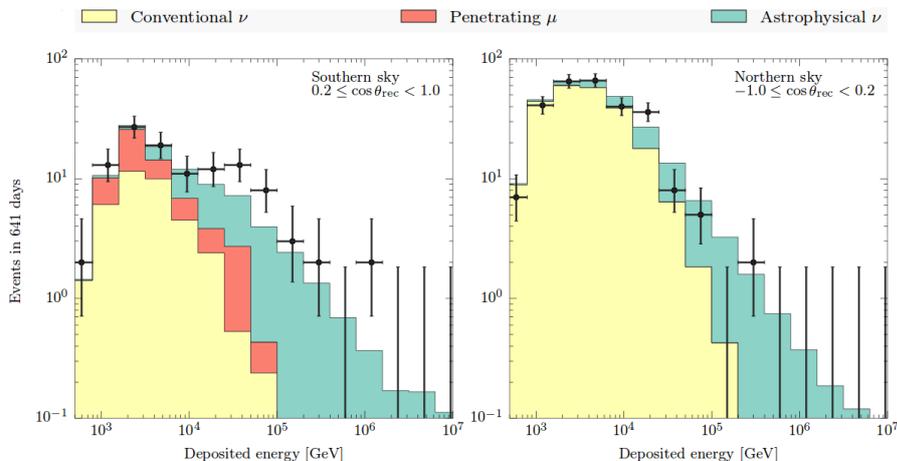
Figure 2.9: Deposited energy distribution of IceCube events selected (black crosses) in the analysis of [71], left panel for the Southern sky, right for the Northern sky. The yellow area represent the sum of all atmospheric neutrino contributions, the red area is (stacked) the contribution from atmospheric muon penetrating the veto while the light blue histogram is the best fit (all-sky) to the signal. An excess of events appears between 50 and 100 TeV of deposited energy in the Southern sky, not seen in the Northern hemisphere.

estimated to produce 6.2 events. The excess of events (~ 7.5 events) could then be attributed to an anisotropy which can be due to the presence of the Galactic Plane.

In ref. [79] it has been pointed out that in the 4 years IceCube sample a 3σ excess of events could be present in the band between ± 10 degrees around the Galactic Plane at energies above 100 TeV with respect to the isotropic assumption. In this calculation up to 1/4 of the overall IceCube flux could be explained by a further galactic component, possibly related to the diffuse flux of neutrinos coming from the Galactic Plane.

Apart from the abundance of possible neutrino sources along the Galactic Plane, a diffuse flux of neutrinos is expected from CR interaction in the interstellar medium. CRs propagating and interacting in the Galaxy would produce a neutrino flux that should follow the energy spectrum of the primaries. The CR spectrum in the Galaxy is softer than what is expected at extra-galactic sources: a softer neutrino spectrum should be expected from the Southern sky, dominated by the Galactic Plane, with respect to the Northern sky, where the extra-galactic component is more relevant.

Space and time correlations with many objects have been searched for. High energy neutrinos can be produced by transient sources of γ-rays, being GRBs and AGN probably accelerating cosmic rays to the highest energy, thus expected to produce neutrinos. The search for coincident neutrinos from GRBs has not reported any correlation and stringent limits on neutrino emission models from these objects have been put by the IceCube Collaboration [80].

Correlations between IceCube HESE and blazars – active galactic nuclei whose jet is aligned along the line of sight – has been searched for with the TANAMI radio array. The analysis reported a possible coincidence with high-

fluence blazars, though compatible with background expectations. The analysis of ANTARES data, not reporting any significant excess, constrains the intensity of neutrino production at this object [81].

The authors of [82] reported that one of the most energetic event of the IceCube HESE sample happened a few hours after the most intense X-ray flare ever registered from Sag A*, the central supermassive black hole of our Galaxy, with a chance probability of 0.9%. Modelling the possible emission of neutrinos from hadronic mechanisms to produce this kind of events, a TeV γ-ray flux from Sag A* is expected to be observed by ground Cherenkov γ-ray telescopes.

Chapter 3

Neutrinos from the Milky Way

The neutrino flux coming from cosmic ray propagation in the central region of our Galaxy can be estimated in two different ways: either with a theoretical/computational approach based on assumed cosmic ray spectra, matter distribution in the Galaxy and intensity of galactic magnetic fields or with a phenomenological one based on gamma ray observations coming from the Fermi-LAT instrument – according to which only the fraction of γ-ray coming from cosmic ray interactions needs to be known.

3.1 Model ingredients

3.1.1 Our Galaxy

Galaxies are classified according to their Hubble type [83], introduced in 1925 by Edwin Hubble. A schematic representation of this is shown in figure 3.1. Most of the known galaxies are elliptical, denoted by the letter E followed by a number representing the ellipticity: 0 is nearly spherical and 7 is the most ellipse-like. Most of the remaining galaxies are spiral galaxies, grouped into two classes: those with a bar (about one-third of the spirals) and those without. Spiral galaxies are indicated with the letter S and a second letter (a, b or c) specifying how tightly wound the spiral arms are, with type Sa having the most tightly wound arms. For barred spiral galaxies, an additional B follows the S. A few percent of galaxies do not show any regularity. These irregular galaxies are classified as Irr.

Since the Milky Way contains the Earth, its precise classification is difficult. It is known that we live in a barred spiral galaxy, but not exactly how tightly wound the spiral arms are. It should be between type SBb and SBc, also denoted by SBbc [84]. The Milky Way, like other galaxies, consists of stars, gas, dust and some form of dark matter. For (barred) spiral galaxies the components are organised into a disk, containing the spiral arms, a bulge and a halo. For elliptical galaxies the disk is not present, since they only consist of a bulge and a halo. The structural components of our Galaxy are:

- *The dark-matter halo.* The main structural component is the dark-matter
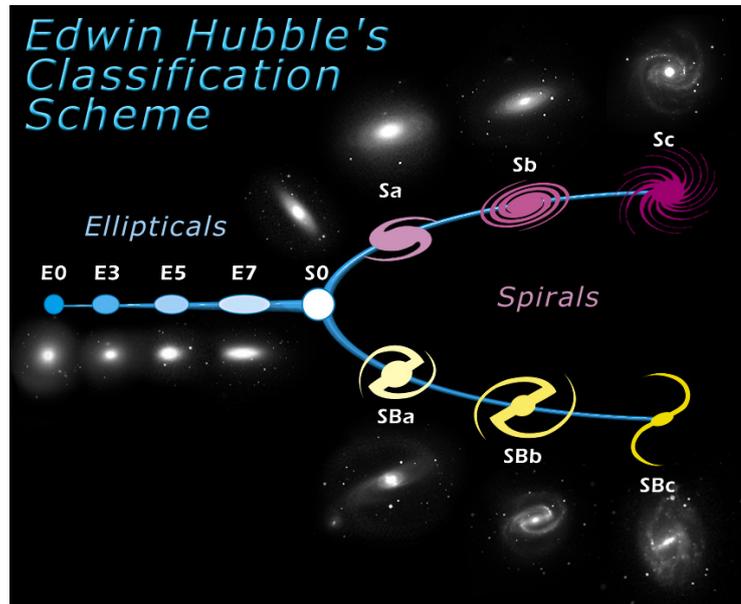
Figure 3.1: Hubble scheme for galaxy classification. See text for details. Image credit NASA.

halo. The mass of dark matter in the Milky Way is estimated to be about $10^{12}\,\mathrm{M_\odot}$ (where $\mathrm{M_\odot}$ denotes the mass of our Sun: $2\times10^{30}\,\mathrm{kg}$). Dark matter is the main responsible for holding gravitationally the Galaxy together. The dark-matter halo is thought to have the form of a flattened sphere, specifically an oblate spheroid. The exact size of the dark-matter halo cannot be quoted, since it has not been observed directly. By looking at its effect on the Magellanic Clouds, its diameter is at least 100–120 kpc.

- *The disk.* Most of the luminous matter is within a thin disk, which also contains the Solar System. Its mass is approximately one-tenth of the mass of the dark-matter halo. It consists of stars and the interstellar medium (ISM). The ISM is mainly composed of gas and dust, magnetic fields are present and cosmic rays propagate through it. Since we are located within the galactic disk, it appears as a band of diffuse light on the sky. It is difficult to define the radius of the disk. The stellar disk has an apparent radius of 15 kpc, but the gas and in particular the atomic hydrogen disk extends to about 25 kpc, although the density decreases considerably beyond 15 kpc. The total height of the galactic disk is about 1 kpc. Our solar system is located near the inner edge of the local Orion-Cygnus arm (Local Arm) at about 8.5 kpc from the Galactic Centre and 15 pc above the midplane.

- *The bulge.* The density of stars rapidly increases close to the centre of the Galaxy and their distribution is more spherical. This region is called the "bulge" and it is thought to have an elongated shape, making the Milky Way a barred spiral galaxy. The bulge extends to about 3 kpc on either side of the Galactic Centre and has a height (and width) of about 2 kpc.
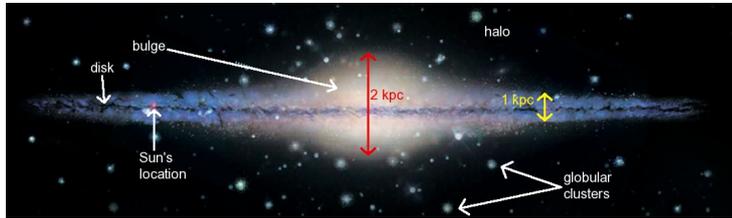
Figure 3.2: Edge-on artistic view of the Milky Way. Figure reproduced after http://woodahl.physics.iupui.edu/Astro105/milkyonedge.jpg.
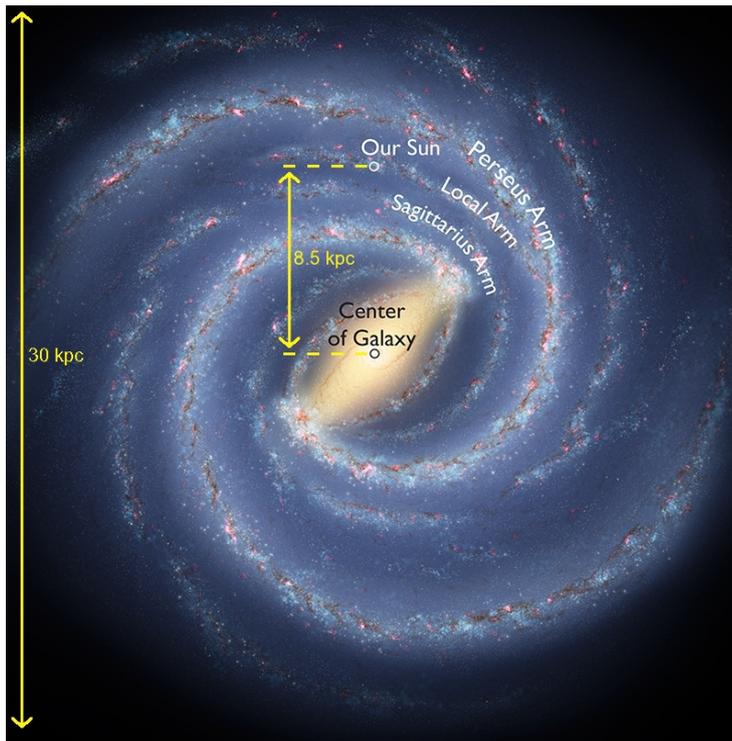
Figure 3.3: Face-on artistic view of the Milky Way. Image credit Robert Hurt, IPAC; Bill Saxton, NRAO/AUI/NSF.

The interstellar medium

The matter in the ISM is made up of gas (in atomic, ionized and molecular forms) and dust. It is concentrated near the Galactic Plane, typically within 150 pc above/below the plane, and in the spiral arms. It has a total mass of about $10^{10}\,M_\odot$. About half of the interstellar mass is confined into clouds which only occupy 1–2% of the interstellar volume. The chemical composition of the interstellar matter is mainly hydrogen (70.4% by mass, 90.8% by number). Helium makes up 28.1% of the mass (9.1% by number) and the remaining 1.5% of the mass consists of heavier elements (referred to as metals by astronomers).

- *Neutral atomic gas.* Here we only speak of hydrogen since it is the most abundant element in the interstellar matter. The main method of detecting neutral atomic hydrogen (denoted by H_I) is via the observation of the 21-cm line. H_I is present in two thermal phases:

    1. A cold phase with temperatures between 50 and $100\,K$, located in dense clouds (also called H_I regions), with a hydrogen density of 20-50 cm^{-3}.

    2. A warm phase with temperatures between 6000 and $10000\,K$, located in the so-called inter-cloud medium, with a hydrogen density of $\sim 0.3\,cm^{-3}$.

    The H_I density in the immediate vicinity of the Sun is lower than the values quoted above. It turns out that our solar system is located inside an H_I cavity, called the Local Bubble. This structure has a width of about 100 pc in the Galactic Plane and is elongated along the vertical. It is filled with ionised hydrogen with a very low density (only $\sim 0.005\,cm^{-3}$), but which has temperatures of nearly $10^6\,K$. The Local Bubble was carved out by a series of past supernovae.

    As noted before, most of the atomic gas is located in the disk and is concentrated near the Galactic Plane. The exponential scale height of the cold phase is about 100 pc. For the warm phase, two vertical scale heights components are seen: one Gaussian with a scale height of about 300 pc, the other exponential with a scale height of about 400 pc. The disk, where the neutral atomic gas is located, is flat and centred around the Galactic Plane only up to distances of about 12 kpc from the Galactic Centre. At larger distances it is tilted, with the gas reaching heights above/below the plane of 1 to 2 kpc.

- *Ionised gas.* Ionised hydrogen (denoted by H_{II}) can be detected using the H_α line, which has a wavelength of 656.28 nm. It is one of the Balmer lines and is created when the electron of a hydrogen atom changes its excitation state from n = 3 to n = 2. H_{II} regions are due to the UV radiation emitted by hot O and B stars (the most massive and hottest stars in the Milky Way). Inside a H_{II} region, ions and free electrons continuously recombine: as a consequence the newly created neutral hydrogen will be ionised once more. The size of the region is determined by the equilibrium of the recombination rate with the photo-ionisation rate. Also ionised hydrogen is present in two thermal phases:

1. A warm phase with temperatures between 6000 and 10000 K, mainly located in the inter-cloud medium (90%), but also partly in H_{II} regions (10%), with a hydrogen density of about $0.04\,\mathrm{cm}^{-3}$.

2. A hot phase with temperatures above $10^6\,\mathrm{K}$ which extends into the galactic halo, with a very low hydrogen density of about $0.003\,\mathrm{cm}^{-3}$.

H_{II} regions are highly concentrated along the Galactic Plane, with a scale height of about $70\,\mathrm{pc}$, while the diffuse component located in the inter-cloud medium has a scale height around $1\,\mathrm{kpc}$. A Gaussian dependence on distance to the Galactic Centre is observed for H_{II} region, with a scale length of $20\,\mathrm{kpc}$ and which peaks around $4\,\mathrm{kpc}$, then decreases again towards the Galactic Centre.

The hot interstellar gas is generated by supernova explosions and stellar winds from the progenitor stars. The hot gas is very buoyant and is located in bubbles (like the Local Bubble described above) and fountains that rain gas back onto the galactic disk. Because of this, it has a large scale height of about $3\,\mathrm{kpc}$, although the uncertainty on this value is quite large.

- *Molecular gas.* Molecular gas is expected where the density is high (as there is a higher chance of atoms meeting each other and binding), the temperature is low (below about $100\,\mathrm{K}$, which avoids collisional disruption) and the UV flux is low (avoiding UV-induced disruption). These conditions are met in cool dense clouds, which are thus called molecular clouds. Molecular clouds themselves are organised in complexes with typical sizes between 20 and $100\,\mathrm{pc}$ and a mean hydrogen number density between 100 and $1000\,\mathrm{cm}^{-3}$. Cloud complexes are mostly located along the spiral arms and are particularly numerous at distances between 4 and $7\,\mathrm{kpc}$ from the Galactic Centre.

  The most abundant interstellar molecule is H_2. It cannot be observed directly, since it has no permanent electric dipole moment and only a very small moment of inertia. Thus, it does not produce significant emission/absorption by rotational or vibrational transition. Most of what is known about molecular interstellar gas comes from the use of the so-called "tracers". The main tracer is the CO molecule (the second most abundant interstellar molecule), which can be observed in its $J = 1 \rightarrow 0$ rotational transition at a radio wavelength of $2.6\,\mathrm{mm}$.

- *Dust.* Dust consists of tiny lumps of solid compounds, mostly made of carbon, oxygen and silicon. The typical size of a dust particle is about 0.1 to $1\,\mu\mathrm{m}$, which makes it comparable in size to the wavelength of visible light. Dust is therefore a very efficient absorber and scatterer of visible light. The total mass of the dust is only about 0.1% of the total mass of the stars, but dust is still very important for a number of processes. It catalyses the formation of molecular hydrogen and also shields H_2 against UV light. It is also thought to be important for the formation of planets, since planetary formation can start with the coagulation of dust grains into planetesimals, which can eventually turn into planets.

Magnetic fields

The observation of the polarisation of starlight from distant stars was the first evidence for the presence of magnetic fields in the ISM. The polarisation is caused by dust grains, the short axis of which aligns with the local magnetic field. Radiation with electric field vector parallel to the long axis of the dust grain is mostly absorbed, leading to polarisation along the direction of the magnetic field. Polarisation measurements only tell us about the direction of the galactic magnetic field. The strength of the magnetic field can be inferred by other means, such as Zeeman splitting of the 21-cm H_I line and Faraday rotation of light from pulsars [85].

The intensity of the magnetic field at our location in the Galaxy is 3–5 μG [86]. The galactic magnetic field consists of two components. A large scale field (also called the "regular" or "uniform" component) which evolves slowly and has a local magnitude of about 1.4 μG and a small scale field (also called the "irregular" or "random" component) representing the fluctuations on the large scale field.

While the measurement of local magnetic fields is relatively easy, since magnetometers can be put aboard spacecraft, magnetic fields further away in the Galaxy are much more difficult to measure. For this reason there is still some tension about the exact topology and intensity of the magnetic field, but a few properties are widely accepted. The regular magnetic field component in the disk has a strong azimuthal component and a smaller radial component, whose magnitude is not known. As viewed from the North Galactic Pole, the direction of the regular field is clockwise while the direction in the Sagittarius Arm is counter-clockwise. This is the only field reversal upon which there is generally agreement. However, it is also possible that there are more magnetic field reversals. Uncertainties are still present concerning the topology of the regular field in the disk, and both axis-symmetric and bi-symmetric spiral configurations are plausible. The strength of the regular field increases smoothly towards the Galactic Centre, reaching about 4.4 μG at a radial distance of 4 kpc [85].

The regular field consists of two separate field layers, the first localised in the disk and the other, which is one order of magnitude weaker, extending into the galactic halo. The transition between the layers takes place at a typical distance of 0.4 kpc above/below the Galactic Plane [87]. The scale height of the halo field is about 1.4 kpc. It is not known if the magnetic field in the halo is symmetric above and below the Galactic Plane (dipole), or anti-symmetric (quadrupole).

The random magnetic field, which is associated with turbulent interstellar plasma, has a local intensity of about 5 μG and is also thought to consist of both a disk and a halo component. The strength of the disk component varies in each spiral arm and decreases as $1/r$ (with r being the radial distance from the Galactic Centre) for radii larger than 5 kpc [85]. The halo component decreases exponentially as a function of the radius and is Gaussian in the vertical direction, with a scale height comparable to the halo component of the regular magnetic field. The random field has a typical coherence length scale of the order of 100 pc.

Even though the magnetic field in the halo is one order of magnitude weaker than that in the disk, it is of great importance for the propagation of cosmic rays, being further extended in height. Since the intensity and scale height of the uniform and random components are of the same order of magnitude,

the transport of cosmic rays in the Galaxy takes place under highly turbulent conditions.

3.1.2   Cosmic rays in the Milky Way

As described in §1.1, cosmic rays are charged particles, consisting primarily of protons. Most of the cosmic rays is produced in galactic sources, even though there is no consensus yet on their origin. The prime candidates for their production and acceleration in the Milky Way are SNRs. Many possible sources are located in the Galactic Plane. After production, the propagation of cosmic rays through the Galaxy and their interactions with the matter and magnetic fields previously described must be taken into account.

Transport of cosmic rays

After acceleration, cosmic ray particles propagate through the interstellar medium under the influence of the interstellar magnetic field. This field confines cosmic rays into the Galaxy, since they are forced to gyrate about the magnetic field lines, following a circular orbit with radius:

$$r_L = \frac{p}{qB} \tag{3.1}$$

where r_L is the Larmor radius, p is the momentum of the particle, q is its charge and B is the intensity of the magnetic field. Considering that the average strength of the magnetic field in the Milky Way is $\sim 3\,\mu$G, the Larmor radius for a proton (Z = 1) with an energy of 10^6 GeV is 0.36 pc, which becomes 360 pc for a proton with an energy of 10^9 GeV. Cosmic rays with energies up to at least about 10^8 GeV are contained in the Galaxy. In the direction parallel to the magnetic field lines, the cosmic ray particles diffuse through the Galaxy due to the random component of the magnetic field. This component is coherent over length scales of about 100 pc, which is small compared to the size of the Milky Way. This explains the isotropy and long confinement time in the Galaxy (which is inferred from unstable isotopes, see below). Besides diffusion, convection can also play a role in the transport of cosmic rays. This effect is inferred from the observation of galactic winds in many galaxies [88].

While propagating through the Galaxy, cosmic rays can interact in several ways. Some of them interact with the interstellar matter and produce secondary particles in inelastic collisions. This process is responsible for the photon and neutrino production. Cosmic ray nuclei can also break up in lighter nuclei like Li, Be and B (referred to as the light elements) in collisions with the interstellar gas. This process is known as spallation. As a result, the abundance of light elements in cosmic rays exceeds the average solar system abundances of these elements. The spallation process is the main way in which these light elements are produced and most of the knowledge about cosmic ray propagation comes from measurements of the abundances. In addition, unstable secondary such as ^{10}Be are produced in spallation process and they can be used to deduce the average cosmic ray lifetime.

Besides losing energy, cosmic rays can also gain energy by scattering off shock fronts or randomly moving magnetic waves. This process is known as diffusive re-acceleration.

In the most general form, the cosmic ray transport can be formulated as [88]:

$$
\frac{\partial \Phi\left(\overrightarrow{r}, p, t\right)}{\partial t} = Q\left(\overrightarrow{r}, p, t\right) + \overrightarrow{\nabla} \cdot \left(D_{xx}\overrightarrow{\nabla}\Phi\right) - \overrightarrow{\nabla} \cdot \left(\overrightarrow{V}\Phi\right) +
$$
$$
\frac{\partial}{\partial p}\left(p^2 D_{pp}\frac{\partial}{\partial p}\frac{\Phi}{p^2}\right) - \frac{\partial}{\partial p}\left[\frac{\partial p}{\partial t}\Phi - \frac{p}{3}\left(\overrightarrow{\nabla} \cdot \overrightarrow{V}\Phi\right)\right] - \frac{\Phi}{\tau_f} - \frac{\Phi}{\tau_d}, \qquad (3.2)
$$

where $\Phi(r, p, t)$ is the cosmic ray density at a certain position position r at a time t for a particle with momentum p, $Q(r, p, t)$ is the source term (representing the cosmic ray sources and including production by spallation and decay), D_{xx} is the spatial diffusion tensor, V is the convection velocity, D_{pp} is the diffusion coefficient in momentum space (representing diffusive re-acceleration), τ_f is the timescale for loss by fragmentation and τ_d is the timescale for radioactive decay.

The cosmic ray transport equation introduced above can be solved by starting with the solution for the heaviest primaries (since they can only be produced at the source, and not via spallation or decay) and using this solution to compute that of lighter primaries in an iterative way. Because of the complexity, this can best be done numerically with, for example, the *GALPROP* code [89].

Several things can happen to cosmic rays. It is generally believed that they eventually disappear, either by diffusing to the edge of the Galaxy where they then have a finite chance to leak out into intergalactic space, or by means of convection. It is also possible however, that they lose all their energy by inelastic collisions with the interstellar matter. And of course, some of the cosmic rays end up in the atmosphere of the Earth, where they interact and can be observed.

3.2 Theoretical models

Having introduced the ingredients for the calculation of the flux of neutrinos coming from CR propagation in the Galaxy, an overview of a few theoretical predictions can be drawn. A large number of modelisations of the galactic neutrino flux have been made, and only a few will be illustrated here. These models either try to solve the problem analytically or numerically. The first approach needs some assumptions in order to simplify the CR transport equations (eq. 3.2) and then compute the resulting neutrino flux; the numerical approach relies on the use of simulation codes such as *GALPROP* [89] or *DRAGON* [90] for the solution of the problem.

3.2.1 Analytical computations

An analytical description of the neutrino flux coming from the interaction of cosmic rays with a dense medium is provided by the authors of [91]. The neutrino intensity $I_\nu(E)$ is given by

$$
I_\nu = \hat{\epsilon}_M d_{CR} n_{gas} \sum_i \int_{A_i E}^{\infty} dE' I_i(E') \sigma_{A_i p}^{inel}(E'/A_i)\frac{dn_{A_i p \to \nu}(E'/A_i, E)}{dE} \qquad (3.3)
$$

where the sum runs over the primary CR mass group i, $I_i(E)$ is the partial intensity for the i-th group, n_{gas} is the gas density, and d_{CR} is the path-length travelled by the CRs. For simplicity a uniform gas density is assumed and the dependence of the confinement time on the charge of the nucleus is neglected.

The helium contribution in the interstellar medium is taken into account by means of an enhancement factor $\hat{\epsilon}_M \simeq 1.3$ for neutrinos in the PeV energy range, to take into account the relative abundance of helium in the medium and its effects on neutrino production. Particle physics enters via the inelastic cross section $\sigma_{Ap}^{\text{inel}}(E_A)$ for an interaction of a nucleus of mass number A and energy per nucleon E_A with a proton, and the neutrino production spectrum $dn_{Ap\to\nu}(E_a,E)/dE$ per inelastic event. The latter is defined as the convolution of the production spectra for different hadron species and the spectra for their decays into neutrinos,

$$\frac{dn_{Ap\to\nu}(E_a,E)}{dE} = \sum_h \int dE_h \frac{dn_{Ap\to h}(E_A,E_h)}{dE_h} \times \frac{dn_{h\to\nu}^{\text{dec}}(E_h,E)}{dE} \tag{3.4}$$

Introducing the energy fraction $z = E/(E'/A_i)$ of the produced neutrinos in eq. 3.3, we can rewrite it in the case of power-law energy spectra of the CRs, $I_i(E) \propto E^{-\alpha}$

$$I_\nu = \hat{\epsilon}_M d_{\text{CR}} n_{\text{gas}} \sum_i I_i(E) Z_A^\nu(E,\alpha_i) \tag{3.5}$$

where the so-called "Z-factors" Z_A^ν [92] for neutrino production are defined as

$$Z_A^\nu = A^{-\alpha} \int_0^1 dz\, z^{\alpha-1} \sigma_{Ap}^{\text{inel}}(E/z) \times \frac{dn_{Ap\to\nu}(E/z,z)}{dz} \tag{3.6}$$

Using eq. 3.4, the neutrino Z-factors can be expressed in terms of the hadron production Z-factors, in the high-energy limit, as

$$Z_A^\nu(E,\alpha) = \sum_h \int_0^1 dz_\nu z_\nu^{\alpha-1} f_{h\to\nu}^{\text{dec}}(z_\nu) Z_A^{\text{hadr}}(E/z_\nu,\alpha) \tag{3.7}$$

where Z_A^{hadr} are defined similarly to Z_A^ν

$$Z_A^{\text{hadr}}(E,\alpha) = A^{-\alpha} \int_0^1 dz\, z^{\alpha-1} \sigma_{Ap}^{\text{inel}}(E/z) \times \frac{dn_{Ap\to h}(E/z,z)}{dz} \tag{3.8}$$

and $f_{h\to\nu}^{\text{dec}}$ are the spectra for hadron decays into neutrinos.

All the dependencies on the properties of proton-proton and nucleus-proton interactions are included in the hadronic Z-factors. They also define how strongly the contribution to neutrino production from primary CR nuclei is suppressed relative to the one of protons. Due to the steep slopes α_i of the primary spectra, these Z-factors are dominated by the hadron spectra in the very forward direction. One can then estimate the suppression of the nuclear contribution, using the relation for the mean number of interacting ("wounded") projectile nucleons $\langle n_{AB}^{Wp}(E)\rangle$ for the collision of nucleus A on nucleus B:

$$\langle n_{AB}^{Wp}(E)\rangle = \frac{A\sigma_{pB}^{\text{inel}}(E)}{\sigma_{AB}^{\text{inel}}(E)} \tag{3.9}$$

neglecting the contribution coming from target diffraction. The forward (z→1) spectra of secondary hadrons become

$$\begin{aligned}
\frac{dn_{Ap\to h}(E,z)}{dz} &\simeq \langle n_{AB}^{Wp}(E)\rangle \frac{dn_{pp\to h}(E,z)}{dz} \\
&= A\frac{A\sigma_{pp}^{\text{inel}}(E)}{\sigma_{Ap}^{\text{inel}}(E)} \frac{dn_{pp\to h}(E,z)}{dz} \tag{3.10}
\end{aligned}$$

Substituting eq. 3.10 in eq. 3.8 the hadron Z-factors become

$$Z_A^{\mathrm{hadr}}(E, \alpha) \simeq A^{1-\alpha} Z_p^{\mathrm{hadr}}(E, \alpha) \qquad (3.11)$$

which leads to

$$I_\nu(E) \simeq \hat{\epsilon}_M d_{\mathrm{CR}} n_{\mathrm{gas}} \sum_i I_i(E) Z_p^\nu(E, \alpha_i) A_i^{1-\alpha} \qquad (3.12)$$

All the Z-factors can be computed using a specific model of hadronic interactions and the resulting neutrino intensity is computed.

This holds where a simple power-law behaviour can describe the CR primary flux dominated by protons. Approaching the knee region a power-law description of the CR flux does not represent well the energy spectrum anymore and, though direct measurement are not available, the CR composition changes to heavier elements. The elemental composition of the total CR flux is not well known and different parametrisations are available [93]. For this energy region, a differential computation can be done assuming a varying slope of the CR spectrum and the relative proportion of heavier elements to proton.

The only missing item is the interaction distance of CRs in the Milky Way. This can be computed modelling the matter distribution in the Galaxy and considering the interaction cross section of the different primary species.

3.2.2   Numerical computations

Though an analytical solution of the CR propagation and interaction equations allows for a direct evaluation of the neutrino flux, its result is strongly dependent on the assumptions that are made and valid only under specific simplifications, as shown in the previous section. More accurate estimations are provided by full numerical computations, where the entire process of propagation and interaction of cosmic rays is simulated, using specific codes which take into account the underlying physics. Moreover they provide the spectra of every particle species at Earth, since all of them are propagated. This allows the tuning of neutrino spectra with experimental data coming from other measurements, such as those from CR and γ-ray observatories.

The authors of [94] have computed the diffuse neutrino flux from the Milky Way exploiting a full simulation of cosmic rays propagating and interacting in the galaxy. Their simulation assumes that the local observation of CRs does not reflect their behaviour in the entire galaxy, and a variable diffusion coefficient could explain different anomalies coming from experimental observations. In particular the large γ-ray flux at a median energy of 15 TeV observed in the Galactic Plane by the MILAGRO experiment [95] does not match the extrapolation of Fermi-LAT data under the usual assumption for CR models in the Galaxy [28]. Moreover conventional models systematically underestimate the low energy γ-ray spectrum measured with the Fermi-LAT instrument. Correction to different modelisation of the γ-ray production in the Galaxy can fix these issues but usually produce further anomalies when compared to data. The following assumptions enter the simulation:

1. the diffusion coefficient for CRs δ has a galactocentric radial dependence $\delta(\mathrm{R}) = \mathrm{AR} + \mathrm{B}$ for $\mathrm{R} < 11\,\mathrm{kpc}$ where $\mathrm{A} = 0.035\,\mathrm{kpc}^{-1}$ and $\mathrm{B} = 0.21$
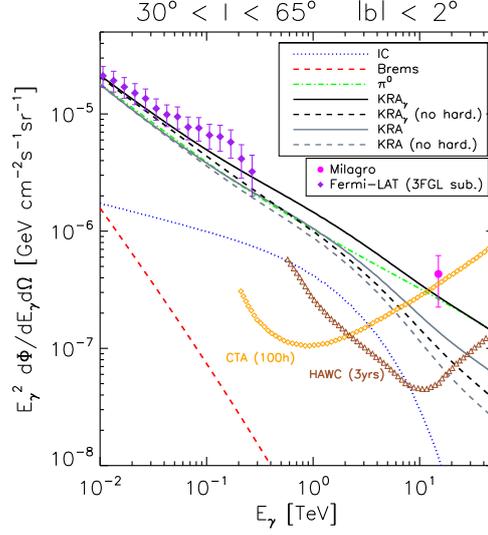
Figure 3.4: Predicted γ-ray fluxes from the model of ref. [94]. The region of the MILAGRO excess is shown, and the different components of the spectrum are reported as explained in the legend. Fermi-LAT and MILAGRO data are shown, together with the expected performance of the CTA and HAWC experiments

so that $\delta(R_{Sun}) = 0.5$, compatible with current models of the interstellar medium. This behaviour may have different physical interpretations, e.g. a smooth transition between a dominant parallel escape along the poloidal component of the regular Galactic magnetic field (in the inner Galaxy, where δ is lower) and a perpendicular escape with respect to the regular field lying in the plane (in the outer Galaxy, where the scaling is steeper);

2. An advective wind for $R < 6.5$ kpc with velocity $V_C(z)\hat{z}$ (where z is the distance from the Galactic Plane) vanishing at $z = 0$ and growing as $dV_c/dz = 100$ km s^{-1} kpc^{-1} is also included. This ingredient is motivated by the X-ray ROSAT observations [96];

3. The vertical dependence of the diffusion coefficient is taken as $D(z) \propto \exp(z/z_t)$;

4. The halo size is $z_t = 4$ kpc for all values of R.

The observed γ-ray spectra at both low and mid galactic latitudes, including the Galactic Centre, are reproduced by this model without spoiling local CR observables: proton, antiproton and helium spectra, B/C and ^{10}Be/^{9}Be ratios. Moreover, this scenario naturally accounts for the radial dependence in the CR spectrum found by the Fermi Collaboration [97]. This model is referred to as "KRA$_\gamma$" since it is tuned on γ-ray data. This setup is implemented with the numerical code *DRAGON* [90], designed to compute the propagation of all CR species. The γ-ray spectrum produced by the model for the region of the MILAGRO anomaly is reported in figure 3.4.

A hardening of the proton and helium spectrum is observed by the PAMELA [98] and AMS-02 [99] experiments. This can be driven by two options: 1) *local*
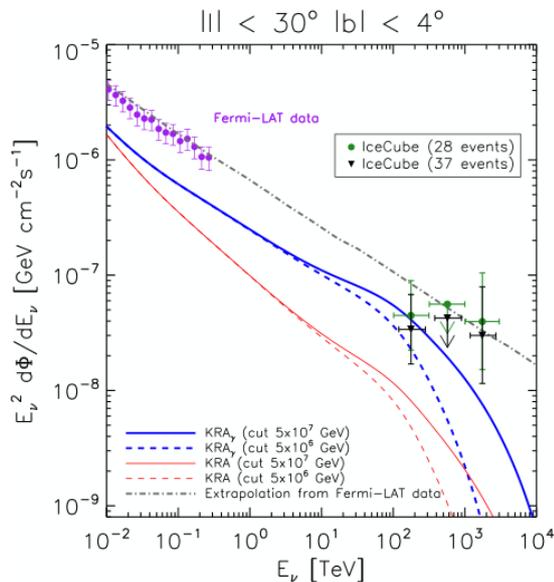
Figure 3.5: Predicted neutrino fluxes from the model of ref. [94]. The plot refers to the inner part of the Galactic Plane, for which the red lines report the neutrino expectations from the model of [94] without the assumption of a variable CR diffusion coefficient (KRA model) while the blue lines assume a radial dependence as described in the text (KRA$_\gamma$ model). Solid and dashed lines refer to different CR cut-off energies. The models are compared to the γ-ray measurement from Fermi-LAT (purple symbols) and its extrapolation (dot-dashed line) to the IceCube measurement reported as green and black dots for the 2 years [67] and 3 years [68] samples respectively as reported in ref. [100]

hardening originating from nearby CR accelerators; 2) *global hardening* from a spectral feature in the rigidity dependence of CR source spectra or the diffusion coefficient. In both cases it is assumed that CR spectra extend up to a certain E_{cut}/nucleon energy cut-off. Different cut-off energies are measured in CR experiments: a 5 PeV or a 50 PeV cut-off have been simulated. The resulting neutrino spectra are shown in figure 3.5.

3.3 Neutrino flux from γ observations

An independent estimate for the neutrino flux can be obtained using the γ-ray flux measured by the Fermi satellite and converting it into a neutrino flux. Part of the diffuse γ-ray flux observed in the central part of the Milky Way is of hadronic origin, i.e. comes from π^0 decays. The main assumption to be made for estimating the neutrino flux from γ-ray observations is the fraction of the γ-ray flux coming from π^0 decays.

Such a procedure has been applied in ref. [101], in which γ-ray data measured by the Cherenkov telescope MILAGRO in combination with the X-ray satellite EGRET data are used. The procedure applied in that paper uses some simplifying assumptions. It is assumed that all photons are of hadronic origin and the flux

in the inner Galaxy ($|\ell| \leq 40°$ and $|b| \leq 2°$) is obtained by scaling the MILAGRO results (which only measures the part of the inner Galaxy between a longitude of 30° and 40°) with the help of the EGRET results.

In ref. [41] instead, data collected by the Fermi Collaboration are used, covering the full sky with higher statistics and a good angular resolution. Although Fermi data do not extend to energies of 10 TeV like the MILAGRO data, the high-energy threshold is large enough (of the order of 600 GeV) to give a reliable estimate of the expected neutrino fluxes.

The LAT instrument aboard the Fermi satellite detects photons from about 20 MeV to over 300 GeV by recording the electron-positron pairs created by individual γ-rays [102]. The Fermi collaboration provides these data, for which they have subtracted the fluxes of all known point sources, in term of measured flux binned in energy pixelled in their galactic coordinates. A simple single power law describes well the data above 3.4 GeV in each of the pixels. In general a single power law cannot be used for the whole region of interest.

Several mechanisms can produce gamma rays:

1. Synchrotron radiation, which occurs when a charged particle is deflected in a magnetic field;

2. Bremsstrahlung, in the case the charged particle is deflected in the Coulomb field of a nucleus;

3. Inverse Compton (IC) scattering, in which a low energy photon (for instance from the cosmic microwave background) is blue-shifted by the collision with an energetic electron;

4. Matter-antimatter annihilation, mostly electron-positron and proton-antiproton annihilations;

5. Decay of subatomic particles, like the π^0 or the η^0 mesons.

Concerning the latter option, almost every subatomic particle has one or more decay modes involving photons, but for the current discussion only the neutral pion and η particle are important, since they are the lightest neutral unflavoured mesons. Both are commonly produced in proton-proton interactions and contribute to the number of observed γ-rays. Since about a factor of 10 more π particles than η particles are produced and the η^0 only decays to photons in about 44% of the cases (with respect to the 98.8% branching ratio of neutral pions), the contribution from pions is dominant.

Among the mechanisms described above, IC scattering and π^0 decay are the most important at photon energies larger than 10 GeV. The relative importance of these two processes depends on the density of electrons and photons compared to the density of CRs and interstellar matter. In the Galactic Plane, where the density of protons is maximal, the main contribution will thus come from π^0, while at high latitudes the IC scattering contribution is higher. The contributions of these two processes have been determined by the Fermi Collaboration for several regions in galactic coordinates.

Several different models are used by the Fermi Collaboration to fit the diffuse γ flux, which differ in the CR source distribution, the size of the volume in which the CRs can propagate and the distribution of interstellar matter. The models are constrained to reproduce the locally observed CR fluxes and the predicted

flux is compared to data using a maximum-likelihood fit. In this fit, the fluxes and spectra of an isotropic γ-ray background component and of known point sources, the strength of the infrared and optical radiation field and a parameter related to the matter composition can be varied. The percentage of all photons originating from neutral pion decays is around 70% at 10 GeV arriving at 45% when extrapolating to 1 PeV for the inner part of the Galactic Plane.

Using a Monte Carlo code like Pythia [103] the neutral pion flux can be determined from the observed γ spectrum since the gamma ray flux Φ_γ can be described as

$$\Phi_\gamma(E_\gamma) = dE_{\pi^0} Y_\gamma(E_{\pi^0}, E_\gamma) \Phi_{\pi^0}(E_{\pi^0}) \tag{3.13}$$

where Φ_{π^0} is the π^0 flux and Y_γ is the yield of γ-rays from neutral pions. This factor Y_γ can be indeed computed using Monte Carlo simulations and the relation of equation 3.13 can be inverted. In order to obtain the expected neutrino fluxes from γ observations, the charged pions flux must be computed. This is obtained from that of neutral pions, since the production ratio between $\pi^\pm$ and π^0 in high energy proton-proton interactions is known from particle physics. Indeed the sum of charged pions is equal to the number of neutral π mesons. Since charged pions are the main neutrino sources, the neutrino flux can be extracted analogously to what is done in equation 3.13, where instead of γ-rays neutrinos are considered.

Chapter 4

The ANTARES telescope

ANTARES (Astronomy with a Neutrino Telescope and Abyss environmental RESearch) is at present the largest neutrino telescope in the Northern hemisphere and the largest under-water neutrino detector [52]. Being in the Mediterranean Sea, the detector has a good visibility of the Southern sky exploiting the reconstructed tracks of upward-going neutrino-induced muons. This is the most interesting region for cosmic neutrino searches due to the presence of the Galactic Centre and Galactic Plane, where many neutrino emitting candidates are expected (§1.1.2).

The ANTARES project has been set up in 1996 [104]. The first detection line was connected in March 2006 [105] and the detector was completed in May 2008. It has been taking data continuously since then, becoming also the longest operating under-water neutrino telescope. It is located at a depth of 2475 m in the Mediterranean Sea at (42° 48′ N, 6° 10′ E), 40 km from La Seyne-sur-Mer in the Gulf of Lion, Southern France (figure 4.1).

4.1 Detector layout

The ANTARES detector consists of 12 detection lines with 25 storeys each. A standard storey includes three optical modules (OMs) [106], glass spheres housing 10-inch photomultiplier tubes (PMTs) [107] and a local control module (LCM) containing the off-shore electronics [108, 109]. The distance between storeys on each line is 14.5 m, and the first storey is located ~ 100 m from the sea-bed. OMs in the storey, mounted on the Optical Module Frame (OMF), are orientated 45° downwards in order to optimise their acceptance to the light from upward-going tracks and to reduce the effect of sedimentation and biofouling. The length of a line is 450 m and the horizontal distance between neighbouring lines is 60-75 m. The total number of active OMs is 885.

All the lines are connected to a Junction Box (JB) on the sea-bed, which is then connected to the shore station in La Seyne-sur-Mer with a 42 km-long electro-optical cable (the Main Electro-Optical Cable, MEOC). Through this cable the detector is powered, the data are collected and a clock signal, responsible for the synchronisation of the different detector elements, is distributed. A schematic view of the detector is reported in figure 4.2. At the shore station filtering and triggering of data take place. Filtered data are stored at a computer centre in
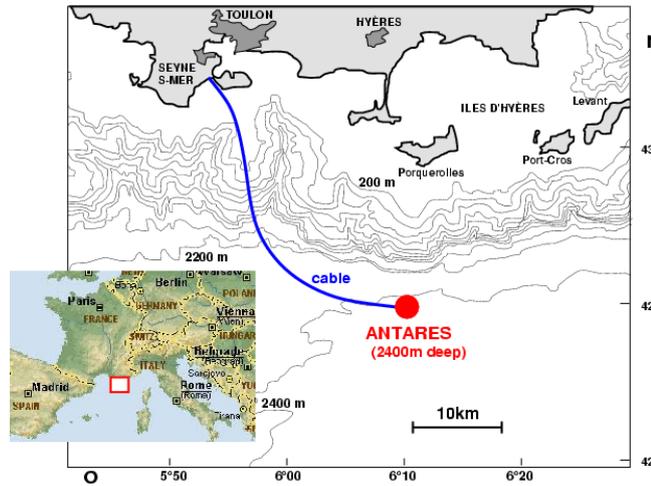
Figure 4.1: ANTARES location in the Mediterranean Sea, 40 km off-shore Toulon, France. Also shown the path of the 42-km-long electro-optical cable connecting the detector to the shore station in La Seyne-sur-Mer.

Lyon.

Instruments for marine and Earth science researches are distributed on the 12 lines and are also located on an additional instrumentation line devoted to the monitoring of the sea environment. Being operated continuously since 8 years, ANTARES provides the longest continuous set of environmental data at such a depth in the Mediterranean Sea.

Each line is anchored to the sea-bed and pulled taught by the buoyancy of the individual OMs and a top buoy. Due to the flexible nature of these lines, a relatively small water current velocity of 5 cm/s can result in the top storeys being displaced by several meters from the vertical: consequently, real time positioning of each OM is needed. This is achieved through two independent systems: an acoustic positioning system and tiltmeters-compasses on each storey. The shape of each line is reconstructed by performing a global fit using information from both of these systems. The relative positions of each individual OM is then calculated from this line fit using the known geometry of each storey.

High timing resolution on the recorded PMT signals, of the order of 1 ns, is necessary to achive the required angular resolution of the telescope. An essential element for this aim is the master clock system, based on-shore, which delivers a common reference time to all the off-shore electronics in the LCMs. This system delivers a "timestamp", which is derived from GPS time, via an optical fibre network from the shore station to the junction box and then to each line base and to each LCM. This system, which works at 20 MHz clock, is self calibrating and continuously measures the time path from shore to the LCM by echoing signals received in the LCM back to the shore station.

Figure 4.2: Schematic view of the detector layout.

4.2 Site characteristics

During the R&D phase of the experiment, an extensive program has been carried out in order to measure some environmental parameters and the optical water properties at the detector site. This section reviews the most relevant results.

4.2.1 Water properties

Water properties in the ANTARES site have been studied analysing time-of-flight distributions of photons emitted from a pulsed isotropic light source and detected by a PMT at different distances from the source and for two wavelengths [110]. While this approach is not sufficient to fully determine the differential cross section of the photon scattering process, the absorption length can be measured. A parametrisation which reproduces the main features of the scattering process can be obtained, sufficient for the needs of data analysis in the telescope.

The system for this measurement was mounted on an autonomous mooring line anchored by a sinker. The line remained vertical because of the flotation provided by syntactic buoys. The measuring system consisted of 17-inch pressure resistant glass spheres mounted on two triangular aluminium frames. A set of three mechanical cables attached to the vertices of the two frames defined their separation distance. The bottom frame supported a light source sphere which contained a set of LEDs with their pulsers. The top frame supported a detector sphere facing the light source sphere and a service sphere. The detector sphere housed a 1-inch photomultiplier tube and the front-end electronics. Such a small PMT is ideal for this measurement since its acquisition is only slightly influenced by the optical background in water and the transit time spread is extremely limited, providing a proper measurement of the pulse time. Except for the PMT window, the internal surface of the detector sphere was blackened in order to absorb photons outside the PMT detection solid angle. The service
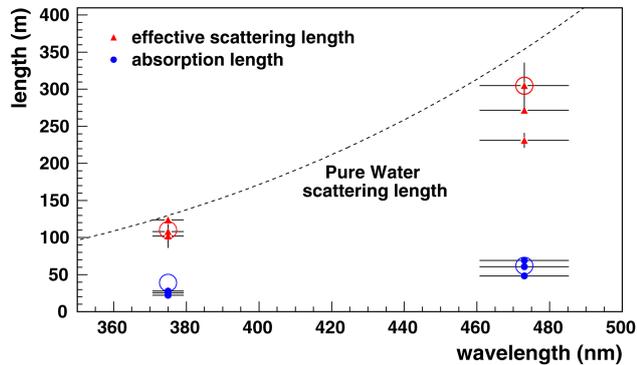
Figure 4.3: Water properties at the ANTARES site [110]. The red and blue symbols represent the measured effective scattering and absorption length of light in water respectively at two different wavelength over different periods of time. The black dashed line shows, for comparison, the effective scatterning length of light in pure water.

sphere contained the data acquisition system for the experimental setup.

In order to obtain an isotropic light source for two wavelengths, 6 pairs of LEDs were mounted on the centres of the faces of a cubic frame 3 cm on a side which also supported the LED pulser boards. The cube was installed at the centre of a 17-inch glass sphere whose external surface had been sand blasted to provide extra diffusion and to remove surface ripples or roughness which can destroy the homogeneity of the emitted light flux. The measured values for the effective attenuation length and the absorption length at the ANTARES site are reported in figure 4.3. The measured value of the effective attenuation length for a wavelength $\lambda = 466$ nm is

$$L_c\left(\lambda = 466\,\mathrm{nm}\right) = 41 \pm 1(\mathrm{stat}) \pm 1(\mathrm{syst})\,\mathrm{m}. \qquad (4.1)$$

The measurement had been repeated during the course of one year to understand the time variability of water properties at the experimental site. Small differences were found at different times, compatible with the accuracy of the measurement.

4.2.2 Biofouling and sedimentation

The detector elements are exposed to particle sedimentation and adherence of bacteria (biofouling) which reduce the light transmission through the glass sphere of the OMs. These effects on the ANTARES optical modules have been studied in ref. [111]. The experimental setup consisted of two resistant glass spheres similar to those used for the OMs. One of them was equipped with five photo-detectors glued to the inner surface of the sphere at different inclinations (zenith angles θ) which were illuminated by two blue light LEDs contained in the second sphere. The measurements went on during immersions of several months and the results were extrapolated to longer periods of time. Figure 4.4 shows the light transmission as a function of immersion time for the the five photo-diodes. As expected there is a tendency in the fouling to decrease when the zenith angle on the glass sphere increases. The loss of transparency in the equatorial region
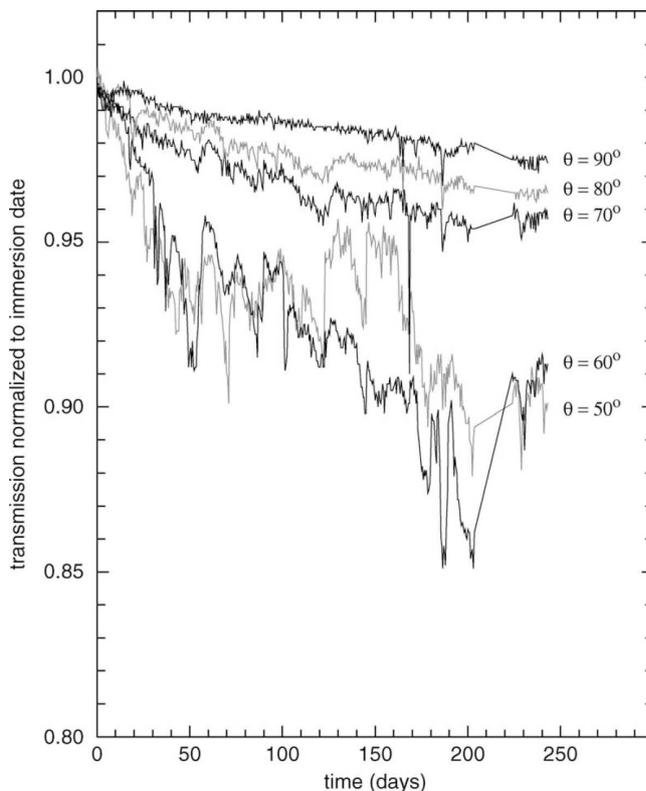
Figure 4.4: PMT light transmission as a function of time spent under-water and of the inclination with respect to the horizontal [111].

of the OM dropped only of about 2.7% in eight months of operation of the test system and then seems to saturate. Extrapolations indicate a global loss after 1 year of about 2% (taking into account the two glass spheres used in the setup). Considering that the PMTs of ANTARES point 45° downward (zenith angle of 135°), the biofouling and the sedimentation should not represent a major problem for the experiment.

4.2.3 Optical background

The optical background on PMTs in sea water has two main natural contributions: the decays of radioactive elements naturally present water and the light produced by living creatures, the so-called *bioluminescence*. ^{40}K decay is by far the dominant process among radioactive decays in sea water. Its decay cannels are:

$$^{40}K \rightarrow ^{40}Ca + e^- + \bar{\nu}_e$$
$$^{40}K + e^- \rightarrow ^{40}Ar + \nu_e + \gamma \tag{4.2}$$
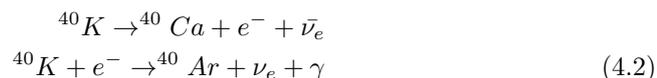
Electrons produced in the first of these processes are often above the threshold for Cherenkov light production. The γ-ray from the second reaction has an energy of 1.46 MeV and can therefore induce electrons above the Cherenkov
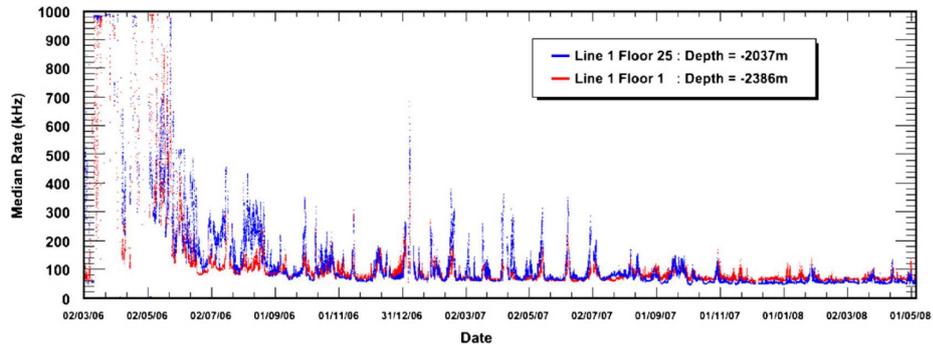
Figure 4.5: Evolution of median measured rates on two ANTARES OM as a function of time over two years of data taking [112]. The red (blue) points shows measured data an optical module at the bottom (top) of the detector.

threshold via Compton scattering. The intensity of ^{40}K optical background is related to its concentration and thus to salinity of sea water. Water salinity is almost constant all over the Mediterranean Sea. The mean single rates from ^{40}K decays is of about 50 kHz on a 10-inch PMT [112].

Two sources of bioluminescence are present in deep sea: glowing bacteria and flashes of light produced by marine animals. The optical background given by these effects can be several orders of magnitude more intense than ^{40}K light. The passage of light emitting organisms can indeed induce bursts in the counting rates of PMTs, while the optical noise due to radioactive decays of salts in water produce a more or less constant baseline. Seasonal effects are present in bioluminescence, which reaches its maximal intensity during spring – MHz single rates on PMTs can be detected during these period and the detector is switched-off to avoid data acquisition problems and excessive ageing of PMTs.

4.3 Data acquisition

The Data acquisition (DAQ) system of ANTARES is extensively described in ref. [109]. The full-custom *Analogue Ring Sampler* (ARS) has been developed to perform the complex front-end operations [113]. This chip samples the PMT signal continuously at a tunable frequency up to 1 GHz and holds the analogue information on 128 switched capacitors when a threshold level is crossed. The information is then digitised, in response to a trigger signal, by means of two integrated dual 8-bit Analog-to-Digital Converter (ADC). Optionally the dynamic range may be increased by sampling the signal from the last dynode. A 20 MHz reference clock is used for time stamping the signals. A Time-to-Voltage Converter (TVC) device is used for high-resolution time measurements between clock pulses. The ARS chip can also discriminate between simple pulses due to conversion of single photoelectrons (SPE) from more complex waveforms. The two classes can indeed be identified on the basis of the amplitude of the signal, the time above threshold and the occurrence of multiple peaks within a time gate. Only the charge and time information is recorded for SPE events, while a full waveform analysis is performed in all other cases. The ARS chips are arranged on a motherboard to serve the optical modules. Two ARS chips, in

a "token ring" configuration, perform the digitisation of the charge and time information of a single PMT. A third chip on each board is used for triggering purposes. The settings of each individual chip can be remotely configured from the shore.

The counting rates on each OM exhibit a baseline dominated by optical background due to sea water ^{40}K decay and bioluminescence coming from bacteria, as well as bursts of a few seconds duration probably produced by bioluminescent emission of macro-organisms close to the OM itself. The average counting rate increases from the bottom to shallower layers. The baseline is normally between 50 to 80 kHz. Differently from the ^{40}K background, bioluminescence suffers from seasonal and annual variations. A high rate veto, often set to 250 kHz single rate on each PMT, serves as an online safeguard against bioluminescence bursts.

The OMs deliver their data in real time and can be remotely controlled through a Gb Ethernet network. Every storey is equipped with a Local Control Module (LCM) hosting the electronic boards for the OM signal processing, the instrument readout, the acoustic positioning, the power system and the data transmission. Every five storeys the Master Local Control Module also contains an Ethernet switch board for the multiplexing of the DAQ channels from the other storeys. At the bottom of each line, the Bottom String Socket is equipped with a String Control Module which contains local readout and DAQ electronics, as well as the power system for the whole line. Both the Master Local Control Modules and the String Control Modules include a Dense Wavelength Division Multiplexing (DWDM) system. The DWDM is used in data transmission to merge several 1Gb/s Ethernet channels on the same pair of optical fibres, using different laser wavelengths. The lines are linked to the junction box by electro-optical cables which were connected using an unmanned submarine vehicle. A standard deep-sea telecommunication cable links the junction box with a shore station where the data are filtered and recorded.

All OMs are continuously read out and digitised information (hits) is sent to shore. A hit is a digitised PMT signal above the ARS threshold, set at about 1/3 of the single photoelectron level (Level 0 hits, L0). On-shore, a dedicated computer farm performs a global selection of hits looking for interesting physics events (DataFilter). This on-shore handling of all raw data is the main challenge of the ANTARES DAQ system, because of the high background rates. The data output rate can be between 0.3 GB/s to 1 GB/s, depending on the background level and on the number of active strings. Subsets of L0 hits, requiring particular conditions, are used for triggering purpose. This subset – Level 1 hits, or simply L1 – corresponds either to coincidences of L0 on the same OM triplet of a storey within 20 ns or to a single high amplitude L0 (typically >3 p.e.). The DataFilter processes all data online and looks for physics events by searching for a set of correlated L1 hits on the full detector in a $\sim 4\,\mu$s window. In case an event is found, all L0 hits of the full detector during the time window are written on disk, otherwise hits are thrown away. The trigger rate is between 1 to 10 Hz, depending on the number of strings in data acquisition, on the environmental conditions and on the active trigger algorithms. Most of the triggered events are due to atmospheric muons, successively reconstructed by track-finding algorithms. If ANTARES receives external alerts, such as from GRB observatories [109], all the activity of the detector is recorded for a few minutes. Untriggered data runs are also collected: this subset is used to monitor the relative PMT efficiencies, as well as to check the timing within a storey, using the ^{40}K activity.

4.4 Event reconstruction

All-flavour neutrinos can be detected in ANTARES. As the present work will be addressed to muon neutrino undergoing charged current interactions, the reconstruction of this event topology will be described in this section. Neutrino induced events must be reconstructed both in direction, for the pointing accuracy of the telescope, and in energy, for background suppression.

4.4.1 Track reconstruction

The challenge of measuring muon neutrinos consists in fitting the trajectory of the muon to the arrival times and to the amplitudes of the signal detected by the OMs. For a given muon position and direction at an arbitrary time t_0, the expected arrival time t^{exp} of the Cherenkov photons follows from the geometric orientation of the OM with respect to the muon path and the straight light propagation. The difference between t^{exp} and the measured arrival time of the photon (i.e. the hit time) defines the time residual

$$r = t^{\mathrm{meas}} - t^{\mathrm{exp}}. \tag{4.3}$$

Photons that scatter in the water and photons emitted by secondary particles (e.g. electromagnetic showers created along the muon trajectory) will arrive at the OM later than t^{exp}, leading to positive residuals.

The track reconstruction method is based on a likelihood fit that uses a detailed parametrisation, derived from simulation, for the Probability Density Function (PDF) of the residuals of the hits, under the assumption of Cherenkov emission from the track, $P(r)$. Also late hits due to light emission by secondary particles or light scattering are considered [114]. Moreover, the probability of a hit being due to optical background is accounted for as a function of the hit amplitude and the orientation of the OM with respect to the muon track.

It has been found that the likelihood function has many local maxima and that the likelihood fit is successful only if the maximisation procedure is started with track parameters that are already a good approximation to the optimal solution. To obtain this approximate solution, the full likelihood fit is preceded by a series of "prefit" algorithms of increasing sophistication. An important ingredient in the prefit stage is the use of a so-called "M-estimator", which is a variant of a χ^2 fit not taking into account full information on the time residual. This is crucial, as it allows the fit to converge to a solution relatively close (typically a few degrees) to the true muon parameters, while being robust against the presence of background hits at large residuals.

The M-estimate is followed by two different versions of the likelihood fit, the last one fully accounting for the presence of background hits. The procedure begins at nine different starting points to increase the probability of finding the global minimum. To mitigate the associated loss in speed, analytical expressions for the gradient of the likelihood function are used in the minimisation/maximisation processes. The value of the final log-likelihood per degree of freedom, obtained from the final fit, is used as a measure of the goodness of the fit. This is combined with information on the number of times the repeated procedure converges to the same result N_{comp} to provide a value

$$\Lambda = \log(L)/N_{\mathrm{dof}} - 0.1(N_{\mathrm{comp}} - 1). \tag{4.4}$$
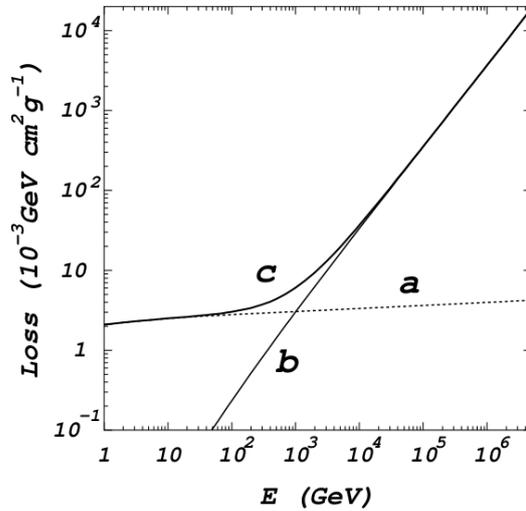
Figure 4.6: Parametrisation of the energy loss of relativistic muons in water; the term a represent the ionisation energy loss, b is for the radiative losses due to bremsstrahlung and pair production [115].

The variable Λ is useful for the rejection of badly reconstructed events, in particular atmospheric muons that are reconstructed as upward-going.

4.4.2 Energy reconstruction

The measurement of the neutrino energy is a non trivial problem. Detected events are prevalently passing-through muons, generated outside the detector and traversing it. Only a fraction of the neutrino energy is transferred to the detected muon, which is often produced outside the instrumented volume of the detector. In addition, as the muon travels, it loses energy before being detected. Since the muon energy loss is proportional to the muon energy, measuring the intensity of energy loss processes can give an estimate of the muon energy itself.

Energy loss processes

Muon energy losses are usually classified into continuous and discrete processes. The former is due to excitation/ionisation, which depends weakly on muon energy and can be considered nearly constant for relativistic particles. For muons below $\sim 500\,\mathrm{GeV}$, this is the dominant energy loss process. At higher energies, discrete energy losses become important: bremsstrahlung, direct electron-positron pair production and electromagnetic interaction with nuclei. The α and β coefficients in equation 1.22 are mildly energy dependent as well as dependent upon the chemical composition of the medium: in particular $\alpha \propto Z/A$ and $\beta \propto Z^2/A$. Typical values of the $\alpha(E_\mu)$, $\beta(E_\mu)$ coefficients in water are given in ref. [115]. Figure 4.6 shows the general behaviour of muon energy loss in water, while figure 4.7 reproduces the behaviour of the various components of radiative/discrete processes.
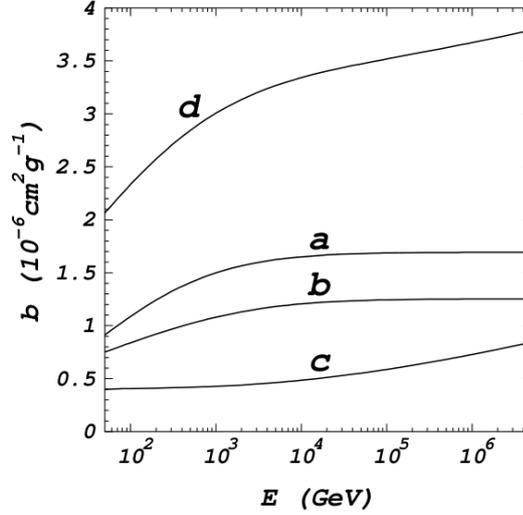
Figure 4.7: Radiative energy losses of muons in water (term $\beta(E)$ in equation 1.22) [115]. Curve (a) represents the pair production energy loss, curve (b) the energy loss by brehmsstrahlung and curve (c) the contribution coming from photo-nuclear reactions. Curve (d) shows the sum of the three components.

Ionisation

Ionisation is the dominating energy loss process for muons in the hundred GeV range. When the muon velocity is larger than the average velocity of electrons in atomic orbitals ($\sim Z\alpha c$), the average energy loss is given by the Bethe-Bloch expression:

$$-\frac{dE}{dx} = K\frac{Z}{A\beta^2}\left[\frac{1}{2}\ln\left(\frac{2m_e c^2\beta^2\gamma^2 T_{\max}}{I^2} - \beta^2 - \frac{\delta(\beta\gamma)}{2}\right)\right] \qquad (4.5)$$

where Z and A are the atomic and mass number of the traversed material. $T_{\max}$ is the maximal kinetic energy that can be transferred to a free electron in a single collision:

$$T_{\max} = \frac{2m_e\beta^2\gamma^2}{1 + 2\gamma\frac{m_e}{m_\mu} + \left(\frac{m_e}{m_\mu}\right)^2} \qquad (4.6)$$

while the term δ represents the corrections due to matter effects. The term I is the average ionisation potential of the material and depends on its Z [116]. In the low energy regime, below a few GeV, energy loss is proportional to β^{-2}, until it reaches a minimum value – the muon is a Minimum Ionising Particle (MIP). Above this energy, the energy loss grows logarithmically and can be considered, at a first approximation, equal to $2\,\mathrm{MeV\,cm^2/g}$.

Radiative effects

- The dominating process for muon energy loss at high energies is given by e^+e^- pair production. The differential cross section for this process can

56

be approximated to:

$$\frac{d\sigma(E,\nu,\rho)}{d\nu d\rho} = \frac{2}{3\pi}(Z\alpha r_e)^2\frac{1-\nu}{\nu}\left(\Phi_e + \frac{m_e^2}{m_\mu^2}\Phi_\mu\right) \tag{4.7}$$

where $\nu = (\epsilon_+ + \epsilon_-)/E$ is the fractional energy given to the pair and $\rho = (\epsilon_+ - \epsilon_-)/E$ is the asymmetry coefficient in the energy transfer. Φ_e e Φ_μ represent the contribution from further QED diagrams describing atomic and nuclear structure corrections.

- *Bremsstrahlung* is the process for which a charged particle emits braking radiation in the presence of a strong nuclear electromagnetic field. The general expression for the cross section of this process can be written as:

$$\sigma = \sigma_{el} + \Delta\sigma_a^{\text{inel}} + \Delta\sigma_n^{\text{inel}} \tag{4.8}$$

where σ_{el} is the elastic cross section of the central Coulomb field, with the inelastic corrections $\Delta\sigma_a$ and $\Delta\sigma_n$, to take into account that the atomic and nuclear charge distribution modify the electric field and the interactions producing changes in the electronic and nuclear structure of the final state:

$$\sigma_{el}(E,\nu) = \frac{\alpha}{\nu}\left(2Z\frac{m_e}{m_\mu}r_e\right)^2\left(\frac{4}{3} - \frac{4}{3}\nu + \nu^2\right)\Phi(\delta) \tag{4.9}$$

$$\Phi(\delta) = \ln\left(\frac{\frac{189m_\mu}{m_e}Z^{-1/3}}{1 + \frac{189\sqrt{e}}{m_e}\delta Z^{-1/3}}\right) - \Delta\sigma_n^{el}(\delta) \tag{4.10}$$

here ν is the fraction of energy which is transferred to the outgoing photon and $\delta \simeq \frac{m_\mu^2\nu}{2E(1-\nu)}$ is the minimum energy transfer. Φ represents the *screening* given by the traversed material. The contribution coming from inelastic terms is small but not negligible, especially for larger ν. The nuclear contribution is about one order of magnitude larger than the atomic one.

- A muon can also directly interact with a nucleus, via photon exchange. This deep inelastic interaction produces an hadronic shower, from nuclear fragmentation. The cross section is given by:

$$\frac{d\sigma_{pn}(E)}{d\nu} = \frac{A\alpha}{2\pi}\sigma_{\gamma N}(\nu E)\nu \times F[E,\nu,\sigma(\nu E)] \tag{4.11}$$

where ν is the fraction of energy transferred by the muon and $\sigma_{\gamma N}$ is the interaction cross section of the real photon with the nucleon. F describes fragmentation processes and hadronic shower production.

Muon energy estimation

Cherenkov light is emitted not only by muons travelling in water, but also by charged particles from hadronic and electromagnetic showers caused by radiative energy loss processes. This additional light related to radiative processes above the critical energy can be seen in different observables such as for example the

charge of individual PMT hits. The amount of detected light can be used to infer the energy of the muon and finally this information can used to determine the energy of the parent neutrino. An overview on the energy reconstruction methods used in ANTARES is give in ref. [117].

"Machine learning methods" are established methodologies to derive the connection between a set of observables and a physical quantity in a semi-parametric way. An *Artificial Neural Network* (ANN) can be used to determine the functional dependency between a set of observables $\hat{x}$ related to the observed light in the telescope and the estimated energy $\hat{E}$. Using multiple layers of nodes, all input variables are correlated using weights w_i and a correlation function g such that the output of each layer y is defined as

$$y = g\left(\sum_i w_i \hat{x}_i\right). \tag{4.12}$$

The ANN is trained on simulated data $(\hat{x}_{\mathrm{MC}}, E_{\mathrm{MC}})$ for the reconstruction of the energy of the event. During the training an error function $\epsilon(\hat{E}(\hat{w}_{\mathrm{MC}}, \hat{x}), E_{\mathrm{MC}})$ is minimised so that the measurement gets closer to the expectations from simulations.

A second method, denoted in the following as *energy likelihood method* [118], maximises the agreement between the expected amount of light in the optical modules and the amount of light that is actually observed. Starting from the direction information of the track reconstruction procedure and keeping the energy of the muon E_μ as a free parameter, a maximum likelihood function is constructed as

$$\mathcal{L}(E_\mu) = \frac{1}{N_{\mathrm{OM}}} \prod_i^{N_{\mathrm{OM}}} \mathcal{L}_i(E_\mu) . \tag{4.13}$$

This product is taken over all the N_{OM} optical modules positioned up to $300\,\mathrm{m}$ from the reconstructed track, regardless of whether a hit is recorded or not. Optical modules with unusually high or low counting rates in a particular run, as well as those that are not active, are excluded. $\mathcal{L}_i(E_\mu)$ depends on the probability of observing a pulse of measured amplitude Q_i given a certain number of photo-electrons produced on the ith OM. These individual likelihood functions $\mathcal{L}_i(E_\mu)$ are constructed as

$$\mathcal{L}_i(E_\mu) \equiv P(Q_i; \langle n_{pe}\rangle) = \sum_{n_{pe}=1}^{n_{pe}^{\max}} P(n_{pe}; \langle n_{pe}\rangle) \cdot G(Q_i; n_{pe}) , \tag{4.14a}$$

when a hit is recorded and

$$\mathcal{L}_i(E_\mu) \equiv P(0; \langle n_{pe}\rangle) = e^{-\langle n_{pe}\rangle} + P_{th}(\langle n_{pe}\rangle) , \tag{4.14b}$$

when there is no hit on the optical module. Equation 4.14a consists of two terms, the Poisson probability $P(n_{pe}; \langle n_{pe}\rangle)$ of having n_{pe} photo-electrons given an expectation of $\langle n_{pe}\rangle$, and a Gaussian term $G(Q_i; n_{pe})$ which expresses the probability that n_{pe} photo-electrons on the photo-cathode will yield the measured amplitude Q_i. Equation 4.14b consists of a term describing the Poisson probability of observing zero photo-electrons when the expected value is $\langle n_{pe}\rangle$, and a term, $P_{th}(\langle n_{pe}\rangle)$, describing the probability that a photon conversion

in the optical module will give an amplitude below the threshold level of 0.3 photo-electrons.

A phenomenological muon energy estimation method – denoted in the following as *energy loss method* [119] – relies on the muon energy losses along its trajectory, as described previously. The muon energy deposit per unit path length is approximated by an estimator ρ which can be derived from measurable quantities

$$\frac{dE}{dX} \propto \rho = \frac{\sum_{i=1}^{N_{\mathrm{hit}}} Q_i}{\epsilon} \cdot \frac{1}{L_\mu}. \tag{4.15}$$

The quantity L_μ represents the length of the reconstructed muon path starting at the entry point on the surface of a cylinder surrounding the instrumented volume of the detector. Due to the light transmission properties of the water, this volume is defined extending the radius and height of the cylinder by twice the light attenuation length. L_μ is thus longer than the effective visible track in the detector. Q_i is, as before, the measured amplitude of the i-th OM. To remove the contribution from background light using the causality criteria embedded in the reconstruction algorithm, only the hits used in the final tracking step are considered. Finally, the quantity ϵ represents the overall ANTARES light detection capability. This quantity depends on the geometrical position and direction of the muon track. It is derived on an event-by-event basis as

$$\epsilon = \sum_{i=1}^{N_{\mathrm{OM}}} \exp\left(-\frac{r_i}{\lambda_{\mathrm{abs}}}\right) \cdot \frac{\eta_i(\vartheta_i)}{r_i}. \tag{4.16}$$

Here the sum runs over all the active optical modules. The distance from the muon track, r_i, and the photon angle of incidence, ϑ_i, are calculated for each OM: ϑ_i is used to obtain the corresponding angular acceptance $\eta_i(\vartheta_i)$ of the involved OM. The distance r_i is used to correct for the light absorption in water (with characteristic absorption length $\lambda_{\mathrm{abs}} = 55\,\mathrm{m}$) taking into account the light distribution within the Cherenkov cone.

4.5   Monte Carlo simulations

Monte Carlo simulations are necessary to understand the behaviour the detector. A software chain has been developed to take care of the simulation of all the events that can be detected in ANTARES [120]. The simulation chain can be considered subdivided into three main steps:

1. Event generation: the physical properties of particles (neutrinos or muon bundles) are generated in the proximity of the detector.

2. Particle and light propagation: particles are propagated through the detector and the light coming from Cherenkov effect is simulated and propagated to the OMs.

3. Data acquisition simulation: the PMT behaviour, the data acquisition electronics are simulated and filtering is applied. The optical background is also added.
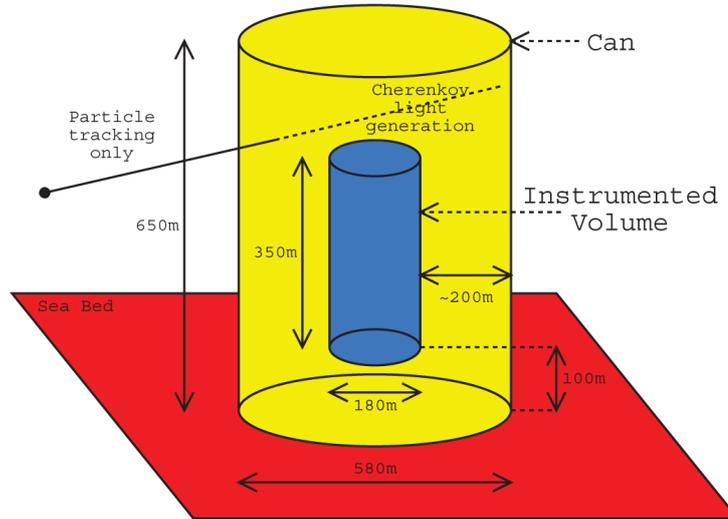
Figure 4.8: Schematic view of the ANTARES can (in yellow), anchored to the sea-bed (in red) and containing the detector instrumented volume (in blue).

4.5.1 Event generation

For the generation of neutrino interactions and the simulation of atmospheric muon bundles arriving at the detector, the instrumented volume of the apparatus can be considered as a cylinder which contains all the PMTs. A larger cylinder, which is called the "can", virtually surrounds the first one. The can defines the volume within which Cherenkov light is generated in the Monte Carlo simulation §4.5.2 to determine the detector response. Outside this volume, only particle energy losses during propagation are considered. Inside it, a full simulation including the generation of Cherenkov light must be performed. The geometry of this simulation scheme is shown in figure 4.8.

Neutrino events

The dedicated *GENHEN* package is suitable for the full range of neutrino studies in ANTARES from neutrino oscillations to high-energy astrophysics, being the majority of detected neutrinos in a range of energies from tens of GeV, limited by the energy threshold of muon detection of around 10 GeV, to a multi-PeV, where the absorption of neutrinos in the Earth, which strongly attenuates the upward neutrino flux must be taken into account. To limit the influence of simulation uncertainties the following general requirements must be satisfied:

- The relevant neutrino interactions from energies of a few GeV must be correctly simulated to conservatively include the interesting energy range. At high energies this is dominated by Deep Inelastic Scattering (DIS).

- Neutrinos interacting both inside the can (volume events) and outside the can (surface events) should be simulated in the same package in the correct proportions.

- For events inside the can, the production of the hadronic shower at the interaction vertex must be simulated as charged secondary particles can contribute to the total amount of Cherenkov light observed.

- For events outside the can, high energy muons must be tracked until they stop or reach the surface of the can.

- The effect of the different media (rock and water) around the detector must be taken into account in both the neutrino interactions and muon propagation.

- For high energy neutrinos, the probability of absorption in the Earth must be calculated given the neutrino interaction cross-section and an Earth density profile. Neutrino interactions are generated in agreement to these points. A power law, $E^{-\gamma}$, is chosen for the generation spectrum of the neutrino interactions (which we will refer to as the "interacting neutrino spectrum" in the following description). This can then be weighted to different neutrino fluxes to give the event rates for specific models.

The general simulation method foresees the definition a volume around the detector which will contain all potentially observable neutrino interactions for the given energy range and the simulation of neutrino interactions within that volume. For those neutrino interactions outside the can, any muon produced is then propagated and stored if it reaches the surface of the can. To get meaningful statistics after the muon propagation stage, say a few thousand muons at or within the can, it is typically necessary to simulate some billions of neutrino interactions. Clearly, the simulation time required to completely process this number of events would be prohibitive.

The largest possible muon energy in the simulation corresponds to the upper limit on the neutrino energies specified by the user, E_{max}. Hence, the maximum muon range at this energy is R_{max}. No neutrino interacting further away from the detector than these distances can possibly produce a muon which will reach the detector. Hence we can use these distances to define our total simulation volume. Starting with this information, the full simulation then proceeds as follows:

- A cylindrical volume around the instrumented volume of the detector of radius R_{max} is defined.

- The total interacting neutrino spectrum is divided into equal bins in the $\log_{10}(E_\nu/\text{GeV})$ between E_{min} and E_{max} and the number of events N, to generate in each bin is calculated.

- For each energy bin, a maximum range in rock and water using the maximum energy in that bin can be calculated.

- For each energy bin the numerical integration of the cross-section in *LEPTO* is performed and the generation for just this energy range is initialised.

- Looping over the number of events to generate in this scaled volume, N_{scaled}:

  1. The energy of the interacting neutrino is sampled from the $E^{-\gamma}$ spectrum within the energy range of this bin.
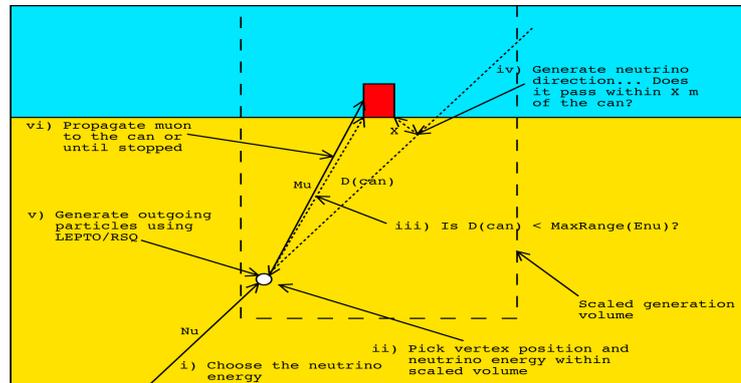
Figure 4.9: Neutrino interaction generation process in *GENHEN*. See text for the complete description of the neutrino interaction simulation.

2. The neutrino position is chosen from within the scaled volume.

3. Whether or not the vertex is inside the can is determined. If it is outside, the shortest distance from the neutrino vertex position to the can is calculated. If this distance is greater than the maximum muon range at that neutrino energy, no muon produced by this neutrino will ever reach the can and the event is rejected with no further processing.

4. The neutrino direction is sampled from an isotropic distribution. For events outside the can, it is calculated whether the distance of closest approach of the neutrino direction to the can is greater than some user specified distance.

5. For each event, the neutrino interaction is simulated using the appropriate code to get the final state particles at the neutrino interaction vertex.

6. For events inside the can, all these particles are recorded (position, direction, energy, etc) for further processing. For events outside the can, only the muons are kept.

7. For those events which are kept, the "event weights" are calculated and all the event informations written on disk.

- On completion of all the stages above, a record of every one of the neutrino interactions which produced at least one particle at or inside the can is obtained.

Figure 4.9 schematically shows the neutrino production procedure

Event weighting

Power law spectra are generated by *GENHEN*. Events can then be weighted properly to obtain the effective rates at the detector. To derive the appropriate event weight, the following parameters need to be defined:

- V_{gen} (m^3): Total generation volume.

- I_θ (sr) = $2\pi(\cos\theta_{max} - \cos\theta_{min})$: Angular phase space factor depending on the specified range of $\cos\theta_\nu$. It is the integral of the solid angle.

- I_E: Energy phase space factor depending on the input spectral index, γ for the neutrino interaction rate. If $\gamma = 1$, $I_E = \ln(E_{max}/E_{min})$ otherwise $I_E = (E_{max}^{1-\gamma} - E_{min}^{1-\gamma})/(1-\gamma)$. It is the integral of the generation spectrum between the minimum and maximum energies.

- $\sigma(E_\nu)$ (m^2):Total neutrino cross-section of the charged current neutrino interaction.

- $\rho\, N_A$ (m^3): Total number of target nucleons per unit volume (ρ is the target density and N_A the Avogadro's number).

- $P_{Earth}(E; \theta)$: Probability of neutrinos to penetrate the Earth.

- N_{total} : Total number of generated events.

- t_{gen} (s): The (arbitrary) time represented by the simulation.

The generation weight w_{gen} is then defined as:

$$w_{gen} = V_{gen}\,\rho N_A\,\sigma P_{Earth}\,I_\theta\,I_E\,E^\gamma\,t \qquad (4.17)$$

and it allows by construction to have a "global" weight w_{global} for each event in order to represent any given differential flux $\phi(E_\nu, \theta_\nu)$:

$$w_{global} = w_{gen} \times \phi(E_\nu, \theta_\nu) \qquad (4.18)$$

Atmospheric muons

The most abundant signal for a neutrino telescope is due to high energy muons resulting from the extensive air showers produced by interactions of CRs in the upper atmosphere. Although the ANTARES telescope is located at large depth under the sea, taking advantage of the shielding effect offered by the water, a large flux of high energy atmospheric muons will reach the active volume of the detector. The atmospheric muons represent an insidious background for track reconstruction as their Cherenkov light can mimic fake upward-going tracks. This kind of signatures can be confused with the cosmic neutrino signal. In addition, atmospheric muons are a useful tool to test offline analysis software, to check the understanding of the detector and to estimate uncertainties.

Atmospheric muon bundles arriving at the detector can be accurately reproduced using a complete extensive air shower simulation, as done by the *CORSIKA* program [121]. In this case the primary cosmic ray interaction at the top of the atmosphere is simulated, the whole CR shower is tracked to the sea level and then muons are propagated to the detector. Even if this gives a precise description of atmospheric muons at the apparatus, it is an extremely time consuming procedure and it is not possible to have a proper statistics of muon events in a reasonable processing time. In addition, large uncertainties on modelling the primary interaction as well as on the primary flux itself are present and a faster generator, even if not taking care of the full air shower development, should be preferred.

Atmospheric muon bundles are generated in ANTARES with the *MUPAGE* software [122]. *MUPAGE* is based on parametrisation of the angular and energy

distribution of muon under-water or in ice as a function of the muon bundle multiplicity. This parametrisations are taken from complete simulations and data collected with the MACRO experiment at Gran Sasso [123], extrapolated either under the sea or under an ice layer. The usage of parametric formulas allows the production of an extremely large number of events within a reasonable CPU time consumption, even if only a fixed atmospheric flux can be simulated. Since the overall uncertainty on the atmospheric muon flux can be estimated as of the order of $\pm 50\%$, this fast parametric generation can be used to get a proper simulation of the atmospheric muon background.

Atmospheric muon production ranges from $0°$ to $85°$ in zenith angle with muon multiplicity in the bundle going from 1 to 200 and the energy of simulated muon bundles goes up to $500\,\text{TeV}$. The fast generation process allows the production of a large quantity of events at the detector: the same order of magnitude of the event rate effectively seen at the detector can be produced in a computationally sustainable time.

4.5.2   Particles and light propagation

All long-lived particles which are stored as output of the physics generators are tracked through the water in the can volume using a *GEANT*-based [124] package, denoted in ANTARES as *KM3*. The composition and density of the water is adjusted to the values at the experimental site. All relevant physics processes activated (energy loss, multiple scattering, radiative processes and hadronic interactions).

Thanks to the homogeneity of the sea water, a photon-by-photon simulation for the Cherenkov light is not required, differently from what is done to describe the photon propagation through the Antarctic ice where optical properties show a dependence on the ice stratification. This means that a set of "scattering tables" containing the probability of each photon to give a hit on a PMT as a function of 5 parameters: the distance from the muon; 3 angles defining the direction of the photons with respect to the muon and to the PMT; the photon arrival time; and considering the diffusion and absorption phenomena, can be created in advance. Muons are propagated in the can volume by *MUSIC* [125]. Steps of $1\,\text{m}$ for muon tracks are considered, the ionisation energy loss and the Cherenkov light emission are calculated. The probability for each Cherenkov photon to reach PMTs is extracted from the scattering tables. Also the probability of a catastrophic energy loss is evaluated. Similar scattering tables are created for electromagnetic showers.

Hadronic showers are treated differently. In this case a large number of charged particles is produced at the interaction vertex. The computation of scattering tables for each particle would require an event-by-event simulation, and a huge amount of CPU time, because of the high variability in the hadronic shower composition. To overcome this problem, a "multi particle approximation" approach is followed. Each hadron is considered as equivalent to an electron. The electron scattering tables are used in association with opportune weights, evaluated for each hadron after many complete photon tracking simulations. The light yield from hadronic showers obtained with this technique is compatible with what is achieved with a detailed simulation.
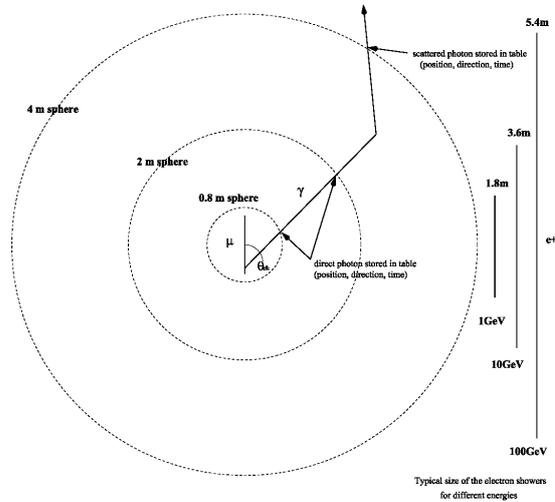
Figure 4.10: Graphical representation of the *KM3* shells used for building the hit probability tables (see text for a detailed explanation).

4.5.3 Data acquisition simulation

The detector response is simulated using the *TriggerEfficiency* program. This software consists of the addition of the optical background to the hits generated by physical events, the simulation of the electronics, and the triggering of events. The optical background can be generated and added to the MC events according to a Poisson distribution using a fixed background rate specified by the user or using a real data run. With this second option the TriggerEfficiency program adds to the PMTs a background which corresponds to a counting rate taken from real detector situation. In other words, it takes into account not only the background due to the radioactive salt decay but also any kind of biological activities that can occur in sea water (e.g. bioluminescence, biofouling) and temporary problems related with the electronics (e.g. charge saturations, temporary power off of single PMTs, "sparks").

The front-end ARS chip integrates the analogue signal from the PMT over a typical time window of 25 ns. This is simulated by summing the number of detected photons in that window. After the integration, the ARS cannot take data for about 250 ns. A second ARS, connected to the same PMT, digitises signals arriving afterwards. The time resolution for single photo-electron signals is 1.3 ns and decreases for higher amplitudes. To simulate this effect, the hit times are smeared using a Gaussian function with a width $\sigma = 1.3$ ns$/\sqrt{N_\gamma}$, where N_γ is the number of simultaneously detected photons. The so-called "level zero" (L0) trigger selects hits that have a charge greater than a low threshold – typically 0.3 photo-electrons (p.e.). The amplitude measurement is then simulated by smearing the integrated number of photons with an empirical function. This function results in a (roughly Gaussian) smearing of about 30%. The dynamic range of the charge integration has a saturation level which corresponds to about 20 photo-electrons.

MC events are triggered with the same trigger algorithm used for real data. The first level trigger (L1) is built up of coincidence hits in the same storey

65

within a 20 ns time window, and single hits with a large charge amplitude, grater than a "high threshold" tunable from 2.5 p.e. to 10 p.e. A trigger logic algorithm, a level 2 trigger (L2), is then applied to data and operates on L1 hits. The main physics triggers are the 3D-directional scan logic trigger "3N" and cluster logic trigger "2T3".

The 3N trigger processes all data and declares an event as soon as a minimum number of L1 hits are found within a 2.2 μs time interval. In addition, each pair of L1 hits should verify the causality relation:

$$\Delta t_{ij} \leq \frac{d_{ij}}{c/n} + 20ns \qquad (4.19)$$

where Δt_{ij} and d_{ij} are the time difference and the spatial distance between (hit)$_i$ and (hit)$_j$ respectively, c is the speed of light and n the index of refraction of the sea water.

The 2T3 trigger is based on the definition of a "T3 cluster" of hits. A T3 cluster is defined when two L1 hits among three adjacent storeys are in coincidence. The coincidence time window is set to 100 ns in case that the two storeys are adjacent, and to 200 ns in case of next to adjacent storeys. The 2T3 trigger logic requires at least two T3 clusters within a time window of 2.2 μs.

Run-by-run approach

The conditions in a marine environment are not stable and constant in time and they directly effect data acquisition in a under-water neutrino telescope such as ANTARES. Biological [112] and physical phenomena [127] show evolving trends on seasonal timescales producing a periodical change of the rates registered at the detector. Short term variations are also present as the sea current velocity affects the optical rates. Apart from these environmental effects, also the fact that not all the detector elements are taking data at a certain moment of time, because of temporary or permanent malfunctioning of optical modules or lack of connection to some part of the apparatus, can change the data acquisition condition. Finally, according to the sea conditions, different triggers can be applied to handle the situation.

A correct Monte Carlo simulation of the detector should reproduce all these effects as reliably as possible. An efficient way to account for the variations of the optical background to the Cherenkov light due to physics signals is to extract related information directly from the data. The *TriggerEfficiency* program can take this information from data files themselves and use it in the processing of the physics output of the Monte Carlo chain. At the same time it can be connected to a database interface where all information on the data acquisition conditions of each detector element is stored for each data acquisition run [128].

Chapter 5

Measuring the atmospheric neutrino background

High energy cosmic rays interacting at the top of the atmosphere produce large cascades of subatomic particles. Out of the multitude of particles in these extensive air showers, only muons and neutrinos reach an under-water detector and can be detected. They represent a background for a neutrino telescope since their event rate is much larger than that of the expected cosmic signal.

As shown in section 2.1.4, atmospheric muons can be rejected selecting upward-going tracks, since only neutrinos can traverse the Earth. The rejection of atmospheric neutrinos is possible on a statistical basis thanks to the fact that their energy spectrum, derived from the primary CR spectrum at the top of the atmosphere, is steeper than the cosmic signal. However, this atmospheric background can bring valuable information on the detector performance, providing a calibration source for the energy reconstruction and give an insight on systematic effects affecting the neutrino detection.

The measurement of the atmospheric neutrino flux obtained using ANTARES data is described in this chapter. The work presented here is completely original and has been published on a peer-reviewed journal [129].

5.1 Atmospheric neutrinos

Up to $\sim 100\,\mathrm{TeV}$, muons and neutrinos in the atmosphere are produced mainly by decays of charged pions and kaons in the cosmic ray air shower and their spectra directly derive from the kinematics of the $\pi \to \mu\nu$ and $K \to \mu\nu$ decays. Additional lower energy neutrinos are produced by the further muon decays from these processes. The corresponding ν_μ flux is usually referred to as the *conventional atmospheric neutrino flux* and its intensity is expressed as

$$\frac{d\Phi_\nu}{dE_\nu d\Omega}(E_\nu, \theta) = A_\nu E_\nu^{-\gamma_p}\left(\frac{1}{1 + \frac{aE_\nu}{\epsilon_\pi}\cos\theta} + \frac{B}{1 + \frac{bE_\nu}{\epsilon_K}\cos\theta}\right), \qquad (5.1)$$

in units of $\mathrm{cm}^{-2}\,\mathrm{s}^{-1}\,\mathrm{sr}^{-1}\,\mathrm{GeV}^{-1}$. The *scale factor* A_ν, the *balance factor* B, which depends on the ratio of muons produced by kaons and pions, and the a, b coefficients are parameters which can be derived from Monte Carlo computation,

numerical approximations or from experimental data. The quantity ϵ_i (the *characteristic decay constant*) corresponds to the energy at which the hadron interaction and decay lengths are equal. For pions and kaons, $\epsilon_\pi = 115\,\text{GeV}$ and $\epsilon_K = 850\,\text{GeV}$, respectively. Below this energy scale, hadrons are more likely to decay while, at higher energies, their Lorentz factor γ is large enough to allow their interaction while traversing the atmosphere. This causes a steepening of the resulting neutrino flux as less neutrinos are produced at higher energies.

An analytical description of the neutrino spectrum above $100\,\text{GeV}$ is given by the Volkova parametrisation [130]. The flux of the conventional atmospheric neutrinos are also provided by the *Barr et al.* [92, 131] and *Honda et al.* [132] calculations. These evaluations of the neutrino flux come from detailed three dimensional simulations of the atmospheric shower development at a certain location, in order to account for the local intensity of the magnetic field which influences cosmic ray spectra at low energies. The expected power-law spectrum of conventional atmospheric neutrinos for $E_\nu \gg \epsilon_\pi, \epsilon_K$ can be approximated with

$$\frac{d\Phi_\nu}{dE_\nu}(E_\nu) = A'_\nu E_\nu^{-\gamma_\nu} \ , \tag{5.2}$$

where $\gamma_\nu \simeq \gamma_p + 1$.

The major uncertainties in the calculations of the atmospheric neutrino flux arise from the limited knowledge of the composition, the absolute normalisation and the slope γ_p of the primary cosmic ray spectrum, as well as from the treatment of hadronic interactions in particle cascades in the atmosphere. The global uncertainty on the normalisation of the conventional atmospheric neutrino flux is at the level of 25-30% [132, 133], though it varies in amplitude with energy.

Charmed hadrons, also decaying to neutrinos, are produced at the interaction point of primary cosmic rays with air nuclei and have a much shorter lifetime, approximately 5 to 6 orders of magnitude smaller than pions and kaons. As a consequence, there is no competition between interaction and decay: a harder neutrino energy spectrum, the so-called *prompt neutrino flux*, is a clear signature of the charmed component. There is significant variability in the calculations of the prompt neutrino flux [134, 135, 136] depending on the modelling of the hadronic interactions, the choice of the gluon distributions and the renormalisation and factorisation scales.

5.2   Unfolding of the atmospheric ν_μ flux

Since the atmospheric neutrino energy spectrum is steeply falling and because of the limited capability of energy estimation for a neutrino telescope, an unfolding procedure must be used in order to draw the actual energy spectrum from the measured event-by-event distribution. This procedure takes into account the stochastic nature of the muon energy losses, the large uncertainty in the reconstructed energy, the detection inefficiencies and the fact that only the daughter muon energy is measured.

The problem to be solved is a set of linear equations of the form

$$A\mathbf{e} = \mathbf{x} \ . \tag{5.3}$$

The vector $\mathbf{e}$ represents the true unknown distribution in a discrete number of intervals, the vector $\mathbf{x}$ is the measured distribution and the matrix A, called the "response matrix", is the transformation matrix between the two distributions. The response matrix is built using Monte Carlo simulations.

A simple direct inversion of the response matrix leads in most cases to rapidly oscillating solutions and large uncertainties due to the fact that the matrix A is *ill-conditioned* [137]: minor fluctuations in the data vector $\mathbf{x}$ can produce large fluctuations in the solution $\mathbf{e}$.

One of the methods used to solve this problem is the *singular value decomposition* (SVD) [138]. The response matrix is decomposed as $A = USV^T$, where S is a diagonal matrix and U and V are orthogonal matrices. This is equivalent to expressing the solution vector $\mathbf{e}$ as a sum of terms weighted with the inverse of the singular values of the matrix S. Small singular values can however enhance statistically insignificant coefficients in the solution expansion, leading to the same problem appearing when directly inverting the response matrix. This problem can be overcome by imposing an external constraint on how the solution is expected to behave. The process of imposing such a constraint is called *regularisation*. The constraint used in our procedure and described in ref. [138] controls the curvature of the solution, not allowing vector $\mathbf{e}$ to exhibit unphysical bin-to-bin fluctuations.

Another unfolding method, which does not rely on the regularisation procedure, is the iterative method based on the *Bayes' theorem* in ref. [139]. The Bayes' theorem, translated to this case, states that the probability $\mathcal{P}(E_i|X_j)$ that E_i is the true energy, given the measurement of a value X_j for the energy estimator, is equal to

$$\mathcal{P}(E_i|X_j) = \frac{A(X_j|E_i)p_0(E_i)}{\sum_{l=1}^{n_E} A(X_j|E_l)p_0(E_l)} \; , \tag{5.4}$$

where $A(X_j|E_i)$ is the probability (calculated from Monte Carlo simulations) of measuring an estimator value equal to X_j when the true energy is E_i. This quantity corresponds to the element A_{ij} of the response matrix. The *a priori* probability $p_0(E_j)$ is the expected energy distribution at the detector derived from theoretical expectations and Monte Carlo simulations. For a given estimator distribution, the energy spectrum at the detector can be obtained applying eq. 5.4 iteratively. At the n-th iteration, the energy distribution at the detector $p_n(E_j)$ is calculated taking into account the observed number of events in the estimator distribution and the expectations from $p_{n-1}(E_j)$. The result rapidly converges towards a stable solution. The number of iterations to be performed is optimised by applying the procedure to different Monte Carlo samples and studying the convergence of the obtained solutions. A small number of iterations biases the unfolding result towards the prior probability $p_0(E_j)$, while further iterations beyond the point where convergence is reached enhances statistical fluctuations in the solution.

Both mentioned unfolding procedures are used in this analysis and are implemented in the *RooUnfold* package [140] as part of the ROOT framework [141].

5.2.1 Atmospheric data analysis

In order to estimate the atmospheric neutrino energy spectrum, ANTARES data acquired from December 2007 to December 2011 have been analysed. This data sample has an equivalent livetime of 855 days.

The two unfolding methods described previously are applied on data reconstructed using the *energy likelihood* and the *energy loss* methods described in section 4.4.2. The former is used for the SVD, the latter for the Bayesian unfolding procedure. Both methods require a high purity sample. The presence of wrongly-reconstructed atmospheric muons would corrupt the final result. All cuts are optimised on a Monte Carlo simulated sample. A 10% fraction of the data is initially used to check the agreement between the observed and expected quantities both on downward-going (atmospheric muons) and upward-going (atmospheric neutrinos) events. The remaining 90% of the data set is *unblinded* only when all the cuts and optimisation procedures have been defined. In addition, the two analyses are kept independent up to the unblinding of the data sample. Finally the two results are merged.

Unfolding method based on the Bayes' theorem

The energy of the muon reconstructed using the *energy loss method* is used to derive the neutrino energy spectrum through the unfolding method based on the Bayes' theorem. In order to suppress the atmospheric muon background, the angular region of accepted tracks is restricted to $\theta > 100°$. An angular error $\beta < 1°$ is required on the reconstructed tracks. In addition, a selection based on the reconstruction quality parameter Λ is applied. Figure 5.1 shows the Λ distribution for data and MC tracks with $\beta < 1°$ and $\theta > 100°$. Asking for $\Lambda > -4.9$ the contamination of wrongly reconstructed atmospheric μ is $\sim 0.3\%$.

The response matrix is built by weighting Monte Carlo events according to the flux described in ref. [131] with no prompt contribution. The expected atmospheric neutrino rate is 1.8 events per day.

The precision on the reconstructed energy E_μ^{Rec} depends on the true muon energy E_μ^{MC}. The quantity

$$\delta E_\mu \equiv \log_{10} \frac{E_\mu^{\mathrm{Rec}}}{E_\mu^{\mathrm{MC}}} \tag{5.5}$$

is used to estimate the energy resolution of the reconstruction. The standard deviation of a Gaussian fit for different intervals of the Monte Carlo true muon energy achieved with this method has an almost constant value $\sigma_{\delta E_\mu} \simeq 0.4$ over the considered energy range.

The comparison between the distribution of the quantities used to construct the energy estimator ρ (eq. 4.15) for data and Monte Carlo events is shown in figure 5.2. The total expected number of Monte Carlo events is $\sim 25\%$ lower than the measurement, within the expected flux normalisation uncertainty.

The relation between the distribution of the neutrino energy and the observable ρ is described by the response matrix constructed via Monte Carlo. The iterative unfolding method based on the Bayes' theorem moves the distribution of the observed estimator towards the real neutrino energy distribution starting from an *a priori* hypothesis. The optimal value of the number of iterations is established using a χ^2 test on different simulated data sets (from now on referred
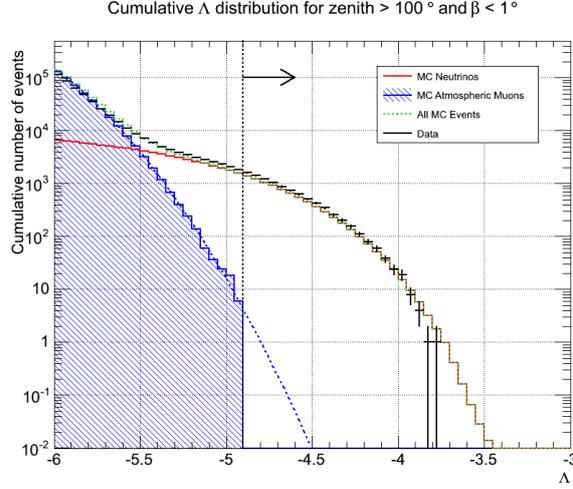
Figure 5.1: Comparison between data and Monte Carlo for the Λ track quality parameter, for upward-going events reconstructed with zenith angle larger than $100°$ and with angular error estimate smaller than $1°$. Black crosses represent the cumulative distribution for data, red line is for simulated atmospheric neutrinos and the blue histogram shows the distribution for wrongly reconstructed atmospheric muons. A blue dashed line shows an extrapolation of the atmospheric muon distribution in order to evaluate the muon contamination in the sample for the cut value, shown with a dashed black line.

to as "pseudo-data"), which are unfolded for different number of iterations. The spectral index corresponds to the parameter γ_ν in eq. 5.2 and it takes the value $\gamma_\nu = 3.63$ when the neutrino flux is averaged over the lower hemisphere. The optimal number of iterations is found to be equal to five using a χ^2 test comparing the unfolded result and the true neutrino spectrum of pseudo-data samples. In particular, neither an enhancement of statistical fluctuations deriving from a larger number of iterations, nor a bias towards the *a priori* spectrum used to construct the response matrix are observed.

Figure 5.3 shows the result of the unfolding procedure applied on pseudo-data with energy spectrum flatter by a factor $E_\nu^{+0.1}$ with respect to the *a priori* spectrum. This pseudo-data set has an overall normalisation 20% larger than the *a priori* one, more in agreement with the measured number of events in the data. The points in figure 5.3 represent the result of the unfolding of this pseudo-data set. The deviations between the true distribution and the unfolded one will be considered in the discussion of systematic uncertainties on §5.3.1

Unfolding method based on singular value decomposition

The muon energy spectrum reconstructed using the *energy likelihood method* is used to build the vector $\mathbf{x}$ in eq. 5.3 applying the SVD unfolding method. The cut on the reconstruction quality parameter Λ is the same as for the energy loss method ($\Lambda > $ -4.9). The cut on β is slightly more stringent ($\beta < 0.5°$), but the zenith angle region is larger, as only events with $\theta < 90°$ are rejected.
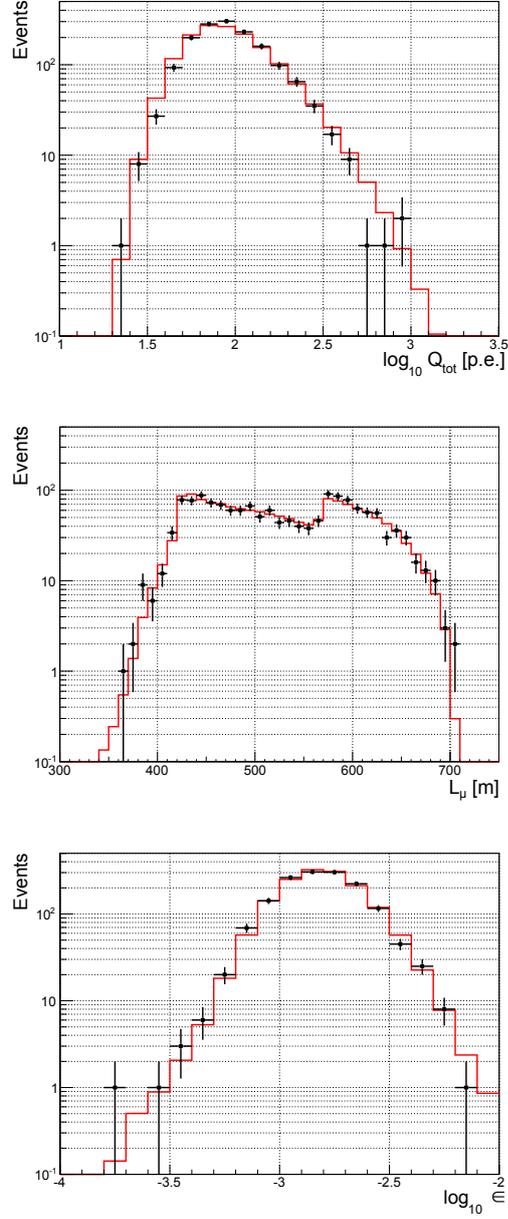
Figure 5.2: Comparison between data (black crosses) and simulations (red line) for the quantities used to construct the energy loss estimator ρ, eq. 4.15. (Top) Distribution of the total measured amplitude Q_{tot} (in photo-electrons) on the optical modules involved in the events; (Middle) muon track length in the detector region; (Bottom) light collection capability defined in eq. 4.16. Only events passing the selection criteria of the *energy loss method* are drawn. The Monte Carlo prediction is scaled by a factor 1.25.
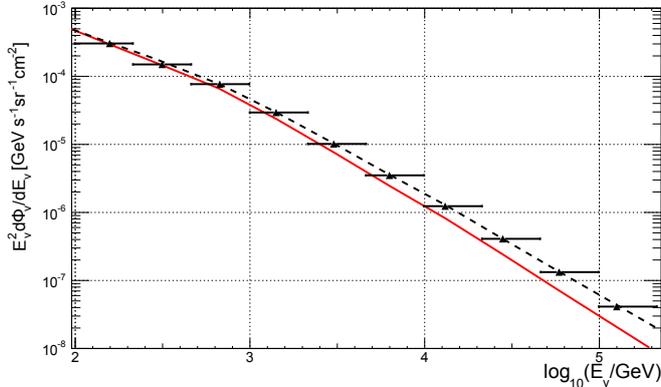
Figure 5.3: Unfolding of a known spectrum. The red solid line is the energy spectrum from ref. [131] used as the *a priori* probability for the bayesian unfolding of pseudo-data generated according to an injected spectrum (black dashed line). The unfolded result (black symbols) is shown without error bars.

The response matrix is built weighting Monte Carlo events according to the conventional flux from ref. [131] plus the prompt contribution from ref. [136]. The corresponding neutrino event rate is 1.7 events per day and the expected muon contamination below 0.2%. The estimated energy resolution eq. 5.5 achieved with this method ranges from $\sigma_{\delta E_\mu} \simeq 0.45$ at $E_\mu^{\mathrm{MC}} = 500\,\mathrm{GeV}$ to $\sigma_{\delta E_\mu} \simeq 0.3$ when $E_\mu^{\mathrm{MC}} = 10^3\,\mathrm{TeV}$.

Figure 5.4 shows the comparison between the reconstructed energy of data and simulated muons using the *energy likelihood method* for events passing the selection (simulation events are normalised to the data). Also in this case, the simulation prediction is $\sim 25\%$ lower than data.

This distribution is the starting point for the application of the SVD unfolding procedure in order to derive the neutrino energy spectrum at the detector. The result of the unfolding depends on the choice of the *regularisation parameter*, i.e. how strongly the regularisation condition acts in smoothing unexpected oscillating components due to statistical fluctuations. A large value of the regularisation parameter imposes stronger constraints on the solution with a possible bias towards the assumed underlying spectrum. The regularisation parameter is chosen by examining the distribution of the absolute values of the expansion coefficients, as described in ref. [138]. The values of the expansion coefficients drop rapidly as the singular values decrease, reaching a level where they are compatible with zero, i.e. following a normal distribution with zero mean and standard deviation equal to one. The optimal regularisation parameter corresponds to the square of the singular values above which the expansion coefficient becomes compatible with zero. In this way too small singular values are excluded from the expansion. This avoids the enhancement of large fluctuations in the solution, behaving as a Fourier low-pass filter which progressively damps out insignificant terms in the solution expansion. As for the Bayesian unfolding method, the performance of the SVD unfolding has been tested on Monte Carlo samples, producing similar results to those shown in figure 5.3.
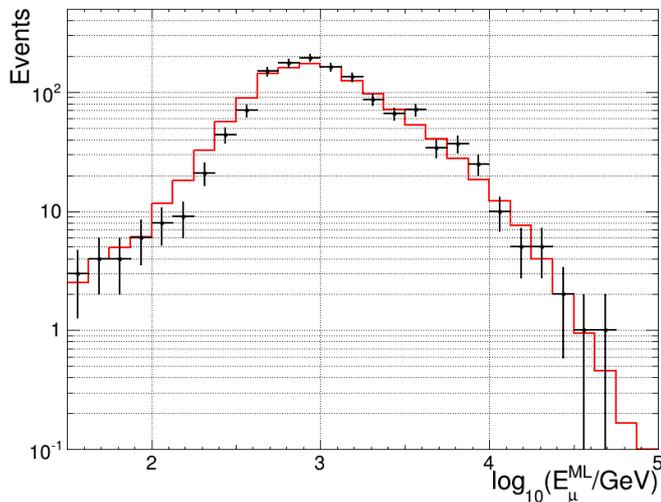
Figure 5.4: Data (black crosses) and Monte Carlo (red line) comparison for the maximum likelihood muon energy estimator E_μ^{ML}, for events passing the selection cuts. This distribution is obtained at the end of the procedure, after the data unblinding (see text). The Monte Carlo prediction is scaled by a factor 1.25.

5.3 Computation of the ν_μ energy spectrum

The output of the unfolding procedure is the number of events per energy bin in the considered livetime and represents a detector dependent quantity. The top panel of figure 5.5 shows the neutrino energy distribution at the detector resulting from the two methods. These energy distributions are dependent on the selection criteria and on the analysed solid angle which are different for the *energy likelihood* and *energy loss* methods.

A detector-independent spectrum can be derived considering the detection and selection efficiencies of the apparatus as a function of the neutrino zenith angle and energy. These effects are accounted for in the so-called "neutrino effective area" of the detector, $A_\nu^{\mathrm{eff}}(\theta, E_\nu)$. In general, this quantity depends on the neutrino cross-section and differs between neutrinos and antineutrinos. Here, A_ν^{eff} is defined as the ratio between the number of selected events and expected number of atmospheric neutrinos and antineutrino as a function of the zenith angle θ and neutrino energy E_ν. In addition it depends on the survival probability of neutrinos crossing the Earth and on the muon detection and selection efficiency. The bottom panel of figure 5.5 shows the neutrino effective area as a function of E_ν for the two methods used in this analysis. The differences between the two include the effects of the different quality cut on the reconstructed tracks.

The effective area is used to relate the energy distribution at the detector to the energy distribution at the surface of the Earth. A correction factor for the effective area is contained because the *energy loss* and *energy likelihood* methods consider two different zenith ranges for the event selection.
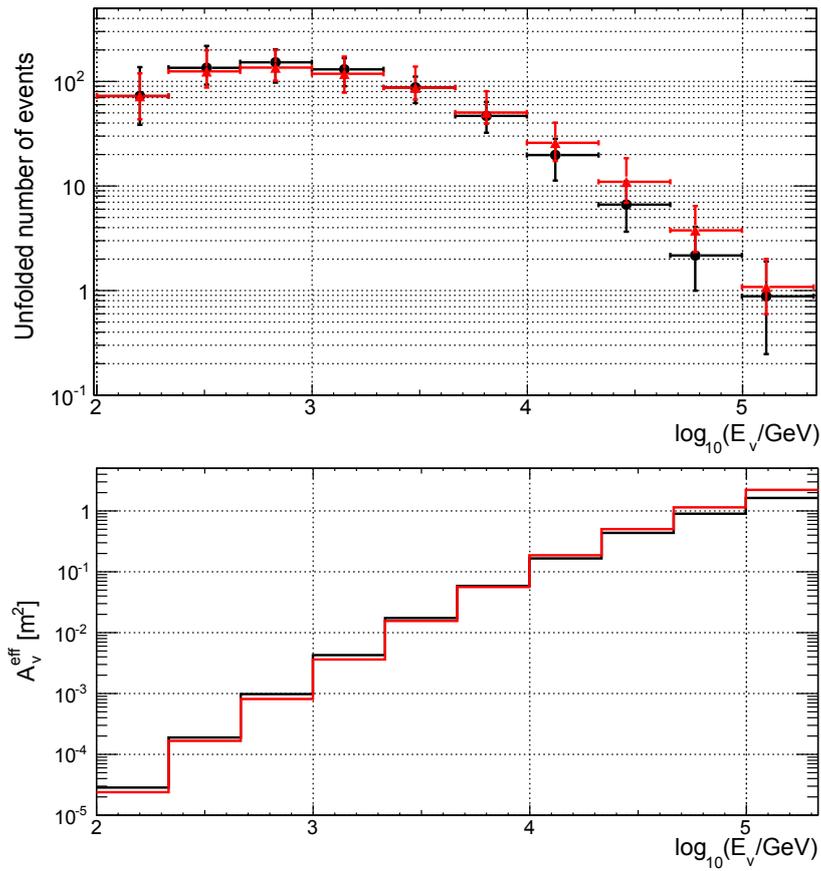
Figure 5.5: Top: unfolded energy distribution at the detector for the energy likelihood (red) and the energy loss (black) methods. The numbers correspond to events per bin per year of effective livetime. Bottom: corresponding neutrino effective area for upward-going neutrinos for the two methods.

5.3.1 Systematic uncertainties

The result of the unfolding process is dependent on Monte Carlo simulations via the construction of the response matrix. Simulations indeed depend on a number of parameters related to the light collection efficiency of the optical modules, the light propagation properties of water and the dependency of the light detection probability to the direction of arrival of photons on the PMTs. Uncertainties on these parameters can systematically influence the unfolding result.

The default response matrix is constructed considering the current best knowledge of these quantities. Systematic effects coming from their uncertainty are evaluated using different specialised simulation data sets. A number of Monte Carlo samples has been produced considering the relative uncertainties related to each of them. Each modified Monte Carlo sample has been used as pseudo-data and unfolded. The deviation from the spectrum obtained when the default value of the parameter is considered is taken as systematic uncertainty. The systematic uncertainties as a function of the neutrino energy for the two unfolding procedures are different because of the different unfolding methods and constructions of the energy estimators.

Figure 5.6 shows the systematic uncertainty as a neutrino energy. The largest uncertainty arising from the *energy loss* or from the *energy likelihood* methods is considered in each bin. The total uncertainty (black full line) is computed as the quadratic sum of each contribution, separately for positive and negative deviations. The differences between the spectra obtained with the two energy estimators with respect to the average value is shown as the thin black line.

The overall sensitivity of the optical modules (red continuous line) has been modified by $\pm 10\%$. This includes the uncertainty on the conversion efficiency of a photon into a photo-electron on the PMT photo-cathode as well as other effects related to the OM efficiency. An additional uncertainty related to the optical modules is connected to the angular acceptance, i.e. the angular dependence of the collection efficiency of each OM. This affects the measurement by less than 10% over the whole analysed energy range. The uncertainties on water properties have been studied and are taken into account by scaling up and down by 10% the absorption length of light in water with respect to the nominal value (blue dashed line).

The effects due to the uncertainty in the neutrino flux used in the response matrix of the unfolding procedures include the possible contribution of prompt neutrinos [135], the effect of a slope change of ± 0.1 in the *a priori* spectral index γ_ν and the effect due to the chosen number of iterations. The uncertainties deriving from these effects, not shown in figure 5.6, are always below 10%.

The unfolding procedure result is affected by the resolution of the energy estimators, as well as by the performance of the unfolding method and the event selection criteria. In particular the *energy likelihood* method is more sensitive to variations of water properties, while the *energy loss* method has a larger dependence on OM efficiency. The statistical uncertainty (magenta short dashed line) is relevant only for the highest energy bins.
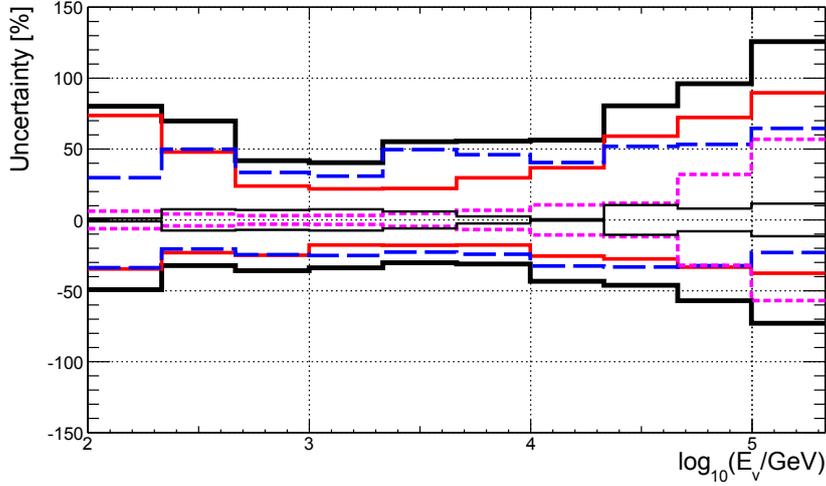
Figure 5.6: Systematic uncertainties calculated for each neutrino energy bin. Red continuous line represents the effects given by a $\pm 10\%$ change of the OM efficiency with respect to the default value; blue dashed line is for a $\pm 10\%$ change in the absorption length in water; magenta short dashed line is the statistical uncertainties. The thick black line shows the estimated total uncertainty while the thin black line represents the relative difference between the two unfolding results. The effects from the OM angular acceptance and the change in the underlying event weighting model (see text) are not shown in the figure.
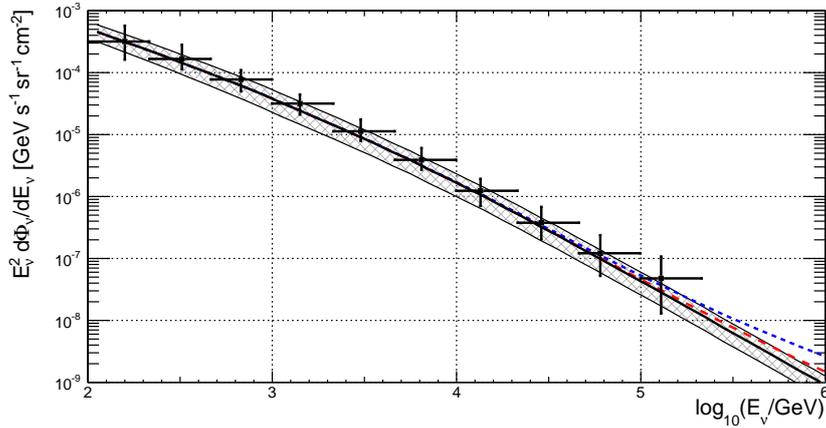
Figure 5.7: Atmospheric neutrino energy spectrum obtained with the ANTARES neutrino telescope using 2008-2011 data. The flux reported here is multiplied by E^2 and compared with the expectations from ref. [131]. The gray band corresponds to the uncertainty in the flux calculation from ref. [133]. The flux obtained by adding to the conventional flux the prompt contributions from ref. [135] (red dashed line) and ref. [136] (blue short-dashed line) is also drawn.

Energy range $\log_{10}(E_\nu/\text{GeV})$	$\log_{10}(\overline{E}_\nu/\text{GeV})$	$\overline{E}_\nu^{\,2} \cdot d\Phi_\nu/dE_\nu$ [GeV s^{-1} sr^{-1} cm^{-2}]	% Uncertainty
$2.00 - 2.33$	2.20	3.2×10^{-4}	$-49, +80$
$2.33 - 2.66$	2.51	1.7×10^{-4}	$-32, +69$
$2.66 - 3.00$	2.83	7.8×10^{-5}	$-36, +41$
$3.00 - 3.33$	3.15	3.2×10^{-5}	$-34, +40$
$3.33 - 3.66$	3.48	1.1×10^{-5}	$-30, +55$
$3.66 - 4.00$	3.81	3.9×10^{-6}	$-31, +56$
$4.00 - 4.33$	4.13	1.2×10^{-6}	$-43, +56$
$4.33 - 4.66$	4.46	3.8×10^{-7}	$-46, +80$
$4.66 - 5.00$	4.78	1.2×10^{-7}	$-57, +96$
$5.00 - 5.33$	5.11	4.8×10^{-8}	$-73, +125$

Table 5.1: The unfolded atmospheric neutrino energy spectrum from the ANTARES neutrino telescope. Each row shows the energy range of the bin; the weighted central value of the neutrino energy $\overline{E}_\nu$ in the bin; the flux multiplied by $\overline{E}_\nu^{\,2}$ and the percentage uncertainty on the flux.

5.3.2 Measured atmospheric neutrino spectrum

The atmospheric neutrino spectrum is computed considering the median value of the neutrino energy in each bin. Thus, the steep decrease of the energy spectrum inside the bin is taken into account. The flux is obtained by dividing the contents of the two histograms presented in figure 5.5 and averaging the results of the two methods. The measured atmospheric neutrino energy spectrum for $\theta > 90°$ is presented in figure 5.7 and the values are reported in table 5.1. The differences for each method with respect to their average value are much smaller than most of the considered systematic uncertainties (see next section) and are shown in figure 5.6 as a thin black line. The best fit value for the neutrino spectral index parameter is $\gamma_{\text{meas}} = 3.58 \pm 0.12$, to be compared with the value of $\gamma_\nu = 3.63$ obtained when the *a priori* pseudo-data set is used. The uncertainties computed previously are reported.

Figure 5.8 shows the result of the present measurement, where the atmospheric ν_μ energy spectrum is averaged over zenith angle from $90°$ to $180°$ compared to theoretical computations and experimental results. The black line represents the conventional Bartol neutrino flux [131]. A decrease above $E_\nu \sim 100\,\text{TeV}$ is expected due to the change of the spectral index γ_p of the primary cosmic ray flux above the *knee* region ($E_p \geq 3 \times 10^{15}\,\text{eV}$). The results from the Antarctic neutrino telescopes AMANDA-II [142] and IceCube40 [143] are also shown. These two measurements consider the zenith angle flux from $100°$ to $180°$ and $97°$ to $180°$, respectively. Assuming the expected angular distribution from the Bartol theoretical model, the flux integrated in the region $\theta > 90°$ is larger than that obtained for $\theta > 100°$ by factors of $\sim 3\%$, 8%, 25% and 40% at 0.1, 1, 10 and $100\,\text{TeV}$, respectively and is consistent with results obtained under ice. The energy spectrum measured by ANTARES has a spectral index parameter $\gamma_{\text{meas}} = 3.58 \pm 0.12$ and the overall normalisation is 25% larger than expected in ref. [131], almost uniformly in the measured energy range. This
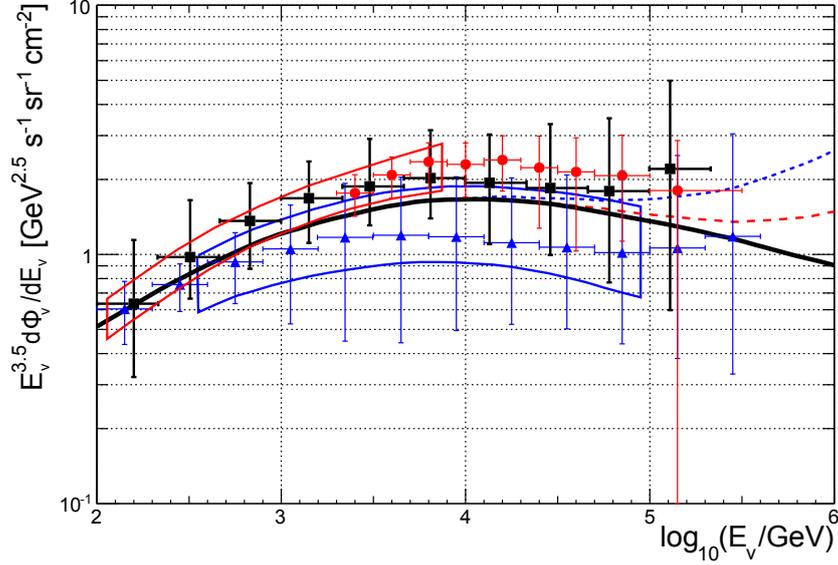
Figure 5.8: The atmospheric neutrino energy spectrum $E_\nu^{3.5}d\Phi_\nu/dE_\nu$ measured in this work in the zenith angle region $\theta > 90°$ (black full squares). The full line represents the ν_μ flux from ref. [131]. The red and blue dashed lines include two prompt neutrino production models from ref. [135] and ref. [136], respectively. All theoretical expectations are zenith-averaged from $90°$ to $180°$. The result of the AMANDA-II unfolding [142] averaged in the region $100°$ to $180°$ is shown with red circles and that of IceCube40 [143] zenith-averaged from $97°$ to $180°$ is shown with blue triangles. The red region corresponds to the ν_μ measurement from ref. [144], and the blue one the IC40 update from ref. [146].

larger normalisation is also compatible with measurements from the MACRO underground experiment [145].

Chapter 6

Search for cosmic neutrinos from the Galactic Plane

The discovery of cosmic neutrinos by the IceCube Collaboration has been described in details in section 2.2. Though IceCube does not claim any directional excess, a North/South asymmetry can be seen in the data sample and an enhancement of the neutrino production from the central region of the Milky Way can be considered a possible source of this excess in the Southern sky. The ANTARES neutrino telescope provides the best limits on neutrino sources located in the Southern sky since it can exploit track-like events coming from ν_μ CC interactions, with median angular resolution of 0.4 degrees [78]. Because of its good exposure to the central part of the Galactic Plane, valuable information can be given by the search of a neutrino flux in this area of the sky using a Mediterranean neutrino telescope.

In this chapter the search for an enhanced neutrino diffuse emission from a region of the sky covering a small solid angle around the centre of the Milky Way is described. An excess of cosmic neutrinos from a region of the sky can be searched for by comparing the number of events coming from this region (called "on-zone") to what is observed in similar regions with no expected signal ("off-zones"). To enhance the presumably harder neutrino signal over the background of atmospheric neutrinos, a cut which selects high energy events is defined. This approach has been already used within the ANTARES Collaboration to search for neutrino candidates from the Fermi bubbles regions [147]. The work presented in this chapter is completely original, has undergone a complete revision process in the ANTARES Collaboration and will be submitted for a publication.

6.1   Signal and background definition

An unbroken power-law behaviour is usually used to parametrise the expected energy spectrum of cosmic neutrinos: this is basically related to the acceleration mechanism of cosmic rays which is described in 1.1.2. Moreover, the IceCube Collaboration has shown that a power-law spectrum can describe rather well the neutrino signal they have observed with high significance. A natural choice for the neutrino signal would then follow this description.

The diffuse γ-ray flux observed by the LAT instrument on-board the Fermi

satellite once galactic point sources are removed can be directly related to the expected neutrino flux coming from hadronic mechanisms. For example in ref. [100] it is shown that a simple power-law extrapolation of the γ-ray flux observed in the Galactic Ridge by Fermi-LAT can fit the neutrino flux derived from the IceCube events close to that region. This extrapolation assumes a fully hadronic mechanism for the production of the diffuse γ-rays in the central part of the Galaxy. Models from full CR propagation in the Milky Way and including all production mechanisms, such as that described in ref. [94] and presented in section 3.2, produce neutrino fluxes that can be described in large parts of the energy range with a power-law behaviour.

A wide range of options can be explored with the observation from ANTARES. For this reason the signal flux is parametrised here as an unbroken power-law with spectral index Γ ranging from 2.0 to 2.7 in steps of 0.1.

The background from atmospheric events is given by atmospheric muons and neutrinos. The first component is described by the MUPAGE Monte Carlo sample described in §4.5.1. Atmospheric neutrinos events are weighted according to the conventional flux prescription of *Honda et al.* computations [132], together with the prompt component from *Enberg et al.* [136].

6.1.1 Choice of the signal and background regions

A detailed description of the diffuse γ-ray flux from the inner part of our Galaxy can be used for the definition of the signal region of the analysis. Fermi-LAT measurements show that most of the observed γ luminosity in the central region of the Milky Way comes from a narrow band in galactic latitude: the central few degrees basically contains 90% of the observed diffuse flux of γ-rays. As far as the galactic longitude is concerned, the observed diffuse flux extends to the whole Galactic Plane, though the largest abundance comes from the innermost 50 degrees.

The signal region must encompass most of the diffuse γ-ray flux, while being small enough to reduce the contribution from atmospheric background. In ref. [70] it is shown that the optimal size for such a region with the ANTARES telescope ranges from about 0.05 to 0.4 sr solid angle area. Smaller regions would be too small for the angular resolution of this kind of search – a point source search would be more accurate in this case. Larger regions would allow in the selected sample too many events from the atmospheric neutrino background, significantly reducing the significance of the measurement. Assuming that a cosmic signal described by an unbroken power law with spectral index $\Gamma = 2.4$, the best signal-to-noise ratio is found when a rectangular region is delimited by

$$|\ell| < 40° \quad |b| < 3° \tag{6.1}$$

in galactic longitude $|\ell|$ and latitude $|b|$. The corresponding solid angle is equal to 0.145 sr.

Off-zones are defined as fixed, non-overlapping regions in equatorial coordinates which have identical size and shape as the on-zone but no overlap with it. In local coordinates, off-zones have the same sidereal-day periodicity as the on-zone and span the same fraction of the sky, but with some fixed delay in time. Thus the detector has the same exposure to each of the off-zones and to the on-zone. In order to avoid possible superimposition with the Fermi bubbles, from

82
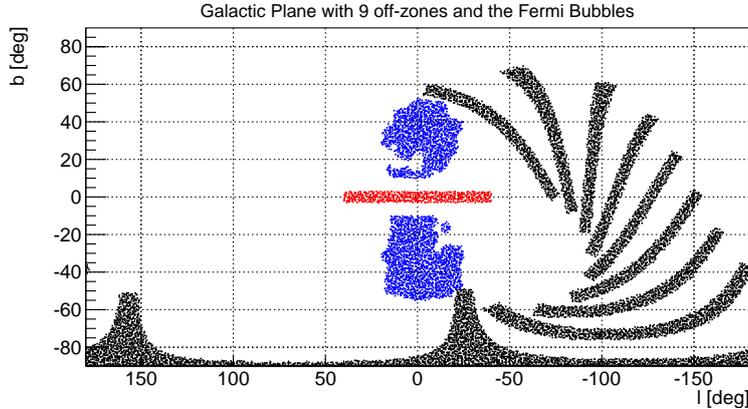
Figure 6.1: Signal (red dots) and background (black dots) regions representing the considered Galactic Plane region and off-zones of the analysis, see text for the definition. Also shown the shape of the Fermi bubbles (blue dots) as in ref. [148].

which a cosmic neutrino signal is expected in some models, the first and last off-zones have been shifted by 7h 12m and -5h 30m from the on-zone respectively. The shape of the Fermi bubbles as provided in ref. [148] has been used. As a consequence of this choice and because of the size of the signal region, a total number of 9 off-zones is defined. Signal and background regions, together with the assumed shape for the Fermi bubbles, are shown in galactic coordinates in figure 6.1.

6.2 Event selection

The analysed data set comprises events collected with the ANTARES neutrino telescope from January 2007 to December 2013. The livetime that has been analysed is equivalent to 1622 days of data acquisition.

Having defined the signal and background for the analysis and the considered data set, an optimal event selection must be defined, based on Monte Carlo simulations. This is necessary to suppress the atmospheric background, optimising the signal-to-noise ratio and consequently the sensitivity of the experiment. Data from the signal region are kept blinded until this selection is not completely defined. Off-zones can however be openly used to check the agreement between data and Monte Carlo, as well as the consistency of the background rates between different off-zones.

6.2.1 Model Rejection Factor minimisation

In order to properly define an optimal event selection for the rejection of atmospheric events maximising the sensitivity of the experiment, a Model Rejection Factor [149] minimization procedure is applied to obtain the best selection cut.

Let $\Phi(E)$ be the theoretical source flux, n_s the number of expected signal events, n_b the expected background and n_{obs} the number of events observed in

a hypothetical experiment. If the number of observed events is compatible with the background, the upper limit for the flux at 90% confidence level (C.L.) is:

$$\Phi(E)_{90\%} = \Phi(E)\frac{\mu_{90}(n_{\text{obs}}, n_b)}{n_s}, \tag{6.2}$$

where $\mu_{90}(n_{\text{obs}}, n_b)$ is the Feldman-Cousins upper limit [150].

The "average upper limit" that would be observed by an ensemble of hypothetical experiments with no true signal ($n_s = 0$) and expected background n_b can be computed. Taking into account all the possible fluctuations for the estimated background, weighted according to their Poisson probability of occurrence, the average upper limit is:

$$\bar{\mu}_{90}(n_b) = \sum_{n_{\text{obs}}=0}^{\infty} \mu_{90}(n_{\text{obs}}, n_b)\frac{n_b^{n_{\text{obs}}}}{n_{\text{obs}}!}e^{-n_b}. \tag{6.3}$$

The best upper limit is obtained with the best cut that minimises the Model Rejection Factor (MRF):

$$MRF = \frac{\bar{\mu}_{90}}{n_s} \tag{6.4}$$

and hence minimises the average upper limit flux

$$\bar{\Phi}(E)_{90\%} = \Phi(E)\frac{\bar{\mu}_{90}}{n_s} \tag{6.5}$$

or, equivalently, provides an estimate of the best sensitivity of the experiment.

6.2.2 Optimal cut selection

The event selection is done on the basis of the track quality parameter Λ, the angular error estimate β and the value of the reconstructed energy coming from an artificial neural network E_{ANN}. The first two parameters are useful for the rejection of atmospheric muons that are wrongly reconstructed as upward-going events, analogously to what is shown in section 5.2.1. In order to estimate the muon contamination for strict selection conditions, where the Monte Carlo simulation runs out of statistics, an extrapolation of the Λ distribution is performed, analogously to what is shown in figure 5.1, for each possible combination of the β and E_{ANN} selection cut.

Figures 6.2 and 6.3 show the MRF value for different event selection cut on the Λ and E_{ANN}: figure 6.2 refers to events with angular error estimate $\beta < 0.5°$, while figure 6.3 is for $\beta < 1°$. The search for an optimal cut is performed changing the signal spectral index from $\Gamma = 2$ to $\Gamma = 2.7$ in steps of 0.1. The optimal value for the selection cut as a function of the signal spectral index is reported in table 6.1.

It can be observed that the minima of the MRF distributions are quite broad and the choice of a close-to-optimal selection cut does not reduce dramatically the sensitivity. Analogously, given a certain signal spectral index, the optimal cut for a close spectral index lies in neighbouring or next-to-neighbouring bin of the $\Lambda - E_{\text{ANN}}$ plane. This translates to the opportunity of setting only one selection cut to be applied on data, without an excessive worsening of the sensitivity of the experiment. Considering that the most interesting spectral index for the

Γ	Λ	β	$\log_{10}(E_{ANN}/\text{GeV})$	Sensitivity
		$[deg]$		$[\text{GeV}^{-1}\,\text{s}^{-1}\,\text{cm}^{-2}\,\text{sr}^{-1}]$
2.0	-5.0	0.5	4.2	2.0×10^{-7}
2.1	-5.0	0.5	4.2	6.7×10^{-7}
2.2	-5.0	0.5	4.0	2.1×10^{-6}
2.3	-5.0	0.5	4.0	6.6×10^{-6}
2.4	-5.0	0.5	4.0	2.0×10^{-5}
2.5	-5.0	0.5	3.8	5.7×10^{-5}
2.6	-5.1	0.5	3.6	1.6×10^{-4}
2.7	-5.3	0.5	2.0	5.6×10^{-4}

Table 6.1: Dependence of the sensitivity obtained with the MRF procedure on the spectral index Γ when the best selection cut are applied in Λ, β and E_{ANN} for the analysis of cosmic neutrino fluxes from the Galactic Plane.

signal should be close to the observation coming from the IceCube experiment, the chosen selection cut is that for $\Gamma=2.4$. This selection cut is

$$\Lambda > -5.0 \quad \beta < 0.5° \quad E_{ANN} > 10 \text{ TeV}. \tag{6.6}$$

6.3 Results

After the unblinding of the entire data sample, 3.7 events are observed on average in the off-zone regions with energy $E_{ANN} > 10$ TeV. Two events are detected from the Galactic Plane region. The distributions of the number of selected events in the on-zone (black points) and off-zone (red histogram) regions as a function of the reconstructed energy are given in figure 6.4. The standard deviation of the variable $\log_{10}(E_{ANN}/E_{true})$, where E_{true} is the Monte Carlo true energy of the muon, is almost constant at ~ 0.4 over the considered energy range. The small under fluctuation of events with $E_{ANN} > 10$ TeV in the signal region is compensated by a similar over-fluctuation at lower energies.

A smaller number of events than the expected background is observed, and the Feldman and Cousins 90% c.l. upper bound [150] was computed. The corresponding flux is equal to $1.5 \cdot 10^{-5}\, E^{-2.4}\, \text{GeV}^{-1}\, \text{s}^{-1}\, \text{cm}^{-2}\, \text{sr}^{-1}$. Adopting the same conservative approach as for the limits from selected point-like sources [78] in the case of a under-fluctuation, the 90% c.l. upper limit on the signal flux is set to the value of the ANTARES sensitivity. One limit for each considered spectral index is obtained. As the procedure was optimised for $\Gamma =2.4$, the limit obtained for this value are the most restrictive.

The 90% c.l. upper limits (for one neutrino flavour) are shown in figure 6.5 for some values of Γ (horizontal black lines). For illustration, the one flavour neutrino flux from the considered region necessary to produce from 2 to 6 HESE is also reported as dashed lines (one for each considered spectral index). The curves are computed on the basis of the effective areas presented in ref. [67] according to the prescription of [70]. All fluxes above the horizontal black lines are excluded by our observations. For instance, a flux with spectral index $\Gamma = 2.5$ that produces 3 or more HESE in the signal region of $\Delta\Omega = 0.145$ sr is excluded by the analysed data.

(a) $\Gamma = 2.0$

(b) $\Gamma = 2.1$

(c) $\Gamma = 2.2$

(d) $\Gamma = 2.3$

(e) $\Gamma = 2.4$

(f) $\Gamma = 2.5$

(g) $\Gamma = 2.6$

(h) $\Gamma = 2.7$
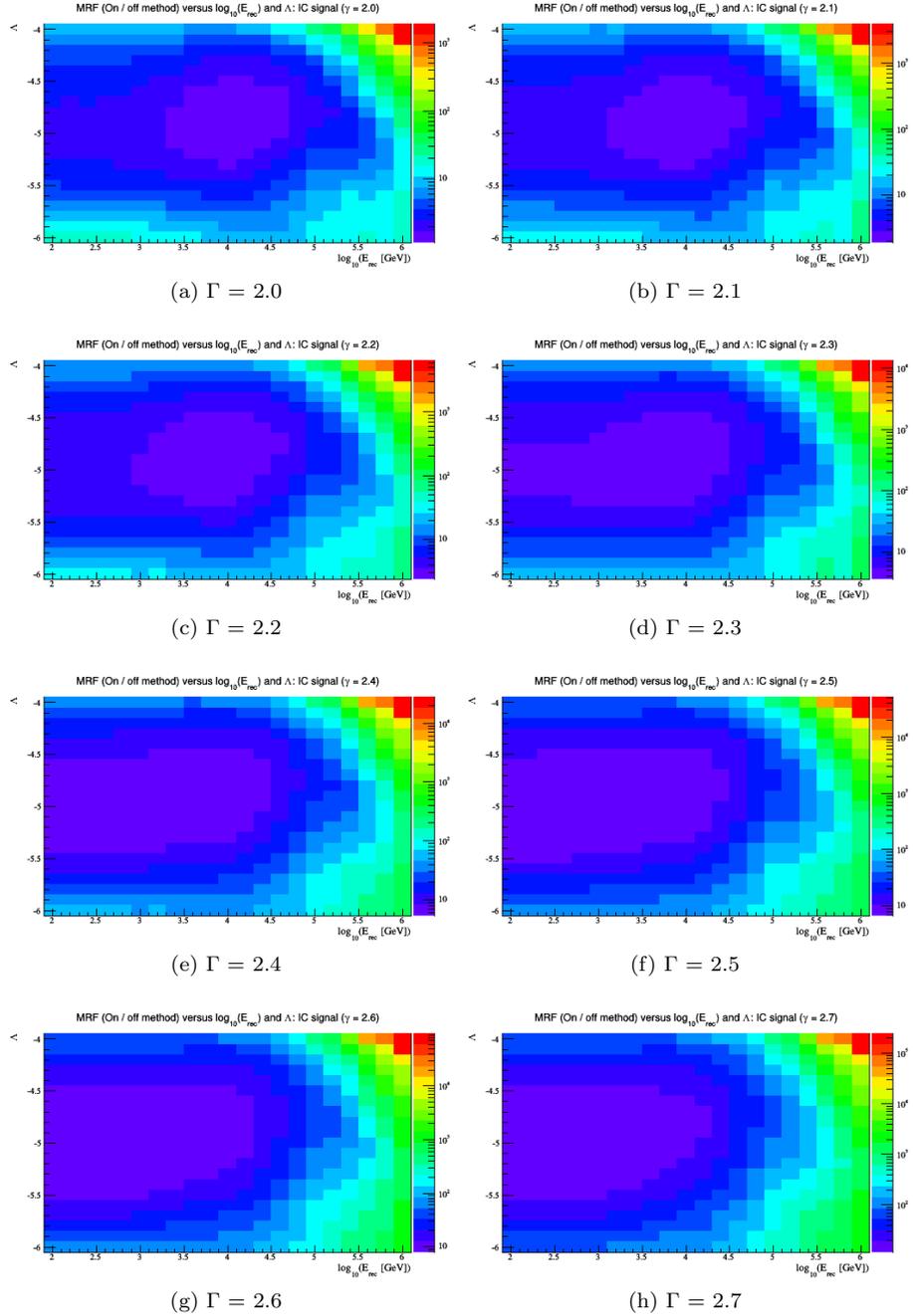
Figure 6.2: 2-dimensional Model Rejection Factor dependence on the Λ track quality parameter and the E_{ANN} reconstructed energy. Different spectral indexes are shown for $\beta < 0.5°$.

(a) $\Gamma = 2.0$

(b) $\Gamma = 2.1$

(c) $\Gamma = 2.2$

(d) $\Gamma = 2.3$

(e) $\Gamma = 2.4$

(f) $\Gamma = 2.5$

(g) $\Gamma = 2.6$

(h) $\Gamma = 2.7$
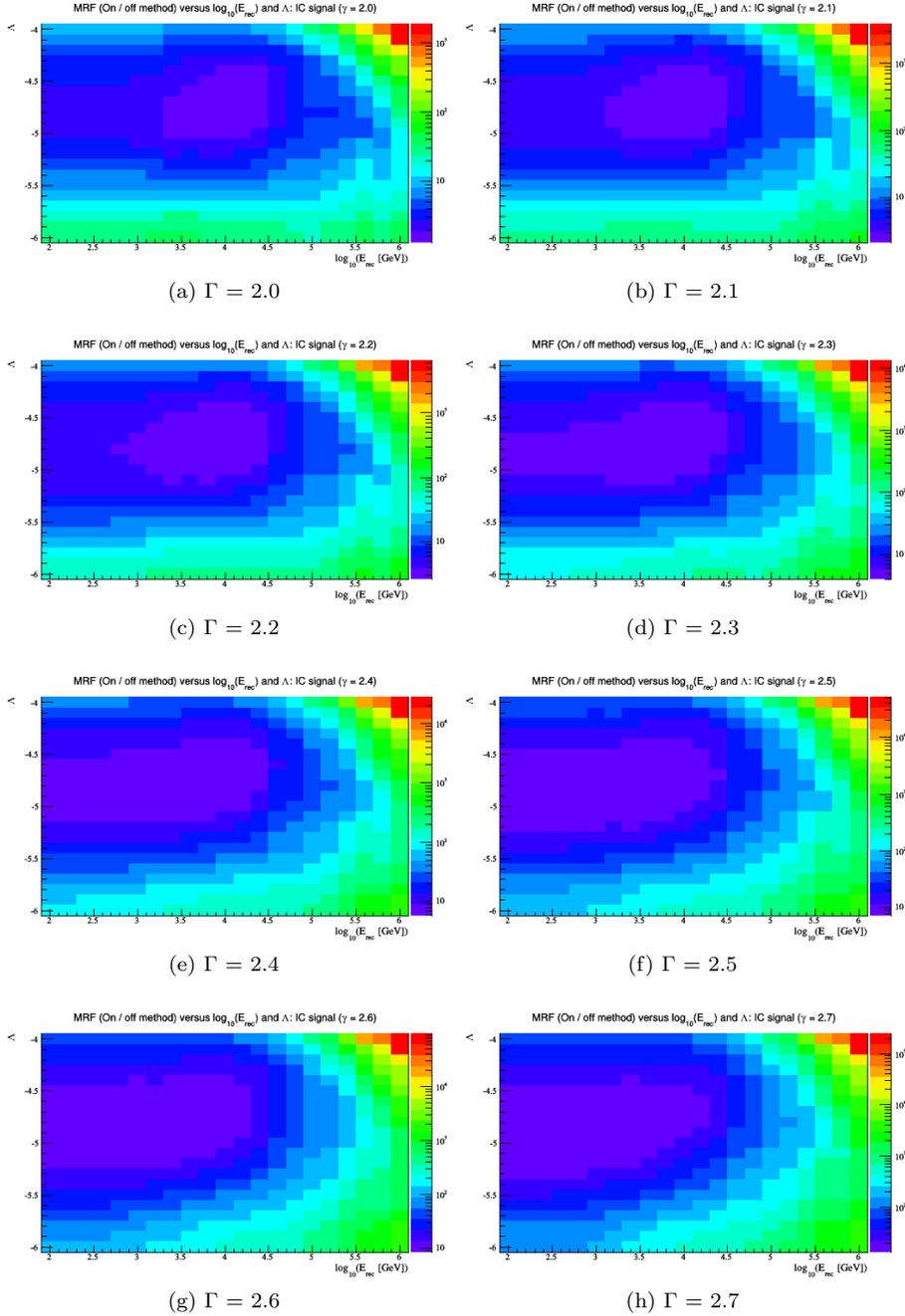
Figure 6.3: 2-dimensional Model Rejection Factor dependence on the Λ track quality parameter and the E_{ANN} reconstructed energy. Different spectral indexes are shown for $\beta < 0.5°$.

87
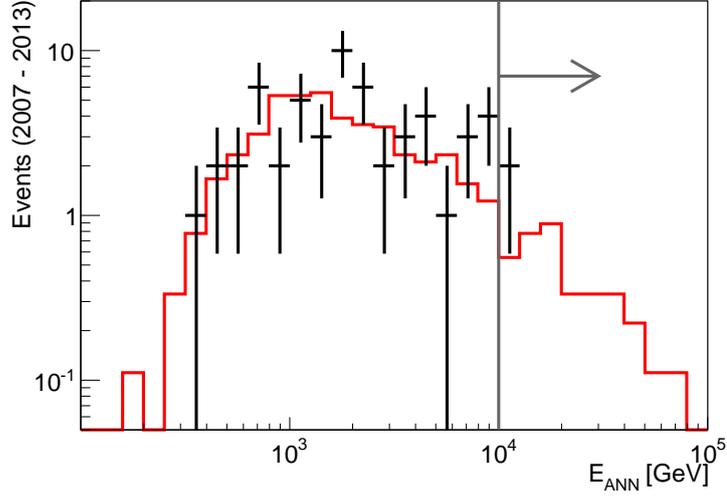
Figure 6.4: Distribution of the reconstructed energy E_{ANN} of upward-going muons in the Galactic Plane (black crosses) and off-zone regions. In the latter case, the distribution is normalized to the number of off-zones. The gray line shows the energy selection cut applied in the procedure.
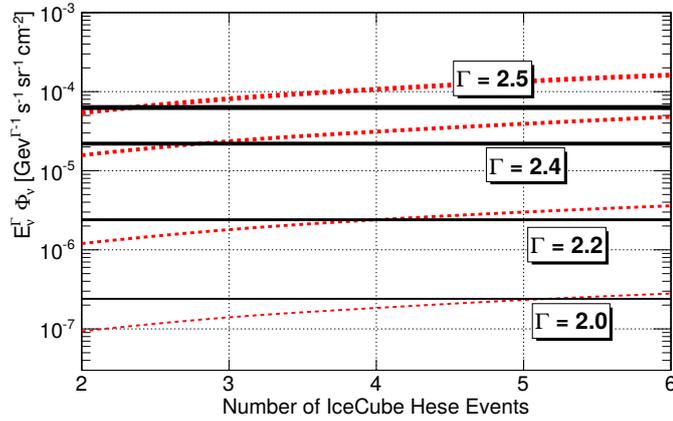
Figure 6.5: Upper limits derived from the null observation in the Galactic Plane region for different signal spectral indexes Γ. Selection cuts have been optimised for $\Gamma = 2.4$. The limits for different spectral index are thus derived with non-optimal criteria, though the difference is limited to a 10% in sensitivity. The expected flux producing from 2 to 6 IceCube HESE in the signal region is also represented by dashed lines.
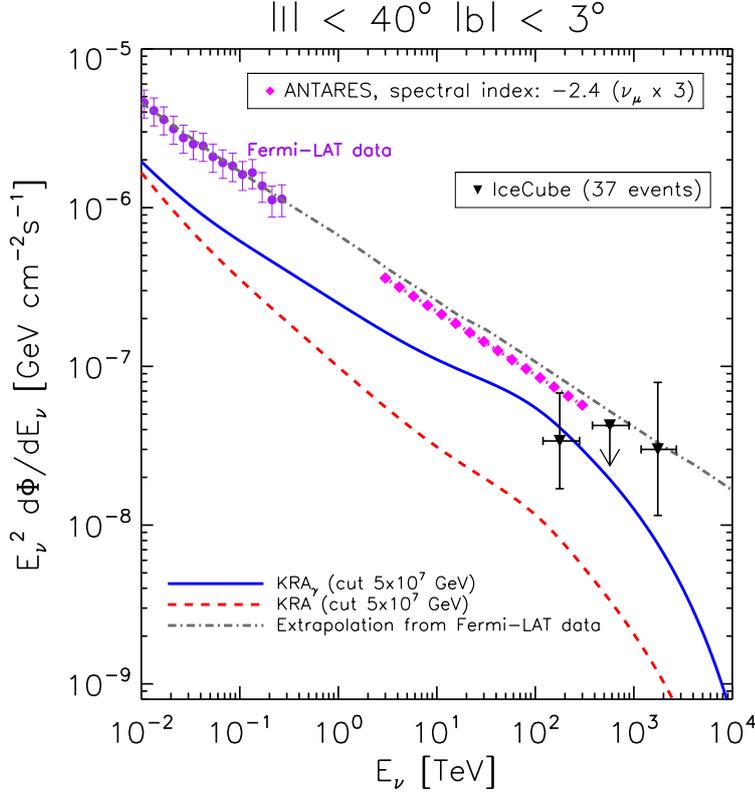
Figure 6.6: ANTARES upper limit (magenta dots) for this analysis compared to the expected neutrino flux (dot-dashed line) estrapolated from the Fermi-LAT diffuse γ flux up to IceCube energies [100] and to the neutrino expectations as computed in ref. [94] for the Galactic Plane region

Figure 6.6 shows the computed ANTARES 90% c.l. upper limit for the neutrino emission in the region $|\ell| < 40°$ and $|b| < 3°$ assuming a $\Gamma = 2.4$ neutrino flux. The purple full line is drawn for all neutrino flavours assuming flavour ratio 1:1:1. The expectations from some theoretical models are also represented in the figure. In particular, it should be mentioned that the simple extrapolation to the IceCube energies of the diffuse γ-ray flux measured by Fermi-LAT, assuming 100% hadronic origin, is excluded at 90% confidence level, if the $1:1:1$ flavor ratio is assumed.

More detailed models, that consider a harder CR spectrum in the inner Galaxy and are tuned to follow the hardening of the CR spectrum measured by PAMELA and AMS-02 [94] yield a neutrino flux (at 100 TeV) a factor of two to three lower, still reproducing the Fermi-LAT γ-ray diffuse flux (blue line denoted as KRA$_\gamma$ in figure 6.6). Models not including the CR hardening (curve labelled KRA) yield neutrino fluxes one order of magnitude smaller than that of the extrapolation from Fermi-LAT, shown as a dot-dashed line.

Chapter 7

Prospects for KM3NeT

The construction of the first building block of the KM3NeT/ARCA detector (§2.1.2) has started in December 2015. Once completed, it will be the largest neutrino experiment in the Northern hemisphere and the largest under-water neutrino telescope. The excellent angular resolution of the ARCA detector, with an instrumented volume of about one Gton, will allow for an unprecedented exploration of the neutrino sky searching for neutrinos coming from point-like (both galactic and extra-galactic) or extended regions of the sky, like the Galactic Plane. It will also look for a diffuse high energy neutrinos flux following the indication provided by the IceCube signal.

Studies on the sensitivity of the KM3NeT/ARCA detector – two building blocks corresponding to an instrumented volume of $1\,\mathrm{km}^3$ – to diffuse fluxes of cosmic neutrinos are presented in this chapter. In particular the work presented in sections 7.1.3 and 7.1.4 is completely origninal and have been published in the KM3NeT Letter of Intent [58].

7.1 All-sky searches

The IceCube Collaboration has observed cosmic neutrinos in various analyses §2.2, reporting an excess of high energy neutrinos over the atmospheric flux expectations. The observed flux is compatible with an isotropic distribution and equipartition in the three neutrino flavours as expected from neutrino oscillations in vacuum. Individual sources for this excess have not been identified, neither has the production mechanism for these high energy neutrinos been cleared. A study to evaluate the sensitivity of the full KM3NeT/ARCA detector has been performed. The one-flavour IceCube cosmic signal flux has been parametrised as:

$$E_\nu^2 \frac{d\Phi(E_\nu)}{dE_\nu} = 1.2 \cdot 10^{-8} e^{-E/3\,\mathrm{PeV}} \mathrm{GeV\ cm}^{-2}\ \mathrm{s}^{-1}\ \mathrm{sr}^{-1} \qquad (7.1)$$

even though different fits are possible. The results presented here do not depend strongly on the assumed signal flux.

Two topologies of events have been considered: track-like and shower-like events. The former is made of through-going muon tracks produced mainly by ν_μ CC interactions. The latter is made of cascades produced in all-flavour neutrino interactions creating electromagnetic and hadronic showers at the interaction

vertex. Two separate analyses have been completed to search for a cosmic spectrum analogous to eq. 7.1 using a step procedure for background rejection. The two strategies are described in section 7.1.1. Each of the two analysis strategies is described separately in the following sections and their combined sensitivity to a flavour-uniform diffuse flux is presented in section 7.1.4.

7.1.1 Search method

The first step of the analysis consists in the rejection of atmospheric backgrounds. The Model Rejection Factor or the Model Discovery Potential (MDP) maximisation procedure [151], have been used to identify the set of selection cuts in order to optimise analyses for the sensitivity of the detector. However this approach does not allow to properly take into account the spectral shape of the signal and background. Improvements are possible when a statistical method based on maximum likelihood methods is used. These methods are based on the Likelihood Ratio (LR) test:

$$LR = \log\left[\frac{P(data|H_{s+b})}{P(data|H_b)}\right] \tag{7.2}$$

where $P(data|H_i)$ is the probability that data can be explained by the hypothesis H_i, being b the background and s the signal.

Collected data consist of a number n of uncorrelated events, so that LR can be written as:

$$LR = \log\frac{\prod_{i=1}^{n}P(x_i|H_{s+b})}{\prod_{i=1}^{n}P(x_i|H_b)} = \sum_{i=1}^{n}\log\frac{P(x_i|H_{s+b})}{P(x_i|H_b)} \tag{7.3}$$

where each event x_i has a certain probability of being classified as signal-like with a certain quality parameter ρ and reconstructed energy E_{reco}. Knowing the 2D probability density functions for the signal and background hypotheses from simulation, eq. 7.3 becomes:

$$
\begin{aligned}
P(x_i|H_{s+b}) &= \frac{n_s}{n}\times P_s(\rho, E_{\text{reco}}) + \left(1 - \frac{n_s}{n}\right)\times P_b(\rho, E_{\text{reco}}) \\
P(x_i|H_b) &= P_b(\rho, E_{\text{reco}})
\end{aligned}
\tag{7.4}
$$

where P_b and P_s are the 2D PDFs for background and signal, n_s is the number of signal events and thus n_s/n and $(1\text{-}n_s/n)$ are the fraction of signal and background events. The likelihood ratio finally becomes:

$$LR = \sum_{i=1}^{n}\log\frac{\frac{n_s}{n}\times P_s(\rho, E_{\text{reco}}) + \left(1 - \frac{n_s}{n}\right)\times P_b(\rho, E_{\text{reco}})}{P_b(\rho, E_{\text{reco}})} \tag{7.5}$$

The maximum LR and the corresponding fitted number of signal events n_s is computed in an iterative procedure. This is firstly applied to the background only hypothesis, producing many pseudo-experiments and recording the $LR_b^{\max}$ distribution. The critical value $LR_{n\sigma}$ is computed so that, for example,

$$\int_{-\infty}^{-LR_{5\sigma}} LR_b^{\max} + \int_{LR_{5\sigma}}^{+\infty} LR_b^{\max} = 5.7\times 10^{-7}. \tag{7.6}$$

The procedure is then repeated adding N_s signal events and the integral of the resulting LR_s^{max} corresponds to the discovery power given by the observation of N_s events. If $N_{5\sigma}$ is the N_s giving a 50% discovery power at 5σ, then $n_{5\sigma}$ represents the number of events needed to have an observation with p-value corresponding to a 5σ discovery with 50% C.L.. Given a signal flux Φ_s and a mean number of signal events $\langle n_s \rangle$, the discovery flux is:

$$\Phi_d = \Phi_s \times \frac{n_d}{\langle n_s \rangle} \qquad (7.7)$$

7.1.2   Track analysis

The first step in the event selection for the track channel analysis is a cut on the reconstructed track direction to get rid of most of the atmospheric muons. According to the optimisation procedure a cut to events with reconstructed zenith angle $\theta_{zen} > 80°$ was chosen, thus including also events coming up from $10°$ above the horizon.

To improve the rejection of the background mainly due to wrongly reconstructed muon tracks and to atmospheric neutrinos the MDP maximisation is performed selecting well-reconstructed tracks and removing less energetic events likely due to atmospheric neutrinos. The two reconstruction parameters correlated with the reconstruction quality and the neutrino energy are the Λ and N_{hit} parameters, described in ref. [152]. The cumulative distributions for the Λ quality parameter and for the number of hits are shown in figure 7.1. $\Lambda >$ -5.8 and $N_{hit} > 539$ proved to be optimal for one year of observation time. The angular and energy resolution for the selected sample is $\sim 0.2°$ and ~ 0.27 in the logarithm of the energy, respectively, as shown in figure 7.2.

After one year of observation time, the final selected event sample contains 5.4 events from background and 7.6 events according to the diffuse neutrino flux of eq. 7.1. With these event rates, the IceCube signal flux can be observed with 3.5σ significance after one year of KM3NeT/ARCA data taking.

The sensitivity can be increased by using a statistical method based on the maximization of a likelihood function, rather than using a simple cut. This has been performed as described in 7.1.1, on a sample of preselected neutrino events with $\theta_{zen} > 80°$ and $\Lambda >$ -5.8. The likelihood ratio function maximisation uses the energy estimation given by the number of hits as probability density function. The resulting significance is shown figure 7.8 as a function of the number of observation years and reaches about 4σ after one year with a 50% chance of detection.

7.1.3   Showers

An event selection procedure based on three consecutive cuts has been used in the shower analysis to discriminate between signal and background events. At the first selection level, only contained events are kept. Because of Earth absorption, part of the neutrino signal can be absorbed while passing through the Earth. For this reason an analysis which can look for events coming from both hemispheres enhances the sensitivity of the experiment. As the background from downward-going is composed mostly of atmospheric muons, a strong rejection of this background is necessary.

(a) Λ
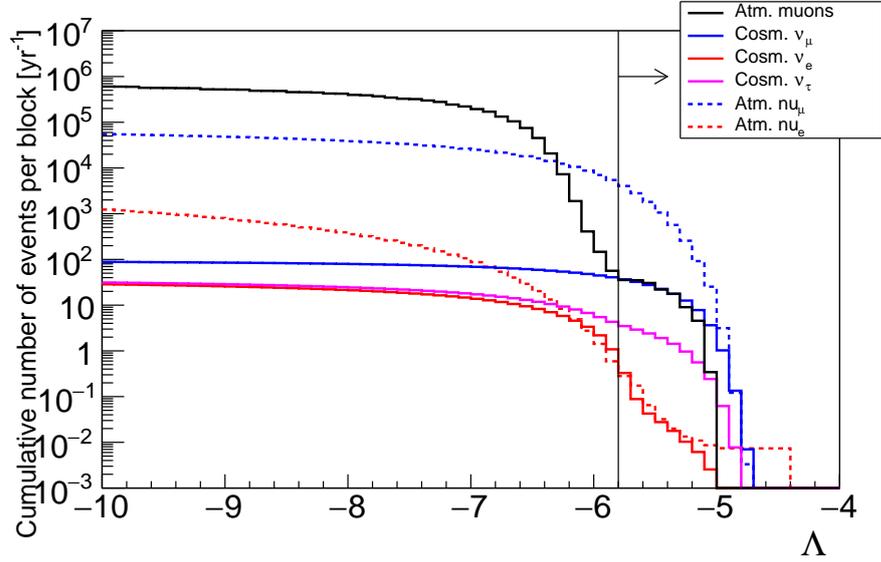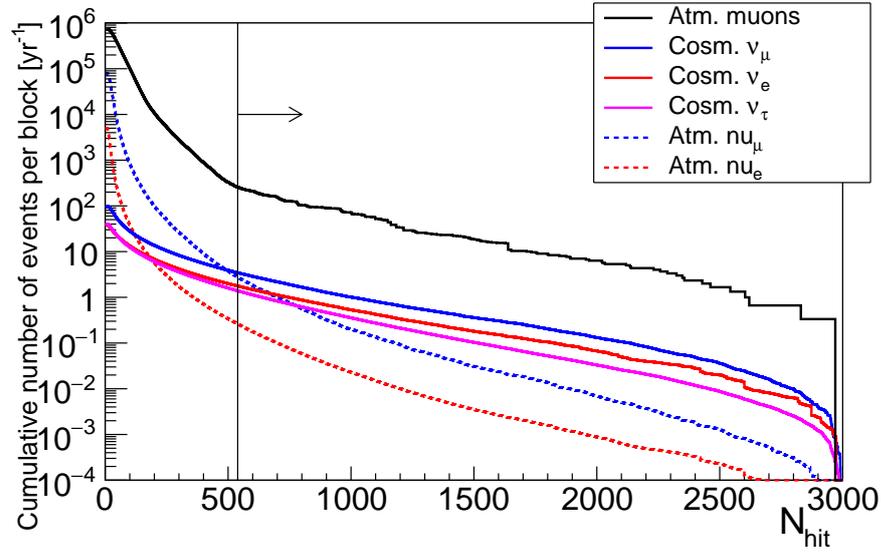
(b) N_{hit}

Figure 7.1: Cumulative distribution for the Λ (top panel) and N_{hit} parameters from the track reconstruction algorithm developed for KM3NeT/ARCA. Event rates for one year of operation of the ARCA building block are reported; atmospheric muons are shown in red, while atmospheric neutrinos in black.

(a) Energy resolution


(b) Angular resolution
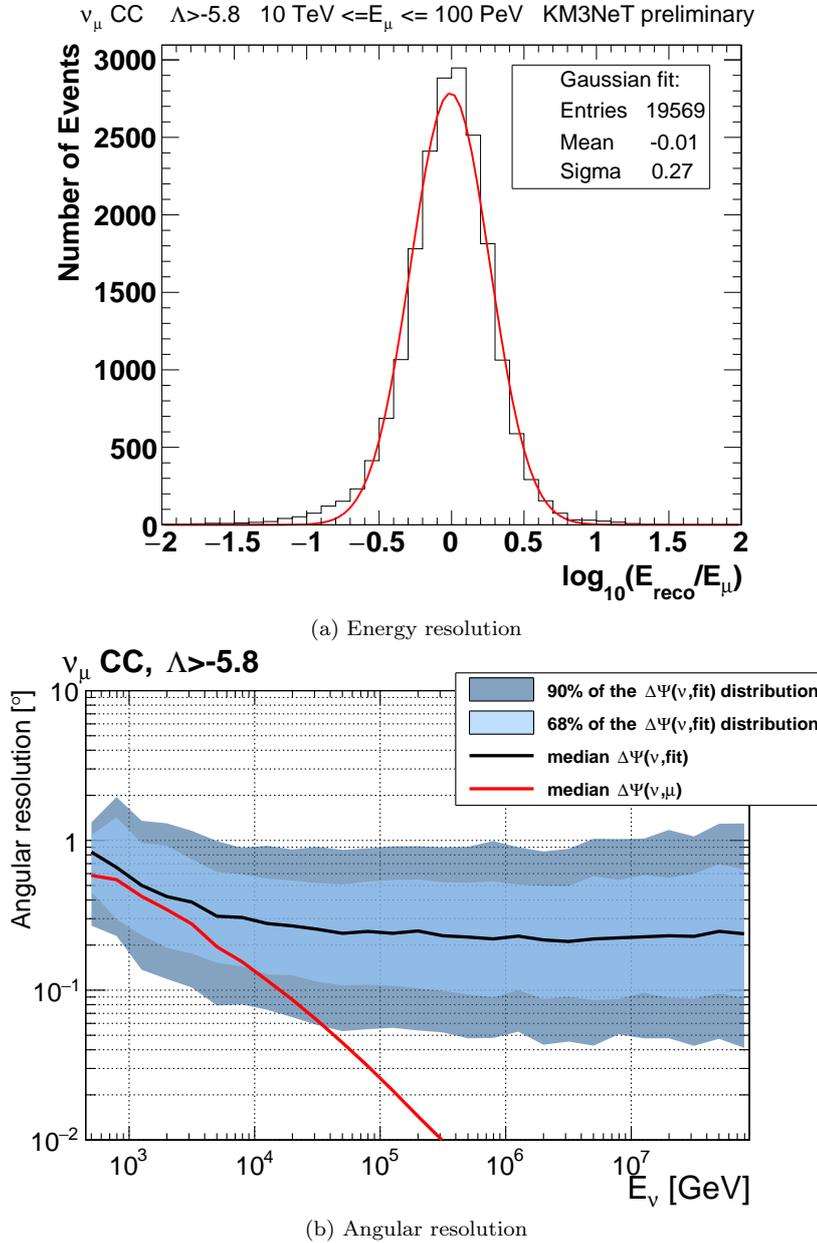
Figure 7.2: Performances of the track reconstruction algorithm for ν_μ CC events after the final selection cut. Top plot shows the difference between the reconstructed and the true muon energy for events above 10 TeV passing the Λ quality cut; bottom plots report angular resolution, showing the 1 and 2σ quantiles as the dark and light blue bands.
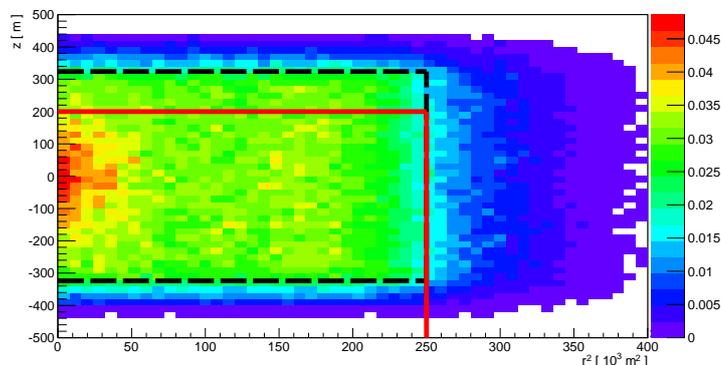
(a) Shower events
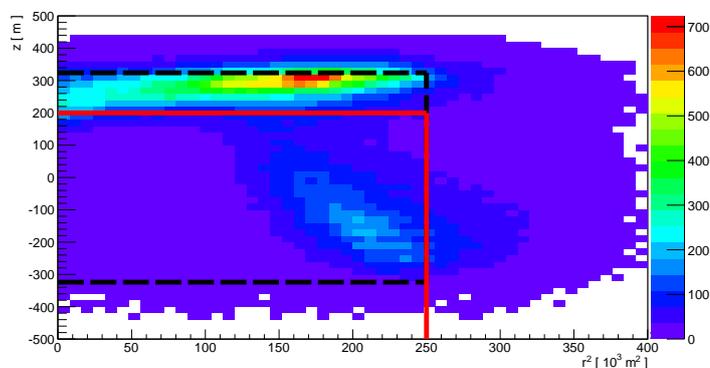
(b) Atmospheric muon, 50 TeV sample

Figure 7.3: Output of the vertex reconstruction for signal cosmic neutrinos (top) and background atmospheric muons (bottom – high threshold sample). The plots here show the z and r^2 coordinates of the reconstructed vertex for neutrino events and a sort of pseudo-vertex for atmospheric muons. The black dashed line represents the instrumented volume of a KM3NeT block, while the region inside the red solid line is the containment requirement for the analysis.

Atmospheric muons are passing through tracks and most of the Cherenkov light coming from the event produces hits on the outermost PMTs of the apparatus. As a result, in this cases, the cascade reconstruction algorithm usually reconstructs a shower vertex outside the instrumented volume. On the contrary neutrinos interacting inside the detector have their vertex properly reconstructed and contained events can be identified, as shown in figure 7.3. A cut on the vertical coordinate z and on the radial distance R of the reconstructed vertices to the detector centre rejects a large part of the background. The applied selection cut is $R < 500\,\mathrm{m}$ and $z < 200\,\mathrm{m}$. This cut reduces the detector geometrical volume by about 20% while decreasing the number of atmospheric muons by more than one order of magnitude.

The sum of the time over threshold (ToT) of the hits causally connected to the reconstructed vertex is related to the energy of the events and can be
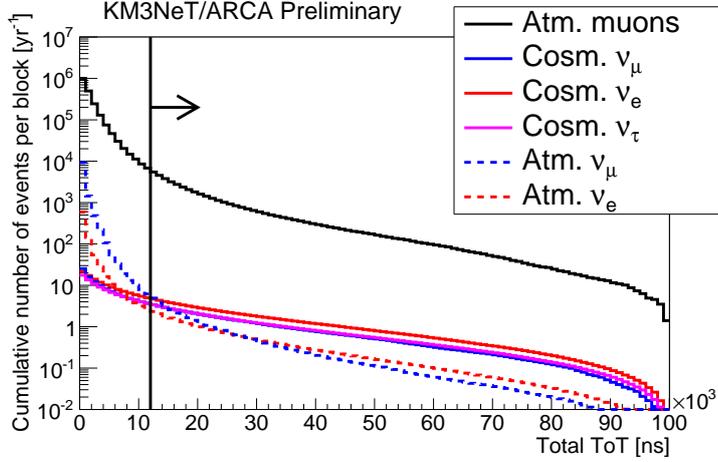
Figure 7.4: Cumulative total Time over Threshold distribution for events passing the containment requirement, colour code in the legend. The low threshold simulations runs out of statistics quite early, but the decrease in the shape of the distribution is strong enough to consider the cut at $12\,\mu$s safe. Different shapes for track and shower neutrinos can be explained by the different hit distribution in the detector with respect to the fitted vertex.

used to improve the rejection of background atmospheric events, both muons and neutrinos. The ToT is measured for each PMT and is a measure of the collected charge. Events with large deposited charge are more likely to be high in energy and consequently of cosmic origin. In addition, track-like events have less selected hits and thus the sum runs over fewer pulses and the total ToT is smaller with respect to that of cascades. This cut rejects a large number of low-energy atmospheric muons and also a large part of the atmospheric neutrino background from ν_μ CC events, dominant at lower energies. Figure 7.4 shows total ToT for the different event types (cumulative distribution) and the action of this selection cut.

The final step to isolate the signal from the remaining background uses a machine-learning algorithm based on the boosted decision tree (BDT) from the ROOT TMVA package [154]. As input for the BDT training, several quality parameters from the available shower and track reconstruction algorithms are used and its output is shown in figure 7.5. The output of the BDT is used together with the reconstructed shower energy $E_{\rm rec}$ to separate the signal from both the remaining atmospheric neutrino and muon backgrounds. The optimisation procedure is done using the MRF procedure already described and the result of the procedure are presented in figure 7.6.

After the final selection cut estimated with the MRF procedure, 16.1 signal and 8.4 background events are expected in one year of the ARCA detector operation. The mean angular and energy resolutions for these events are roughly $1.5°$ and 10%, respectively at $100\,$TeV as shown in figure 7.7. With these event rates in the shower channel a 5σ discovery of the assumed IceCube flux can be achieved after 1.3 years of ARCA data taking with 50% probability. A further improvement of this result is reached by applying the maximum
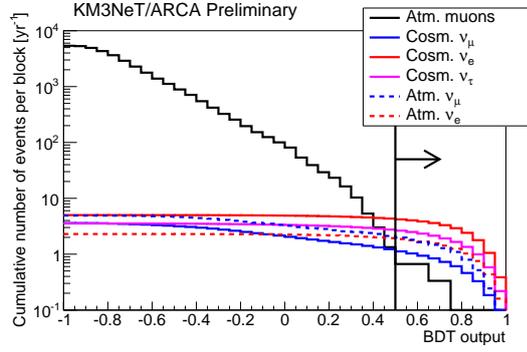
(a) Event flavour
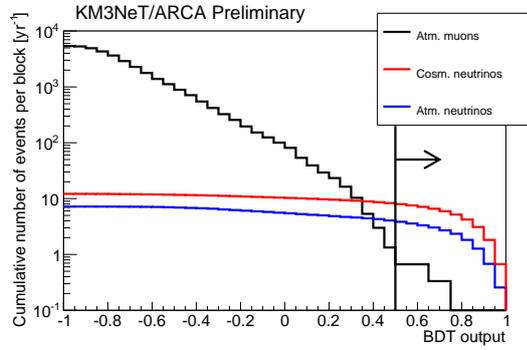
(b) Event type

Figure 7.5: Cumulative distribution of the output of the Boosted Decision Tree application on all events; upper plot showing the contribution of each event type of event (colour code as in the legend). Bottom plot shows the sum of all atmospheric and cosmic contributions together. BDT output values close to 1 mean "shower-like" event, -1 for "track-like" events.
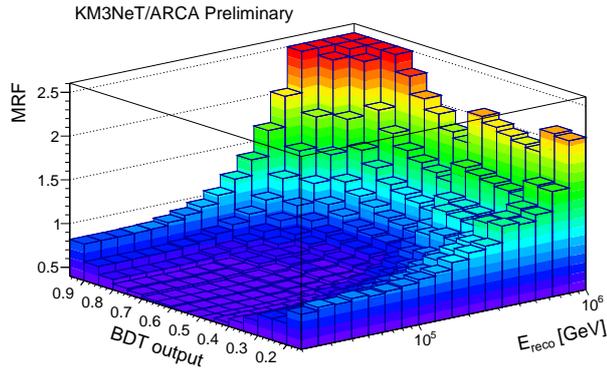

Figure 7.6: Model rejection factor distribution as a function of the reconstructed energy and of the BDT output. The position of the minimum can be clearly seen, at BDT = 0.50 and $E_{reco} = 10^{4.7}$ GeV.
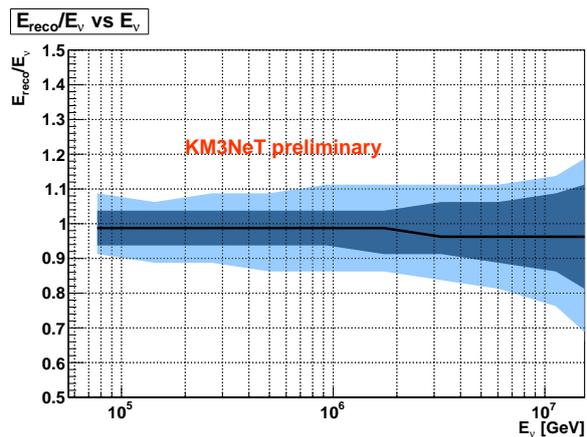
(a) Energy resolution
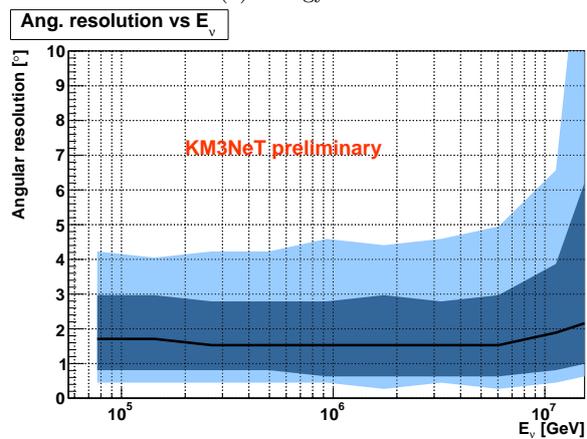
(b) Angular resolution

Figure 7.7: Performances of the shower reconstruction algorithm ν_e CC events after the final selection cut. Top plot is for the median energy resolution, bottom for the median angular resolution; the 2 bands show the 1 and 2σ quantiles.

likelihood method described in §7.1.2. The signal and background PDFs are two-dimensional functions of the reconstructed shower energy, E_rec, and of the BDT output. The resulting significance as a function of the observation years is shown in figure 7.8.

7.1.4   Combined search

As both the track and shower analyses have a strong bias in efficiency towards one particular event topology, a further analysis strategy has been developed to incorporate the results from both searches. The two analyses are indeed almost independent, as the overlap between the final event samples is limited to less than 2% of the surviving events. In order to develop an all-sky analysis with tracks and showers, the two hemispheres are treated separately, using the reconstructed zenith angle from the track reconstruction algorithm.

For downward-going events, where the atmospheric background is extremely high, only contained shower events are considered since muon-induced neutrinos would be completely covered by atmospheric muons. The selection for these events is analogous to that of the usual cascade analysis. For upward-going events, preliminary cuts are used to reject part of the atmospheric muons that are wrongly reconstructed as upward-going, based on both the track and cascade reconstruction quality parameters; then a BDT multivariate technique is used to provide a further rejection of these events. This BDT uses parameters coming from both the track and shower reconstruction algorithms and is optimised for the rejection of atmospheric muons. Its output is used together with the shower energy estimation in the same maximum likelihood approach described before.

The result of this combined analysis is equivalent to the combination of the two individual results from the track and shower analyses. A 4.8σ significance is obtained in 0.5 years of observation time (figure 7.8).

7.2   Neutrinos from the Galactic Plane

The search for neutrino fluxes from the Galactic Plane with ANTARES data, described in chapter 6, has shown that an under-water neutrino telescope in the Northern hemisphere can probe neutrino fluxes from CR propagation in the Galaxy. The upper limits presented in section 6.3 is already competing with the expectations from optimistic models such as that of ref. [100]. The ARCA detector, with an instrumented volume 20 times large than ANTARES, can provide a deep insight on this flux, possibly testing neutrino production models and CR propagation properties.

In order to study the expected sensitivity of the ARCA neutrino telescope, track-like events have been analysed. The neutrino flux from [94] is used as benchmark model for this computation. A rectangular region of the sky encompassed by $|\ell| < 30°$ and $|b| < 4°$ is taken into account for the ARCA analysis. This region of the sky is visible to the ARCA detector for 77% of its observation time when considering events up to 10° above the horizon. In this part of the sky the one-flavour neutrino flux computed by the authors of [94],
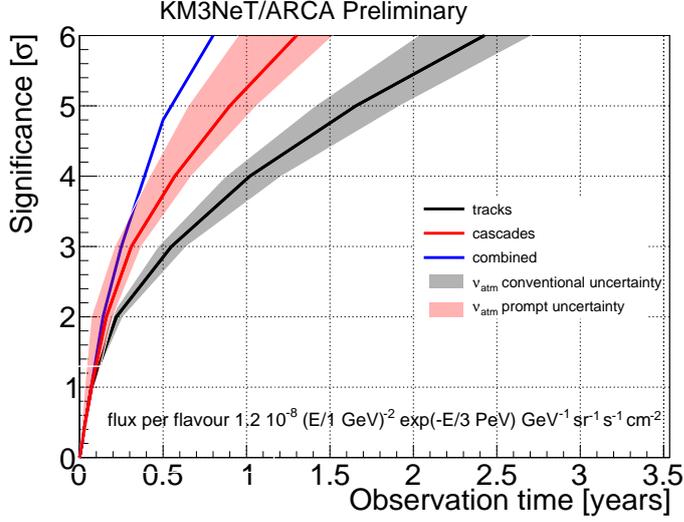
Figure 7.8: Discovery potential to the flux of eq. 7.1 for ARCA analyses. The black line shows the result from the analysis of track-like events, the red line that of the cascade channel and the blue line the combined result. Shaded areas provide a graphical estimation of systematic effects on the significance of the discovery to the referenc flux.

described in section 3.2.2 and shown in figure 3.5 can be parametrised as:

$$\frac{d\Phi}{dE_\nu} = 5 \times 10^{-6} \left(\frac{E_\nu}{1 \text{ GeV}} \right)^{-2.3} \times \exp \left(\sqrt{\frac{E_\nu}{1 \text{ PeV}}} \right) \text{ [GeV s sr cm}^2]^{-1}. \quad (7.8)$$

Events reconstructed with the track reconstruction algorithm with $\theta_{\text{rec}} >$ 80° have been selected at first. Analogously to the all-sky search, the MDP optimisation procedure has been used for the determination of the optimal selection cut on the Λ track quality parameter and N_{hit} energy estimator. The optimal cut that is found in the procedure is $\Lambda >$-5.8 and $N_{\text{hit}} >$181. As a result of this selection cut, 2.8 background and 3.4 signal events are expected for one year of operation of the ARCA detector from this region of the sky with the assumed flux of eq. 7.8.

Additionally, the maximum likelihood fitting procedure already explained above is used to estimate the discovery potential of the experiment. The 3σ and 5σ discovery flux as a function of the acquisition time with the complete ARCA detector are shown in figure 7.9, top panel. Within one and a half years of operation, the ARCA detector will be able to provide a discovery at 3σ significance (with 50% chance discovery) for the reference flux. Within 5 years of operation the significance would reach 5σ. The significance of the observation of the reference flux as a function of the acquisition time is given in figure 7.9, bottom panel.
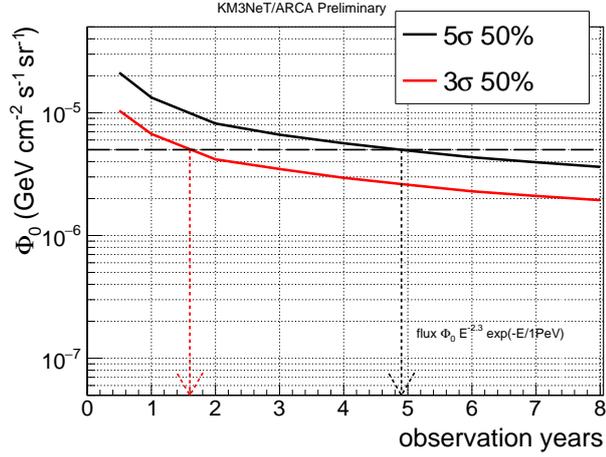
(a) Discovery potential
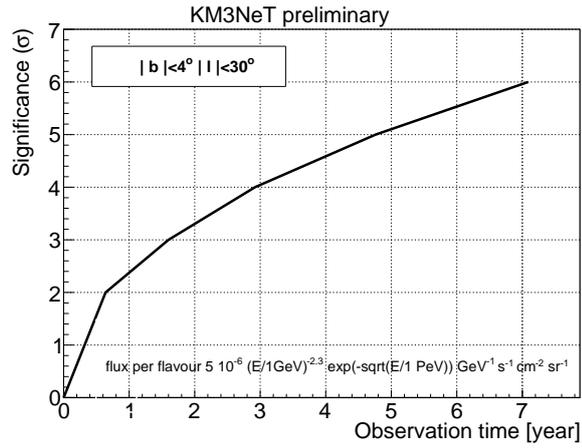
(b) Significance

Figure 7.9: Top panel: discovery flux at 3 (red line) and 5σ (black line), with 50% chance probability for the ARCA detector as a function of the acquisition time for the flux of equation 7.8. The dashed horizontal line shows the normalisation level of the flux. The red and black arrows report the time at which the discovery flux becomes lower than the normalisation of the reference flux. Bottom panel: significance of the discovery as a function of the acquisition time with the complete ARCA detector for the same reference flux.

Conclusions

The ANTARES telescope was completed in May 2008 and has taken data continuously since then; it is made of 12 lines anchored on the sea-bed, equipped with 885 PMTs. The main aim of the ANTARES Collaboration is the study of neutrino-emitting astrophysical objects, like AGN, GRB, and supernova remnants. The work presented in this thesis uses all data collected by the ANTARES neutrino telescope from the beginning of 2007 to the end of 2013.

Since 2012, the existence of cosmic high energy neutrinos has been estabilished by the IceCube Collaboration with high significance. The ANTARES detector represents a complementary instrument of discovery with respect to the IceCube neutrino telescope and it has already constrained the possible origin of part of this signal from point-like neutrino source in the central region of the Milky Way.

The search for a region of enhanced neutrino emission in the Southern sky which could explain part of the IceCube cosmic signal is presented in this thesis. The background from atmospheric muons is rejected by selecting upward-going neutrino-induced tracks. Though looking for upward-going reconstructed tracks should select only events due to neutrino interaction, a large number of wrongly reconstructed atmospheric muons survives this selection. The quality parameters of the track reconstruction algorithm are used to reject this background. The surviving background due to atmospheric neutrinos has been studied in details and the measurement of its energy spectrum is also presented in this work. This background can be rejected, on a statistical basis, selecting high energy events.

An enhanced neutrino emission is expected from the Galactic Plane as a result of the interaction of primary cosmic rays confined within the Milky Way. High energy events coming from the central part of the Galactic Plane are selected and the rate from a signal region encompassing the possible emission are is compared to what is observed in background regions for which the detector has the same exposure. This allow to limit systematics and uncertainties due to Monte Carlo simulations.

The optimal cut for background rejection is selected using a Model Rejection Factor minimisation procedure to scan a 3-dimensional space in the track quality parameter, the angular error estimate and the reconstructed energy of the event. The resulting sensitivity is:

$$E^{-2.4} \frac{d\Phi}{dE} = 2.0 \times 10^{-5} \text{ GeV}^{-1} \text{ s}^{-1} \text{ cm}^{-2} \text{ sr}^{-1} \tag{7.9}$$

using the Feldman-Cousins upper limit estimation. The observation of data from the signal region provides an under-fluctuation with respect to the background estimation from off-source regions. This conservatively corresponds to an upper limit equal to the sensitivity of the experiment.

The upper limit obtained in the analysis allows to constrain a fully hadronic explanation of the observed γ-ray flux from the Fermi-LAT satellite experiment for the Galactic Plane. This upper limits also allows the rejection of any model for the neutrino emission from the Galactic Plane which would produce more than 3 of the observed IceCube cosmic neutrino candidates. Theoretical models for neutrino production in the Galactic Plane from cosmic ray propagation cannot still be excluded, though the upper limit presented in this work is the most stringent ever obtained.

The further extension of the data sample up to the end of 2016, together with the addition of events reconstructed in the cascade channel can provide a further improvement of the measured limit. Finally the next generation neutrino telescope KM3NeT/ARCA being built in the Mediterranean Sea, with an instrumented volume 20 times larger than ANTARES, will allow for a deep insight on cosmic neutrinos, both for all-sky searches, for point-like source and for extended regions of neutrino emission, starting to prove the actual sources of cosmic neutrinos.

Bibliography

[1] V.F. Hess, Phys. Zeit. **13**: 1084, 1912.

[2] B. Rossi, Physical Review **36** (3): 606, 1930.

[3] T.H. Johnson, Physical Review **43** (10): 834-835, 1933.

[4] L. Alvarez and A.H. Compton, Physical Review **43** (10): 835-836, 1933.

[5] B. Rossi, Physical Review **45** (3): 212-214, 1934.

[6] C.D. Anderson, Phys. Rev. **43**: 491, 1933.

[7] S.H. Neddermeyer and C.D. Anderson, Phys. Rev. **51**: 884, 1937.

[8] C.M.G. Lattes, H. Muirhead, G. Occhialini and C.F. Powell, Nature **159**: 694, 1947.

[9] M. Longair, *High Energy Astrophysics*, Cambridge University Press, 1992.

[10] J.R. Hörandel, arXiv:1212.0739, 2012.

[11] A.M. Hillas, arXiv:astro-ph/0607109, 2006.

[12] J.R. Hörandel, Astrop. Phys. **21**: 241-265, 2004.

[13] J. Blümer, R. Engel and J.R. Hörandel, Prog. Part. Nucl. Phys. **63**: 293, 2009.

[14] R. Aloisio, V. Berezinsky and A. Gazizov, Astrop. Phys. **39-40**: 129-143, 2012.

[15] K. Greisen et al., Phys. Rev. Lett. **16**: 748, 1966.

[16] G.T. Zatsepin and V.A. Kuz'min, JETP Lett. **4**: 78, 1966.

[17] M. Takeda et al., Phys. Rev. Letters **81**: 1163-1166, 1998.

[18] R. Abbasi et al., Phys. Rev. Lett. **100** (10): 101101, 2008.

[19] J. Abraham et al., Phys. Rev. Lett. **101** (6): 061101-1-061107-7, 2008.

[20] E. Fermi, Phys. Rev. **75**: 1169, 1949.

[21] E. Fermi, Astroph. J. **119**: 1, 1954.

[22] M. Spurio, *Particle and Astrophysics. A Multi-Messenger Approach*, Springer, ISBN 978-3-319-08050-5, 2014.

[23] R. Antonucci, Annual Reviews in Astronomy and Astrophysics **31** (1): 473-521, 1993.

[24] P. Urry and P. Padovani, Publications of the Astronomical Society of the Pacific **107**: 803-845, 1995.

[25] P. Abreu et al., Astrop. Phys. **34**: 314-326, 2010.

[26] J.D. Jackson, *Classical Electrodinamics (3rd ed.)*, John Wiley & Sons, ISBN 978-0-30932-1, 1998.

[27] A.A. Abdo et al., Science **327** (5969): 1103-1106, 2010.

[28] M. Ackermann et al., ApJ **750**: 3, 2012.

[29] Y.Q. Guo, H.B. Hu and Z. Tian, arXiv:1412.8590, 2014.

[30] F. Vissani, Astrop. Phys. **26**: 310-313, 2006.

[31] C. Stegmann et al., Astrophysics and Space Science **309**: 429, 2007.

[32] E. Waxman and J. Bahcall, Phys. Rev. D **59**: 023002, 1998.

[33] E. Waxman and J. Bahcall, Phys. Rev. D **64**: 023002, 2001.

[34] A. Loeb and E. Waxman, JCAP **05**: 003, 2006.

[35] T.A. Thompson et al., Astrophys. J. **645**: 186-198, 2006.

[36] M. Rowan-Robinson, Astrophys. J. **549**:745-758, 2001

[37] A. Ptak et al., Astrophys. J. **592**: 782-803, 2003.

[38] G. Ingelman and M. Thunman, arXiv:hep-ph/9604286, 1996.

[39] J. Candia and E. Roulet, JCAP **09**: 005, 2003.

[40] J. Candia, JCAP **11**: 002, 2005.

[41] E. Visser, PhD Thesis, University of Leiden, 2015.

[42] J. Pumplin et al., JHEP **07**: 012, 2002.

[43] T. Chiarusi and M. Spurio, Eur. Phys. J. C **65**: 649-701, 2010.

[44] P. Lipari and T. Stanev, Phys. Rev. D **44**: 3534, 1991.

[45] M.A. Markov, Proceedings Int. Conf. on High Energy Physics, p. 183, Univ. of Rochester, 1960.

[46] G. Mie, Annalen der Physik **330**: 377, 1908.

[47] M.G. Aartsen et al., Nucl. Intrum. and Meth. in Phys. Res. A **711**: 73, 2013.

[48] http://www.phys.hawaii.edu/ dumand/

[49] I.A. Belolaptikov et al, Astrop. Phys. **7** (3): 263-282, 1997.

[50] V. Aynutdinov et al., Astrop.Phys. **25**: 140-150, 2006.

[51] A.V. Avrorin et al., Intruments and Experimental Techniques **54** (5): 649-659, 2011.

[52] http://antares.in2p3.fr/.

[53] T. Feder, Physics Today **55** (10): 20, 2002.

[54] A. Capone et al., Nucl. Inst. and Meth. in Phys. Res. A **602**: 47-53, 2009.

[55] S. Aiello et al., Astrop. Phys **66**: 1-7, 2015.

[56] G. Riccobene et al., Astrop. Phys. **27**: 1-9, 2007.

[57] T Chiarusi et al., JINST **9**: C03045, 2014.

[58] S. Adrián-Martínez et al., *Letter of Intent for KM3NeT 2.0*, arXiv:1601.07459 , 2016.

[59] S. Biagi et al., Proceedings of the 34th ICRC, The Hague, Netherlands, 2015.

[60] P. Piattelli et al., Proceedings of the 34th ICRC, The Hague, Netherlands, 2015.

[61] J. Brünner et al., Proceedings of the 34th ICRC, The Hague, Netherlands, 2015.

[62] A. Creusot et al., Proceedings of the 34th ICRC, The Hague, Netherlands, 2015.

[63] R. Bruijn et al., Proceedings of the 34th ICRC, The Hague, Netherlands, 2015.

[64] F. Halzen, Eur. Phys. J. C **46**: 669-687, 2006.

[65] A. Karle et al., Proceedings of the 31st ICRC, Lodz, Poland, 2009.

[66] M.G. Aartsen et al., Phys. Rev. Lett. **111**: 021103, 2013.

[67] M.G. Aartsen et al., Science **342**: 1242856, 2013.

[68] M.G. Aartsen et al., Phys. Rev. Lett. **113**: 101101, 2014.

[69] C. Kopper and N. Kurahashi Neilson et al., Proceedings of the 34th ICRC, The Hague, Netherlands, 2015.

[70] M. Spurio, Phys. Rev. D **90**: 103004, 2014.

[71] M.G. Aartsen et al., Phys. Rev. D **91**: 022001, 2015.

[72] M.G. Aartsen et al., Phys. Rev. Lett. **114**: 171102, 2015.

[73] A. Palladino et al., arXiv:1510.05921v1, 2015.

[74] M.G. Aartsen et al., Astrophys. J. **796**: 2, 2014.

[75] E. Waxman and J. Bahcall, Phys.Rev.Lett. **78**: 2292, 1997.

[76] K. Mannheim, R. Protheroe, and J.P. Rachen, Phys. Rev. D **63**: 023003, 2001.

[77] S.R. Kelner, F.A. Aharonian and V.V. Bugayov, Phys. Rev. D **74** (3): 034018, 2006.

[78] S. Adrián-Martínez et al., ApJ **786**: L5, 2014.

[79] A. Neronov and D. Semikoz, Astrop. Phys. **75**: 60-63, 2016.

[80] M.G. Aartsen et al., ApJ **805**: L5, 2015.

[81] S. Adrián-Martínez et al., A&A **576**: L8, 2015.

[82] Y. Bai et al., Phys. Rev. D **90**: 063012, 2014.

[83] E.P. Hubble, ApJ **64**: 321-369, 1926.

[84] M.H. Jones and R.J.A. Lambourne, *An Introduction to Galaxies and Cosmology*, Cambridge University Press, 2004.

[85] J.C. Brown, ASP Conference Series **438**: 216-228, 2011.

[86] R. Jansson and G.R. Farrar, ApJ **761**:L11, 2012.

[87] R. Jansson and G.R. Farrar, ApJ **757**:14, 2012.

[88] A.W. Strong, I.V. Moskalenko and V.S. Ptuskin, Annu. Rev. Nucl. Part. Sci. **57**: 285-327, 2007.

[89] V. Moskalenko et al., Proceedings of the 32nd ICRC **6**:279-282, 2011.

[90] http://dragon.hepforge.org

[91] M. Kachelreiss and S. Ostapchenko, Phys. Rev. D **90**: 083002, 2014.

[92] T.K. Gaisser, *Cosmic Rays and Particle Physics*, Cambridge University Press, Cambridge (1991). ISBN: 978-0521339315.

[93] T.K. Gaisser, arXiv:1303.1431

[94] D. Gaggero et al., ApJ Letters **815**: L25, 2015.

[95] T. Prodanović, B.D. Fields and J.F. Beacom, Astrop. Phys. **27**: 10, 1997.

[96] S. Snowden et al. ApJ **485**: 125, 1997.

[97] J.M. Casandjian, arXiv:1502.07210, 2015.

[98] O. Adriani et al., Science **332**: 69, 2011.

[99] M. Aguilar et al., Phys. Rev. Lett. **114**: 171103, 2015.

[100] A. Neronov, D. Semikoz and C. Tchernin, Phys. Rev. D **89**: 103002, 2014.

[101] A.M. Taylor et al., Nucl. Inst. Meth. Phys. Res. A **602**:113-116, 2009.

[102] M. Ackermann et al., ApJ **203**: 4, 2012.

[103] http://home.thep.lu.se/∼torbjorn/Pythia.html

[104] P. Amram et al., Astrop. Phys. **13**: 127-136, 2000.

[105] M. Ageron et al., Astrop. Phys. **31**: 277-283, 2009.

[106] P. Amram et al., Nucl. Inst. and Meth. in Phys. Res. A **484**: 369, 2002.

[107] J.A. Aguilar et al., Nucl. Inst. and Meth. in Phys. Res. A **555**: 132, 2005.

[108] J.A. Aguilar et al., Nucl. Inst. and Meth. in Phys. Res. A **622**: 59, 2010.

[109] J.A. Aguilar et al., Nucl. Inst. and Meth. in Phys. Res. A **570**: 106, 2007.

[110] J.A. Aguilar et al., Astrop. Phys. **23**: 131-155, 2005.

[111] P. Amram et al., Astrop. Phys. **19**:253-267, 2003.

[112] M. Circella et al., Nucl. Instr. and Meth. A **602**:1-6, 2009.

[113] F. Feinstein et al., Nucl. Instr. and Meth. A **504**: 258, 2003.

[114] A. Heijboer et al., Proceedings of the 31st ICRC, Lodz, Poland, 2009; arXiv:0908.0816.

[115] S. Klimushin, E. Bugaev & I. Sokalski, Proceedings of the 27th ICRC, Hamburg, Germany, 2001; arXiv:hep-ph/0106010

[116] K.A. Olive et al. (Particle Data Group), Chin. Phys. C **38**: 090001, 2014.

[117] J. Schnabel et al., Nucl. Inst. and Meth. in Phys. Res. A **725**: 106-109, 2013.

[118] D. Palioselitis, PhD thesis, University of Amsterdam, 2013.

[119] F. Schüssler et al., Proceedings of the 33rd ICRC, Rio de Janeiro, Brazil, 2013.

[120] A. Margiotta et al., Nucl. Inst. and Meth. in Phys. Res. A **725**: 98-101, 2013.

[121] D. Heck et al., report FZKA-6019, 1998.

[122] G. Carminati et al., Computer Physics Communications **179, 12**: 915-923, 2008.

[123] Y. Becherini et al., Astrop. Phys. **25**: 1, 2006.

[124] *GEANT* program manual, CERN program library long writeup, W5013, 1993.

[125] P. Antonioli et al., Astrop. Phys., **7**: 357, 1997.

[126] http://root.cern.ch

[127] H. van Haren et al., Deep-Sea Research I **58**: 875-884, 2011.

[128] L.A. Fusco and A. Margiotta et al., Proceedings of the VLVnT 2015, Rome, Italy, 2015.

[129] S. Adrian Martínez et al., Eur. Phys. J. C **73**: 2606, 2013.

[130] L.V. Volkova and G.T. Zatsepin, Soviet Journal of Nuclear Physics 37: 212, 1980.

[131] G.D. Barr et al, Phys. Rev. D **70**: 023006, 2004. The extension of high energy in 2009 is in http://www-pnp.physics.ox.ac.uk/∼barr/fluxfiles/.

[132] M. Honda et al., Phys. Rev. D **75**: 043006, 2007.

[133] G.D. Barr et al, Phys. Rev. D **74**:094009, 2006.

[134] C.G.S. Costa, Astrop. Phys. **16**: 193, 2001.

[135] A. Martin et al., Acta Phys. Pol. B **34**: 3273, 2003.

[136] R. Enberg et al., Phys. Rev. D **78**: 043005, 2008.

[137] A.N. Tikhonov, Sov. Math **4**: 1035, 1963.

[138] A. Hocker & V. Kartvelishvili, Nucl. Inst. and Meth. in Phys. Res. A **372**: 469, 1996.

[139] G. D'Agostini, Nucl. Inst. and Meth. in Phys. Res. A **362**: 487, 1995.

[140] http://hepunx.rl.ac.uk/∼adye/software/unfold/RooUnfold.html .

[141] http://root.cern.ch .

[142] R. Abbasi et al., Astrop. Phys. **34**: 48, 2010.

[143] R. Abbasi et al., Phys. Rev. D **83**: 012001, 2011.

[144] R. Abbasi et al., Phys. Rev. D **79**: 102005, 2009.

[145] M. Ambrosio et al., Eur. Phys. J. C **36**: 323, 2004.

[146] R. Abbasi et al., Phys. Rev. D **84**: 082001, 2011.

[147] S. Adrian Martínez et al., Eur. Phys. J. C **74**: 2701, 2014.

[148] M. Ackermann et al., ApJ **793**: 64 (2014).

[149] G.C. Hill ant K. Rawlins, Astrop. Phys. **19**: 393, 2003.

[150] G.J. Feldman and R.D. Cousins, Phys. Rev. D **57**: 3873-3889, 1998.

[151] S. Adrian Martínez et al., Astrop. Phys. **42**: 7-14, 2013.

[152] A. Trovato et al., Proceedings of the 34th ICRC, ID 1279, The Hague, The Netherlands, 2015)

[153] A. Trovato et al., Proceedings of the 34th ICRC, ID 1282, The Hague, The Netherlands, 2015.

[154] A. Hoecker, P. Speckmayer, J. Stelzer, J. Therhaag, E. von Toerne, and H. Voss, TMVA - Toolkit for Multivariate Data Analysis, PoS ACAT 040, 2007.

Acknowledgements